이학박사학위논문

Large-Area Synthesis of High-Quality Graphene Films for Gas-Barrier Applications

가스 배리어를 위한 대면적 고품질 그래핀 합성 연구

2015년 8월

서울대학교 대학원

화학부 물리화학 전공

Kyoungjun Choi

Large-Area Synthesis of High-Quality Graphene Films for Gas-Barrier Applications

가스 배리어를 위한 대면적 고품질 그래핀 합성 연구

지도교수: 홍 병 희

이 논문을 이학박사 학위논문으로 제출함

2015년 6월

서울대학교 대학원

화학부 물리화학 전공

최 경 준

최경준의 이학박사 논문을 인준함

2015년 6월

Chair _____ **(Seal)**

Vice Chair _____ **(Seal)**

Examiner _____ **(Seal)**

Examiner _____ **(Seal)**

Examiner _____ **(Seal)**

Ph.D. Thesis

Large-Area Synthesis of High-Quality Graphene Films for Gas-Barrier Applications

Supervisor: Professor Byung Hee Hong

Major: Physical Chemistry

By Kyoungjun Choi

Department of Chemistry

Graduate School of Seoul National University

2015

Abstract

Chapter 1 describes general introduction of the thesis. The properties and synthesis methods of graphene are introduced briefly.

Chapter 2, improving the properties of graphene has been intensively studied to facilitate the practical applications for electronics. In addition, developing novel approaches to lower the growth temperature and simplify the fabrication steps of graphene devices are demanded. Here, we report a simple method to prepare uniformly and selectively grown monolayer graphene by chemical vapor deposition (CVD) using acetylene (C2H2) at temperature as low as 800 °C, which was evidenced by Raman Spectroscopy, SEM, and TEM. The organic field-effect transistors (OFETs) based on the selectively grown graphene electrodes exhibit enhanced performance compared to photolithography-patterned graphene electrodes. We expect that our method would enable the cost-effective high-performance synthesis and applications of graphene by providing lower synthesis temperature that does not require quartz chambers and simplifying the complicated post-growth pattering processes of graphene electrodes.

Chapter 3, two dimensional semiconductor such as MoS_2 are an emerging material with wide-ranging potential applications in electronics, optoelectronics, and energy harvesting. Large-area growth and control over lattice orientation remain a challenge. Here, we have demonstrated metal organic chemical vapor deposition growth of monolayer MoS2 on sapphire by the use of liquid phase Mo-precursor. The AFM and SEM images revealed that the MoS2 flake is well-defined triangular shape and MoS2 flake has observed step heights of individual layers of 0.7-0.8 nm. Furthermore, Raman and PL spectrum indicate that monolayer MoS2 is less doped and smaller structural disorder. We believe that our versatile MOCVD leads to synthesis high quality monolayer MoS2, allowing its use in future electronic and optoelectronic

devices.

Chapter 4, preventing reactive gas species such as oxygen or water is important to ensure the stability and durability of organic electronics. Although inorganic materials have been predominantly employed as the protective layers, their poor mechanical property has hindered the practical application to flexible electronics. The densely-packed hexagonal lattice of carbon atoms in graphene does not allow the transmission of small gas molecules. In addition, its outstanding mechanical flexibility and optical transmittance are expected to be useful to overcome the current mechanical limit of the inorganic materials. In this paper, we reported the measurement of the water vapor transmission rate (WVTR) through the 6-layer 10x10 cm2 large-area graphene films synthesized by chemical vapor deposition (CVD). The WVTR was measured to be as low as 10-4 g/m2·day initially, and stabilized at ~0.48 g/m2·day, which corresponds to 7 times reduction in WVTR compared to bare polymer substrates. We also showed that the graphene-passivated organic field-effect transistors (OFETs) exhibited excellent environmental stability as well as a prolonged life time even after 500 bending cycles with strain of 2.3 %. We expect that our results would be a good reference showing the graphene's potential as gas barriers for organic electronics.

Keyword **:** Graphene, Selective Growth, Barrier Films, MoS_2, Organic Field Effect Transistors, van der Waals Epitaxy

Student Number : 2013-30094

Contents

Chapter 1. General Introduction

Chapter 2. Graphene Growth at Low-Temperature

- Selective Growth of Graphene by Chemical Vapor Deposition on Patterned Cu-Ni Alloy Catalyst

Chapter 3. The Synthesis of MoS_2 on Sapphire

- van der Waals Epitaxial Growth of MoS_2 by Metal Organic Chemical Vapor Deposition

Chapter 4. Graphene Gas Barrier Films

- Reduced Water Vapor Transmission Rate of Graphene Gas Barrier Films for Flexible Organic Field-Effect Transistors

Appendix

List of Figures

Chapter 1

Figure 5. a,b, Band structures calculated from first-principles density functional theory (DFT) for bulk and monolayer MoS_2 (a) and WS_2 (b). The horizontal dashed lines indicate the Fermi level. The arrows indicate the fundamental bandgap (direct or indirect). The top of the valence band (blue) and bottom of the conduction band (green) are highlighted.

Chapter 2

Figure 1. Analysis of graphitic carbon grown on Cu and graphene grown on Cu-Ni alloy at 1000°C. (a) SEM image of graphitic carbon. (b) Raman spectrum and (c) XPS spectrum of graphitic carbon transferred on SiO2/Si. (d) SEM image of graphene. (e) Raman spectrum and (f) XPS spectrum of graphene transferred on SiO2/Si. Scale bars, 500nm.

Figure 2. The optimization of high quality and selectively grown monolayer graphene (a) The difference in the interaction between hydrocarbon gas and metal catalysts as well as the growth mechanism corresponding to the nucleation and growth of monolayer graphene on Cu and Cu-Ni alloy at low pressure and temperature. In part of a binary metal alloy, a Ni catalyze the dissociation and dehydrogenation of acetylene. Inset scheme, the process indicates the growth mechanism in accordance with Ni-CVD process, including dissociated carbon atom diffuse into bulk from metal surface and then segregated carbon atoms can form the nucleation of monolayer graphene. Synthesis of selectively monolayer graphene (SMG) (b) Photograph of Ni pre-pattern on Cu foil. (Graphene Research Laboratory) (c) Optical microscope image of the selective growth of monolayer graphene, transferred on SiO_2/Si, synthesized from the catalysts shown in (b). Scale bars, 1mm. (d) Raman intensity mapping of 2D peak in the region of red box in (c).

Figure 3. Raman spectrums of graphene grown on Cu-Ni on temperature variation from 700 ºC to 1000 ºC.

Figure 4. The optimization of high quality and selectively grown monolayer graphene (a) Raman spectra of graphene depending on Ni thickness. (b) The plot of 2D/G peak intensity ratio as a function of Ni thickness. (c) Raman spectra of graphene depending on C2H2 flow. (d) The plot of 2D/G peak intensity ratio as a function of C2H2 flow.

Figure 5. The optical characteristics of monolayer graphene grown on Cu-Ni alloy at 800 °C. (a) The comparison of Raman spectrum of monolayer graphene grown on Cu-Ni and on Cu at 1000 °C, transferred on SiO_2/Si. Raman mapping images of (b) 2D/G peak intensity and (c) D/G peak intensity of monolayer graphene. Scale bars, 5μm. (d) Electrical characteristic of the FET devices of monolayer graphene (e) SAED pattern and profile plots of diffraction spot intensities along red arrow. (inset) TEM image of monolayer graphene. Scale bar, 100 nm. (f) high-angle annular dark field (HAADF) image of monolayer graphene.

Figure 6. (a) Optical image of graphene. (b) The sheet resistance of graphene depending on doping

Figure 7. EM analysis of graphene as a function of temperature. (a) SEAD pattern of, and (d) SEM image of graphene grown at 1000 °C. (b) SEAD pattern of, and (e) SEM image of graphene grown at 900 °C. (c) SEAD pattern of, and (f) SEM image of graphene grown at 800 °C. Scale bar, 500 nm.

Figure 8. High-magnification SEM images of the flake of graphene on Cu catalyst for the calculation of graphene coverage depending on temperatures. Scale bar, 500 nm.

Figure 9. Analysis of kinetics of graphene growth. (a) Representative scanning electron

micrographs showing flake evolution with the elapsed time, at 800 °C (scale bar: 500 nm). (b) As-grown graphene coverage on Cu as a function of temperature. (c) Evolution of the mean flake area with growth time for the four temperature. (700, 750, 800, and 850 °C) (d) Arrhenius plot of graphene growth rate as a function of 1000/T. Each point was obtained in (c).

Figure 10. High-magnification SEM images of the flake of graphene on Cu catalyst for the calculation of flake area and growth rate depending on growth temperatures and times. Scale bar, 500nm.

Figure 11. Electrical properties of pentacene FETs with various electrodes, such as SMG, photolithography monolayer graphene (PMG), and Au metal, on SiO_2/Si. (a) Transfer characteristics in the saturation regime (V_D = 80 V), and (c) output characteristics of OFETs prepared with the three types of electrodes. (b) Compared with calculation of the contact resistance values. All electrical measurements were performed in a N_2-rich glove box.

Figure 12. Raman spectra of SMG electrode. (inset) Optical image of SMG electrode.

Figure 13. Channel width-normalized R_{total} of the pentacene FETs with (a) SMG electrodes, (b) PMG electrode, and (c) Au electrodes.

Chapter 3

Figure 1. (a) Photographs of monolayer MoS_2 grown on sapphire (right). The left substrate shows the bare sapphire for comparison. (b) SEM image of monolayer MoS_2 flake on sapphire. (c) AFM image of monolayer MoS_2 flake. Inset: Line scan showing the thickness profile along the red line in the AFM image.

Chapter 4

Figure 5. (**a, b)** Optical transmittance and UV–Vis spectra of graphene films on PET films with increasing number of graphene layers, respectively.

Figure 6. XPS spectra of (a) bare Cu foil and (b) Cu foil with graphene film after air oxidation ($Cu2p_{3/2}$; 932.6 eV, $Cu2p_{1/2}$: 952.4 eV, Cu_2O ; 932.4 and 952.4 eV, CuO ; 933.6 and 953.4 eV, $Cu(OH)_2$; 934.3 and 954.5 eV) after two months under ambient pressure and room temperature. Scale bars, 2 μm.

Figure 7. (**a-c**) AFM topographs and XPS spectra of bare pentacene, oxidized pentacene with graphene, and oxidized pentacene without graphene, respectively. Scale bars, 400 nm. The oxidation was carried out by using UV/Ozone treatment for 1 hour. The AFM profiles of pentacene on SiO_2/Si along the red line clearly shows the degradation of pentacene film by oxidation. The XPS analyses of the C1s core level bands show that the oxygen related peaks appear as oxidation proceeds.

Figure 8. (a) ~ (f) AFM topographs of pentacene as a function of UV/Ozone treatment time. (g) Cross sectional AFM relative height of (a) bare pentacene and (f) oxidized pentacene for 2 h 30 m.

Figure 9. Schematic of the difference between the conventional and reverse method for transferring graphene films.

Figure 10. (a) I_D versus V_G transfer characteristics and $I_D^{1/2}$ versus V_G characteristics of before (black curve) and after (red curve) passivated OFET with graphene. (b) Before applying voltage to a passivated OFET and (c) after applying voltage to a passivated OFET

Figure 11. (a) Time-dependent $I_D^{1/2}$ *vs*. V_G characteristics of the bare OFETs (left) and an OFET passivated with PMMA/graphene (right). (**b**) Time-dependent relative field-effect mobilities of bare pentacene, pentacene with PMMA, and pentacene with PMMA/graphene

films. Bending cycle tests: (**c**) I_D *vs*. V_G transfer characteristics and the $I_D^{1/2}$ *versus* V_G characteristics of a passivated OFET prepared with PMMA/ 6-layer graphene. (**d**) Field-effect mobility and on-off ratio of a passivated OFET prepared with PMMA/ 6-layer graphene. All the electrical measurements were performed using the reversed transfer method at 25°C under 60% relative humidity.

Figure 12. Relative WVTR values with increasing bending cycles, where WVTRo and $WVTR_b$ denote the WVTR values before and after bending, respectively.

Chapter 1

General Introduction[1]

[1] S. J. Kim, K. Choi et al. Materials for Flexible, Stretchable Electronics: Graphene and 2D Materials, *Ann. Rev. Mater. Res.* **45** (2015)

The Atomic Structure of Layered 2D Materials

The Atomic Structure of Graphene

To understand the discovery of graphene, it is helpful to first gain an understanding of the peculiarities of elemental carbon. The general interest in carbon arises from the variety of structural forms in which this element is available. This variety results from a special electron configuration of carbon that provides the ability to form different types of valence bonds to various elements. Carbon has the atomic number 6 and therefore, electrons occupy the $1s^2$. $2s^2$, $2p_x^1$ and $2p_y^1$ atomic orbitals in Figure 1a. It is a tetravalent element, i.e. only the four exterior electrons participate in the formation of covalent chemical bonds.

When forming bonds with other atoms, carbon promotes one of the 2s electrons into the empty $2p_z$ orbital, resulting in the formation of hybrid orbitals. In diamond the 2s-energy level hybridizes with the three 2p levels to form four energetically equivalent sp^3-orbitals that are occupied with one electron each (Figure 1b).

In graphite only two of the three 2p-orbitals partake in the hybridization, forming three sp^2-orbitals (Figure 1c). The sp^2-orbitals are oriented perpendicular to the remaining 2p-orbital, therefore lying symmetrically in the X-Y plane at 120º angles. Thus, sp^2-carbon atoms form covalent in-plane bonds affecting the planar hexagonal “honeycomb” structure of graphite. While the in-plane σ-bonds within the graphene layers (615 kJ/mol) are even stronger than the C-C bonds in sp^3-hybridized diamond (345 kJ/mol), the interplane π-bonds, formed by the remaining 2p-orbitals, have a significantly lower binding energy, leading to an easy shearing of graphite along the layer plane. This atomic structure of graphene opens a gate for the real investigation of only single-layer graphene by mechanical exfoliation.[1]

The Atomic Structure of TMDs

Many transition metal dichalcogenides (TMDs) crystallize in a graphite-like layered structure that leads to strong anisotropy in their electrical, chemical, mechanical and thermal properties.[2] In layered structures, each layer typically has a thickness of 6~7 Å, which consists of a hexagonally packed layer of metal atoms sandwiched between two layers of chalcogen atoms. The intra-layer M–X bonds are predominantly covalent in nature, whereas the sandwich layers are coupled by weak van der Waals forces thus allowing the crystal to readily cleave along the layer surface. Studies have shown that the single layers are stabilized by development of a ripple structure as in the case of graphene.[3]

The metal atoms provide four electrons to fill the bonding states of TMDs such that the oxidation states of the metal (M) and chalcogen (X) atoms are +4 and –2, respectively. The lone-pair electrons of the chalcogen atoms terminate the surfaces of the layers, and the absence of dangling bonds renders those layers stable against reactions with environmental species. The M–M bond length varies between 3.15 Å and 4.03 Å, depending on the size of the metal and chalcogen ions. These values are 15–25% greater than the bond lengths found in elemental transition metal solids, indicating limited energetic and spatial overlap of the d orbitals in TMD compounds. The metal coordination of layered TMDs can be either trigonal prismatic or octahedral (typically distorted and sometimes referred to as trigonal-antiprismatic) as shown in Fig. 1b and c, respectively. Depending on the combination of the metal and chalcogen elements, one of the two coordination modes is thermodynamically preferred.

In contrast to graphite, bulk TMDs exhibit a wide variety of polymorphs and stacking polytypes (a specific case of polymorphism) because an individual MX2 monolayer, which itself contains three layers of atoms (X–M–X), can be in either one of the two phases (Figure

2). Most commonly encountered polymorphs are 1T, 2H and 3R where the letters stand for trigonal, hexagonal and rhombohedral, respectively, and the digit indicates the number of X–M–X units in the unit cell (that is, the number of layers in the stacking sequence). There are three different polytypes (that is, three different stacking sequences) for 2H polymorphs. A single TMD can be found in multiple polymorphs or polytypes, depending on the history of its formation. For example, natural MoS_2 is commonly found in the '2H phase' where the stacking sequence is AbA BaB (The capital and lower case letters denote chalcogen and metal atoms, respectively). Synthetic MoS2, however, often contains the 3R phase where the stacking sequence is AbA CaC BcB.[4] In both cases, the metal coordination is trigonal prismatic. Group 4 TMDs such as TiS2 assume the 1T phase where the stacking sequence is AbC AbC and the coordination of the metal is octahedral.

The Synthesis of Layered 2D Materials

Mechanical Exfoliation

Mechanical exfoliation refers to the process where mechanical force is used to separate the sheets of layered 2D materials such as graphene and TMDs from bulk layered 2D materials. This generally involves using either an adhesive tape to attach to the surface of bulk and using force to peel off the tape plus the sheets of layered 2D materials attached or by rubbing the surface of bulk against another material to slide off layered 2D material sheets from the bulk. The principle of writing with a pencil involves this process where the lead is actually graphite and as it is forced against paper thin graphite sheets are adhered to the paper leaving a black mark. At some stage in most of our lives we have all made graphene when putting pencil to paper.

The ease of production and low cost make exfoliation of layered 2D material the most popular route to prepare graphene and TMDs, Many routes have been demonstrated for exfoliation, including micromechanical exfoliation,[4,5] and intercalation steps.[6,7] The adhesive tape micromechanical exfoliation is easy and a quick one and provides high-quality large graphene sheets which are useful for the various experimental studies. However, the main drawback of this technique is that it does not provide sufficient output yield for many applications. Moreover, the purity of the produced material often contains may induce strain on the sheet of layered 2D material during deposition on a substrate and introduce various types of defects. Nevertheless, exfoliation is still attractive as a facile method to obtain a single crystalline layered 2D material due to its simplicity and the possibility to obtain layered 2D material with little to no grain boundaries.

Chemical Exfoliation

The layers of 2D material that are stacked together can be separated from the bulk using solution based chemistry. To achieve layer separation, the strong van der Walls forces that stick layered 2D material sheets together must be overcome. This generally requires some form of input energy and calculations suggest that 2 eV/nm^2 is needed to separate layers.[8] Even though the sheets of layered 2D materials has been studied for a long time, chemical exfoliation is a great method for obtaining large amounts of micron sized flakes of layered 2D material in a wide range of solvent hosts.

Chemically exfoliation methods for preparation of graphene

The idea of exfoliating a layer of graphene from graphite to obtain graphene quickly expanded to other variation such as chemical exfoliation. It utilizes strong acids and oxidants to produce graphene oxide (GO) from graphite. Graphene oxide is the name given to graphene that has been oxidized and as such the pristine nature of the graphene lattice disrupted. The oxidization of graphite has been the subject of investigation since at least the mid-19^{th} century.[9,10] One of the first reports was by Brodie (1860) where graphite was treated with potassium chlorate ($KClO_3$) and fuming nitric acid (HNO_3). Staudenmaier (1898) later improved this approach for oxidizing graphite by slowly assed the potassium chlorate over the course of a week to a solution containing concentrated sulphuric acid, concentrated nitric acid (63%) and graphite. However, needing a 10:1 mass ratio of potassium chlorate to graphite, researchers found this method dangerous due to possibility of explosion and time-consuming. More than 56 years later Hummers and Offeman (1958) reported an alternative ‘safer’ method known as the Hummers method, which involved a water-free mixture of concentrated sulphuric acid, sodium nitrate, and potassium permanganate. Temperatures of only 45 C were required and the entire reaction took only 2 hours to complete.

All three methods involve oxidation of graphite to various levels. Graphite salts made by intercalating graphite with strong acids such as H_2SO_4, HNO_3 or $HClO_4$ have also been used as precursors for the subsequent oxidation to GO. [249] Graphene oxide disperse well in water due to the negative surface charges on the sheets that arise from the phenols and carboxylic acid groups that decorate graphene oxide and keep it from reaggregating.[11] The hydrophilic nature of graphene oxide means that water molecules easily intercalate graphite oxide, leading to variable inter-sheet separations ranging from 0.6 nm to 1.2 nm.[12]

For many years there was uncertainty regarding the specific atomic structure of graphite oxide and subsequently graphene oxide. In many of the graphite oxide structure studies, solid-state NMR was used to provide insights, however, the low nature abundance of ^{13}C leads to relatively poor signal to noise ratio. Cai et al. overcome this problem by using synthetic ^{13}C labelled graphite to prepare graphene oxide.[13]

Chemically exfoliation methods for preparation of TMDs

Liquid exfoliation methods are likely to be better suited for fundamental and proof-of-concept demonstrations in applications where large quantities of materials are required, such as electrochemical energy storage, catalysis, sensing or fillers for composites. Liquid exfoliation by direct sonication in commonly used solvents such as dimethylformamide and N-methyl-2-pyrrolidone has been used to disperse graphene. Recently, this method was employed to fabricate single-layer and multilayer nanosheets of a number of layered inorganic compounds, such as MoS_2, WS_2, $MoSe_2$, $NbSe_2$, $TaSe_2$, $NiTe_2$, $MoTe_2$, h-BN and Bi_2Te_3.[14]

One of the most effective methods for mass production of fully exfoliated TMD nanosheets is the ultrasound-promoted hydration of lithium-intercalated compounds. Joensen and co-workers[15] demonstrated the preparation of single-layer MoS2 with n-butyl lithium dissolved in hexane as the intercalation agent. An important step in the lithium intercalation process is the formation of Li_xXS_2 compound and this reaction can be tuned to control the yield of monolayers. The degree of lithiation also has implications on the amount of 1T phase present in MX2. The lithiated solid product can then be retrieved by filtration and washed with hexane to remove excess lithium and organic residues from n-butyl lithium. The extracted product can be readily exfoliated by sonication in water. The yield of this method is very high (nearly 100% of the products are atomically thin).[7] The key advantage of the Li intercalation method is the ability to access the metallic 1T phase that is induced through charge transfer from Li to the TMD. To accommodate this additional charge, a local rearrangement of the atomic structure from the 2H to the 1T phase occurs. The metastable 1T phase remains even in the solid form and the residual negative charge on the nanosheets is passivated by the presence of a water bilayer containing protons or residual Li ions.

Epitaxial Growth

The attraction in the use of silicon carbide for the formation of graphene stems from the fact that graphene films cab be grown epitaxially on commercial SiC substrates. Moreover, the grown graphene can be patterned using standard lithography methods without the need for transfer. This makes the technique compatible with current semiconductor technology.[16] In addition, the technique is very clean because no metal or hydrocarbon are involved since the epitaxially matching support itself provides the carbon. Epitaxial graphene grown on SiC can exhibit long phase coherence lengths and mobilities exceeding 25,000 cm^2/V s, further adding attraction to graphene grown in this manner.[17] These aspects have made it a widely used technique. The technique is based on the controlled sublimation of Si from single-crystalline SiC surfaces. The sublimation process, in which a direct transformation of material in the solid phase to the vapor phase occurs, does not preserve stoichiometry for binary compounds. This is related to the binding energy between atoms such that less tightly bound atoms in the solid sublimate first. In the specific case of SiC, Si sublimates first leaving behind a few layers of nearly free carbon species. These layers rearrange on the surface so as to minimize energy forming graphene in the process.[18] Calculations on molar densities show that approximately three bi-layers of SiC are required to free sufficient carbon atoms for the formation of a single-graphene layer.[19] To form epitaxial graphene in this manner the (0001) (silicon terminated) and $(000\bar{1})$ (carbon terminated) faces of 4H and 6H α-SiC wafers are usually used.

The technique itself dates back to the early 1960s when Badami during X-ray scattering studies found graphite on SiC after heating it to 2150 ºC in UHV.[20] He suggested that the graphite formed through preferential surface Si-out diffusion. Over a decade later, Van Bommel and co-workers found single layers of graphite on SiC after annealing at 800 ºC and enhanced

graphitization around 1500 ºC. They also identified that the observed differences in the crystallinity of the graphene layers has a dependence on the surface termination, namely, the Si-terminated (0001) face and the C-terminated $(000\bar{1})$ face. They found that the epitaxial alignment of graphene on the C-terminated $(000\bar{1})$ face is rotated 30 ºC with respect to the Si-face unit cell. Later in the 1980s and 1990s few researchers conducted more detailed studies on the graphitization process, which, in short, confirmed the results of Van Bommel. Recently, the parallel publication of the electrical response of graphene in 2004 by Novoselov et al. and Berger et al. provided new impetus to optimize the growth conditions of graphene on SiC.[16,21]

Chemical Vapor Deposition Methods

Chemical Vapor Deposition of Graphene

The fabrication of graphene over metals by chemical vapor deposition is one of the most popular synthesis routes. The reasons for this are various and include the potential to scale-up fabrication, the technique is already well established in industrial settings and it is easy to set-up in research laboratories amongst other attractive traits. CVD grown graphene over metals can also be established in over large areas and this is important for applications, for example, transparent conducting electrodes for solar cells, where a contiguous covering of graphene is required. This is fundamentally different to exfoliation routes that result in graphene flakes scattered randomly over a substrate.

The chemical vapor depositing of sp^2 carbon entails passing a carbon feedstock over the surface of a catalyst substrate (e.g. transition metal) at elevated temperatures. The catalyst then catalytically decomposes the feedstock to provide a supply of carbon. The catalytic potential of transition metals is well established and is argued to arise from partially filled d orbitals or by the formation of intermediate compounds which can absorb and activate the reacting medium. In essence, the metals provide low energy pathways for reactions by changing oxidation states easily or through the formation of intermediates. Once the feedstock has decomposed and provided a source of carbon, the carbon can be absorbed by the metal and then later precipitate out to form graphene as for example Ni and Co, or if carbon solubility is limited, then sp^2-carbon formation can occur as a surface process as for example is the case for Cu.

Intensive early studies using nickel soon revealed a fundamental limitation with this

catalyst, namely that single and few layer graphene is obtained over tens of microns and is not homogeneous across the substrate surface. In other words, control over the number of layers is limited. This is argued to occur because Ni has a large carbon solubility.[22] Above 800 °C, carbon and nickel form a solid solution. The solubility of carbon decreases below 800°C so that upon cooling, carbon diffuses out of the Ni. In short, carbon segregation is rapid within Ni grains and heterogeneous at grain boundaries. This means the number of graphene layers that form at grain boundaries exceeds that forming over Ni grains and leads to a variation in the number of graphene layers forming on the surface. To some degree this can be alleviated by using single crystalline Ni, however whilst this is attractive for producing graphene for fundamental studies, it is limited in practical terms for large area and cost.

Copper has a low carbon solubility at high temperature (0.008 weight% at 1084 °C).[23] The interest in copper as a substrate stems from its potential to catalyse various carbon allotropes such as graphite,[24] diamond,[25] and carbon nanotubes.[26] Unlike most substrate with high carbon solubility at elevated temperature, substrates with low carbon solubility allow more facile single graphene formation over large areas, for example on Cu foil. Graphene formation over ruthenium has also been demonstrated. Ru has a carbon intermediate carbon solubility at high temperature. With Ru implementing a gradual decreases in temperature enables uniform graphene nucleation and growth.[24]

A great advantage of Cu is that it can be grown over huge areas. Bae et al. demonstrated this beautifully in a roll to roll process for the production of predominantly 30-inch graphene film.[28] The films were found to have a sheet resistance of around 150 Ω/square with 97.4% optical transmittance and exhibit half-integer quantum hall effect which highlights the high quality of the material making it suitable for transparent electrode fabrication on an industrial

scale.

Chemical Vapor Deposition of single-layer TMDs

Chemical vapor deposition of graphene on copper has been a major breakthrough that has enabled the preparation of large-area graphene.[29] Very recently, synthesis of large-area ultrathin MoS2 layers using CVD has been demonstrated using several approaches.[30,31] Most of the current CVD research has focused on MoS_2; we therefore introduce the details of MoS_2 growth by CVD, then discuss strategies for extending the methodology to other single-layered TMDs materials.

A two-step thermolysis process shown in Fig. 4a was reported for deposition of three-layered MoS2 sheets by dip-coating in ammonium thiomolybdates [$(NH_4)_2MoS_4$] and converting to MoS_2 by annealing at 500 °C followed by sulfurization at 1,000 °C in sulfur vapour.[30] The chemical reaction leading to the formation of the MoS_2 layers is $(NH_4)_2MoS_4 + H_2 \rightarrow 2NH_3 + 2H_2S + MoS_2$. The second annealing at 1,000 °C is required for improving the crystallinity (or the size of MoS2 domains). A different strategy reported for deposition of single-layer MoS2 is based on the sulfurization of Mo metal thin films. Adsorption of sulfur on the Mo film to form MoS2 has been studied since the 1970s,[32] and it has been demonstrated through low-energy electron diffraction, auger electron spectroscopy and thermal desorption spectroscopy that sulfur atoms form ordered phases on the Mo crystal face58. Nuclei of MoS_2 appear in conjunction with chemisorbed sulfur species and then the film is formed by the diffusion of sulfur, which is affected by pressure and temperature.[33]

Lee and co-workers have reported an alternative method for synthesizing large-area MoS2 monolayer flakes using the gas-phase reaction of MoO3 and S powders.[31] They conclude that treatment of substrates with aromatic molecules such as reduced graphene oxide, perylene-3,4,9,10-tetracarboxylic acid tetrapotassium salt (TPAS) and perylene-3,4,9,10-tetracarboxylic

dianhydride (PTCDA) prior to deposition assists in the growth. The reaction mechanism in their study is likely to be: $MoO_3 + x/2S \rightarrow MoO_{3-x} + x/2SO_2$ and $MoO_{3-x} + (7-x)/2S \rightarrow MoS_2 + (3-x)/2SO_2$, where MoO_2 during the reaction is an intermediate phase formed when x = 1. However, full coverage of the substrate is a challenge using this method. Lin and co-workers have shown that wafer-scale deposition can be achieved using the same chemistry, where the few-layer MoS_2 was obtained after direct sulfurization of MoO_3 thin-films on sapphire substrates.[34]

The Properties of Layered 2D Materials

Properties of graphene

Graphene has a unique band structure that results in many attractive electronic properties, such as a 10–100-times-higher carrier mobility than Si. For instance, in 2008, Kim's group at Columbia showed that single-layer graphene prepared by using the mechanical exfoliation method exhibited carrier mobility in excess of 200,000 cm2/(V·s) at room.[35] By fabricating a suspended graphene channel, they were able to minimize substrate-induced scattering and to obtain essentially ballistic charge transport at millimeter length scales at room temperature.

Lee et al.[36] reported that single-layer graphene is mechanically very strong. They showed that when a graphene sheet suspended across 1.0–1.5-μm cavities in a SiO2 film was deflected using an AFM tip, the graphene sheet stayed intact and exhibited a Young's modulus of 1 TPa and a large spring constant (1–5 N/m). The excellent mechanical properties of graphene have also been investigated by measuring the electrical resistance on stretching, and as shown in Figure 3c, the resistance shows little variation with strain.[37] This combination of large strain capability and small changes in resistance is necessary for the operation durability of a flexible and stretchable device.

Presently, ITO is widely used as a transparent conductor for optoelectronic devices. However, ITO has poor mechanical properties; it tends to crack easily or shows defects when strained. For these reasons, the use of graphene has been widely investigated in recent years as a transparent conductor for optoelectronic and photonic applications because of its combination of electrical, mechanical, and optical properties. The optical properties of graphene result in high opacity for an atomic monolayer. The transmittance of graphene decreases approximately

2.3% with each layer as the number of graphene layers increases.[38] Furthermore, graphene films transferred onto flexible polyethylene terephthalate (PET) and stretchable PDMS substrates maintain their high transparency and flexible properties.[39]

The adsorption of various molecules on the graphene surface is possible because of graphene's hydrophobic surface, which is similar to that of carbon nanotubes (CNTs). Also, the conductivity and doping types can be modified by chemical treatment. There are now numerous reports of doping methods such as modification of the substrate surface with self-assembled monolayers; sp3 functionalization of carbon with H, F, or Cl; atomic substitution with N; and surface treatment of graphene by using certain molecules or acidic solutions.[40-43]

Properties of TMDs

Graphene behaves as a zero-band-gap semiconductor, and this fact limits its applications when electronic devices are fabricated. Fortunately, a wide spectrum of 2D inorganic materials can behave as insulators [e.g., hexagonal boron nitride (hBN)], semiconductors (e.g., MoS_2, WS_2, WSe_2), and even superconductors (e.g., $NbSe_2$, NbS_2) owing to their versatile crystal structures and stacking orientations. In particular, every individual layer of transition metal dichalcogenides (TMDs) with the general formula of MX_2 is formed by a transition metal atom (M = Mo, W, Ta, etc.) sandwiched between two chalcogen layers (X = Se, S, Te).

In general, bulk semiconducting TMDs (STMDs) exhibiting a 2H phase behave as indirect band-gap semiconductors. These indirect band gaps range from 1.0–1.29 eV for MoS2 to 1.3–1.4 eV for WS_2 to 1.1 eV for $MoSe_2$ to 1.2 eV for WSe_2.[44] However, when the layered system is reduced to a single monolayer, it behaves as a direct-band-gap semiconductor.[45] Figure 2 shows the band structures calculated by using density functional theory (DFT) for mono- and few-layer WSe_2. As WSe_2 is thinned, the direct band gap at the K point of the Brillouin zone remains unaffected when the layer thickness is scaled down. This is because the direct band gap is determined through the localized d orbitals at the W atom sites, which have minimal interlayer coupling because W atoms are located in the middle of the Se-W-Se unit cell. The indirect band gap near the Γ point, however, is a linear combination of d orbitals on the W atoms and antibonding p_Z orbitals on the Se atoms; the Γ point is strongly influenced by interlayer coupling and, therefore, increases monotonically as the layer thickness is reduced. The indirect-to-direct-band-gap transition occurs when the indirect band gap becomes larger than the direct band gap in monolayers.

Thermal properties of the STMDs, which have not been studied as intensively as electronic

properties, are also relevant for many applications. Ultralow cross-plane thermal conductivity of the order of 0.05 W/mK has been found in turbostratic thin films of WSe_2.[46] In this context, cross-plane thermal conductivities of turbostratic thin films for WS_2, MoS_2, and WSe_2 exhibit 10-times-smaller values than do their respective bulk systems mainly due to phonon scattering at the domain boundaries; here the turbostratic layers exhibit domain sizes of the order of 5–10 nm.[47] The thermal conductivity in MoS2 thin films (50–150 nm) has been measured to be 1.5 W/mK along the basal planes and 0.25 W/mK across the basal planes.[48]

References

1. Haering, R. R., Band structure of phombohedral graphite. *Can. J. Phys.* **1958,** *36* (3), 352-362.
2. Wilson, J. A.; Di Salvo, F. J.; Mahajan, S., Charge-density waves and superlattices in the metallic layered transition metal dichalcogenides. *Adv. Phys.* **1975,** *24* (2), 117-201.
3. Bertolazzi, S.; Brivio, J.; Kis, A., Stretching and Breaking of Ultrathin MoS_2. *ACS Nano* **2011,** *5* (12), 9703-9709.
4. Novoselov, K. S.; Geim, A. K.; Morozov, S. V.; Jiang, D.; Zhang, Y.; Dubonos, S. V.; Grigorieva, I. V.; Firsov, A. A., Electric Field Effect in Atomically Thin Carbon Films. *Science* **2004,** *306* (5696), 666-669.
5. RadisavljevicB; RadenovicA; BrivioJ; GiacomettiV; KisA, Single-layer MoS_2 transistors. *Nat. Nanotechnol.* **2011,** *6* (3), 147-150.
6. Zhu, J., Graphene production: New solutions to a new problem. *Nat. Nanotechnol.* **2008,** *3* (9), 528-529.
7. Eda, G.; Yamaguchi, H.; Voiry, D.; Fujita, T.; Chen, M.; Chhowalla, M., Photoluminescence from Chemically Exfoliated MoS_2. *Nano Lett.* **2011,** *11* (12), 5111-5116.
8. Niyogi, S.; Bekyarova, E.; Itkis, M. E.; McWilliams, J. L.; Hamon, M. A.; Haddon, R. C., Solution Properties of Graphite and Graphene. *J. Am. Chem. Soc.* **2006,** *128* (24), 7720-7721.
9. Brodie, B., Sur le poids atomique du graphite. *Ann. Chim. Phys* **1860,** *59* (466), e472.
10. Hummers Jr, W. S.; Offeman, R. E., Preparation of graphitic oxide. *J. Am. Chem. Soc.* **1958,** *80* (6), 1339-1339.

11. He, H.; Klinowski, J.; Forster, M.; Lerf, A., A new structural model for graphite oxide. *Chem. Phys. Lett.* **1998,** *287* (1), 53-56.
12. Buchsteiner, A.; Lerf, A.; Pieper, J., Water dynamics in graphite oxide investigated with neutron scattering. *J. Phys. Chem. B* **2006,** *110* (45), 22328-22338.
13. Cai, W.; Piner, R. D.; Stadermann, F. J.; Park, S.; Shaibat, M. A.; Ishii, Y.; Yang, D.; Velamakanni, A.; An, S. J.; Stoller, M., Synthesis and solid-state NMR structural characterization of 13C-labeled graphite oxide. *Science* **2008,** *321* (5897), 1815-1817.
14. Coleman, J. N.; Lotya, M.; O'Neill, A.; Bergin, S. D.; King, P. J.; Khan, U.; Young, K.; Gaucher, A.; De, S.; Smith, R. J.; et al. Two-Dimensional Nanosheets Produced by Liquid Exfoliation of Layered Materials. *Science* **2011,** *331* (6017), 568-571.
15. Joensen, P.; Frindt, R. F.; Morrison, S. R., Single-layer MoS2. *Mater. Res. Bull.* **1986,** *21* (4), 457-461.
16. Berger, C.; Song, Z.; Li, T.; Li, X.; Ogbazghi, A. Y.; Feng, R.; Dai, Z.; Marchenkov, A. N.; Conrad, E. H.; First, P. N., Ultrathin epitaxial graphite: 2D electron gas properties and a route toward graphene-based nanoelectronics. *J. Phys. Chem. B* **2004,** *108* (52), 19912-19916.
17. Berger, C.; Song, Z.; Li, X.; Wu, X.; Brown, N.; Naud, C.; Mayou, D.; Li, T.; Hass, J.; Marchenkov, A. N., Electronic confinement and coherence in patterned epitaxial graphene. *Science* **2006,** *312* (5777), 1191-1196.
18. Camara, N.; Tiberj, A.; Jouault, B.; Caboni, A.; Jabakhanji, B.; Mestres, N.; Godignon, P.; Camassel, J., Current status of self-organized epitaxial graphene ribbons on the C face of 6H–SiC substrates. *J. Phys. D: Appl. Phys.* **2010,** *43* (37), 374011.
19. Hass, J.; De Heer, W.; Conrad, E., The growth and morphology of epitaxial multilayer graphene. *J. Phys.: Condens. Matter* **2008,** *20* (32), 323202.

20. Badami, D. V., Graphitization of α-Silicon Carbide. *Nature* **1962,** *193* (4815), 569-570.
21. Al-Temimy, A.; Riedl, C.; Starke, U., Low temperature growth of epitaxial graphene on SiC induced by carbon evaporation. *Appl. Phys. Lett.* **2009,** *95* (23), 231907.
22. Mattevi, C.; Kim, H.; Chhowalla, M., A review of chemical vapour deposition of graphene on copper. *J. Mater. Chem.* **2011,** *21* (10), 3324-3334.
23. Oshima, C.; Nagashima, A., Ultra-thin epitaxial films of graphite and hexagonal boron nitride on solid surfaces. *J. Phys.: Condens. Matter* **1997,** *9* (1), 1.
24. Ong, T.; Xiong, F.; Chang, R.; White, C., Nucleation and growth of diamond on carbon-implanted single crystal copper surfaces. *J. Mater. Res.* **1992,** *7* (09), 2429-2439.
25. Constant, L.; Speisser, C.; Le Normand, F., HFCVD diamond growth on Cu (111). Evidence for carbon phase transformations by in situ AES and XPS. *Surf. Sci.* **1997,** *387* (1), 28-43.
26. Rümmeli, M.; Grüneis, A.; Löffler, M.; Jost, O.; Schönfelder, R.; Kramberger, C.; Grimm, D.; Gemming, T.; Barreiro, A.; Borowiak-Palen, E., Novel catalysts for low temperature synthesis of single wall carbon nanotubes. *Phys. status solidi (b)* **2006,** *243* (13), 3101-3105.
27. Sutter, E.; Albrecht, P.; Sutter, P., Graphene growth on polycrystalline Ru thin films. *Appl. Phys. Lett.* **2009,** *95* (13), 133109.
28. Bae, S.; Kim, H.; Lee, Y.; Xu, X.; Park, J.-S.; Zheng, Y.; Balakrishnan, J.; Lei, T.; Ri Kim, H.; Song, Y. I.; Kim, Y.-J.; Kim, K. S.; Ozyilmaz, B.; Ahn, J.-H.; Hong, B. H.; Iijima, S., Roll-to-roll production of 30-inch graphene films for transparent electrodes. *Nat. Nanotechnol.* **2010,** *5* (8), 574-578.
29. Li, X.; Cai, W.; An, J.; Kim, S.; Nah, J.; Yang, D.; Piner, R.; Velamakanni, A.; Jung, I.; Tutuc, E.; Banerjee, S. K.; Colombo, L.; Ruoff, R. S., Large-Area Synthesis of High-

Quality and Uniform Graphene Films on Copper Foils. *Science* **2009,** *324* (5932), 1312-1314.

30. Liu, K.-K.; Zhang, W.; Lee, Y.-H.; Lin, Y.-C.; Chang, M.-T.; Su, C.-Y.; Chang, C.-S.; Li, H.; Shi, Y.; Zhang, H.; Lai, C.-S.; Li, L.-J., Growth of Large-Area and Highly Crystalline MoS_2 Thin Layers on Insulating Substrates. *Nano Lett.* **2012,** *12* (3), 1538-1544.
31. Lee, Y. H.; Zhang, X. Q.; Zhang, W.; Chang, M. T.; Lin, C. T.; Chang, K. D.; Yu, Y. C.; Wang, J. T. W.; Chang, C. S.; Li, L. J., Synthesis of Large-Area MoS_2 Atomic Layers with Chemical Vapor Deposition. *Adv. Mater.* **2012,** *24* (17), 2320-2325.
32. Salmeron, M.; Somorjai, G.; Chianelli, R., A LEED-AES study of the structure of sulfur monolayers on the Mo (100) crystal face. *Surf. Sci.* **1983,** *127* (3), 526-540.
33. Wilson, J., LEED and AES study of the interaction of H_2S and Mo (100). *Surf. Sci.* **1975,** *53* (1), 330-340.
34. Lin, Y.-C.; Zhang, W.; Huang, J.-K.; Liu, K.-K.; Lee, Y.-H.; Liang, C.-T.; Chu, C.-W.; Li, L.-J., Wafer-scale MoS 2 thin layers prepared by MoO_3 sulfurization. *Nanoscale* **2012,** *4* (20), 6637-6641.
35. Bolotin, K. I.; Sikes, K. J.; Jiang, Z.; Klima, M.; Fudenberg, G.; Hone, J.; Kim, P.; Stormer, H. L., Ultrahigh electron mobility in suspended graphene. *Solid State Commun.* **2008,** *146* (9–10), 351-355.
36. Lee, C.; Wei, X.; Kysar, J. W.; Hone, J., Measurement of the Elastic Properties and Intrinsic Strength of Monolayer Graphene. *Science* **2008,** *321* (5887), 385-388.
37. Kim, K. S.; Zhao, Y.; Jang, H.; Lee, S. Y.; Kim, J. M.; Kim, K. S.; Ahn, J.-H.; Kim, P.; Choi, J.-Y.; Hong, B. H., Large-scale pattern growth of graphene films for stretchable transparent electrodes. *Nature* **2009,** *457* (7230), 706-710.
38. Nair, R.; Blake, P.; Grigorenko, A.; Novoselov, K.; Booth, T.; Stauber, T.; Peres, N.; Geim,

A., Fine structure constant defines visual transparency of graphene. *Science* **2008,** *320* (5881), 1308-1308.

39. Lee, Y.; Bae, S.; Jang, H.; Jang, S.; Zhu, S.-E.; Sim, S. H.; Song, Y. I.; Hong, B. H.; Ahn, J.-H., Wafer-scale synthesis and transfer of graphene films. *Nano lett.* **2010,** *10* (2), 490-493.
40. Park, J.; Jo, S. B.; Yu, Y. J.; Kim, Y.; Yang, J. W.; Lee, W. H.; Kim, H. H.; Hong, B. H.; Kim, P.; Cho, K., Single-Gate Bandgap Opening of Bilayer Graphene by Dual Molecular Doping. *Adv. Mater.* **2012,** *24* (3), 407-411.
41. Wu, J.; Xie, L.; Li, Y.; Wang, H.; Ouyang, Y.; Guo, J.; Dai, H., Controlled chlorine plasma reaction for noninvasive graphene doping. *J. Am. Chem. Soc.* **2011,** *133* (49), 19668-19671.
42. Guo, B.; Liu, Q.; Chen, E.; Zhu, H.; Fang, L.; Gong, J. R., Controllable N-doping of graphene. *Nano Lett.* **2010,** *10* (12), 4975-4980.
43. Kim, S. J.; Ryu, J.; Son, S.; Yoo, J. M.; Park, J. B.; Won, D.; Lee, E.-K.; Cho, S.-P.; Bae, S.; Cho, S., Simultaneous etching and doping by Cu-stabilizing agent for high-performance graphene-based transparent electrodes. *Chem. Mater.* **2014,** *26* (7), 2332-2336.
44. Sandoval, S. J.; Yang, D.; Frindt, R.; Irwin, J., Raman study and lattice dynamics of single molecular layers of MoS_2. *Phys. Rev. B* **1991,** *44* (8), 3955.
45. Mak, K. F.; Lee, C.; Hone, J.; Shan, J.; Heinz, T. F., Atomically thin MoS_2: a new direct-gap semiconductor. *Phys. Rev. Lett.* **2010,** *105* (13), 136805.
46. Chiritescu, C.; Cahill, D. G.; Nguyen, N.; Johnson, D.; Bodapati, A.; Keblinski, P.; Zschack, P., Ultralow thermal conductivity in disordered, layered WSe_2 crystals. *Science* **2007,** *315* (5810), 351-353.
47. Muratore, C.; Varshney, V.; Gengler, J.; Hu, J.; Bultman, J.; Smith, T.; Shamberger, P.; Qiu,

B.; Ruan, X.; Roy, A., Cross-plane thermal properties of transition metal dichalcogenides. *Appl. Phys. Lett.* **2013,** *102* (8), 081604.

48. Ajit, K., Thermal anisotropy in nano-crystalline MoS_2 thin films. *Phys. Chem. Chem. Phys.* **2014,** *16* (3), 1008-1014.

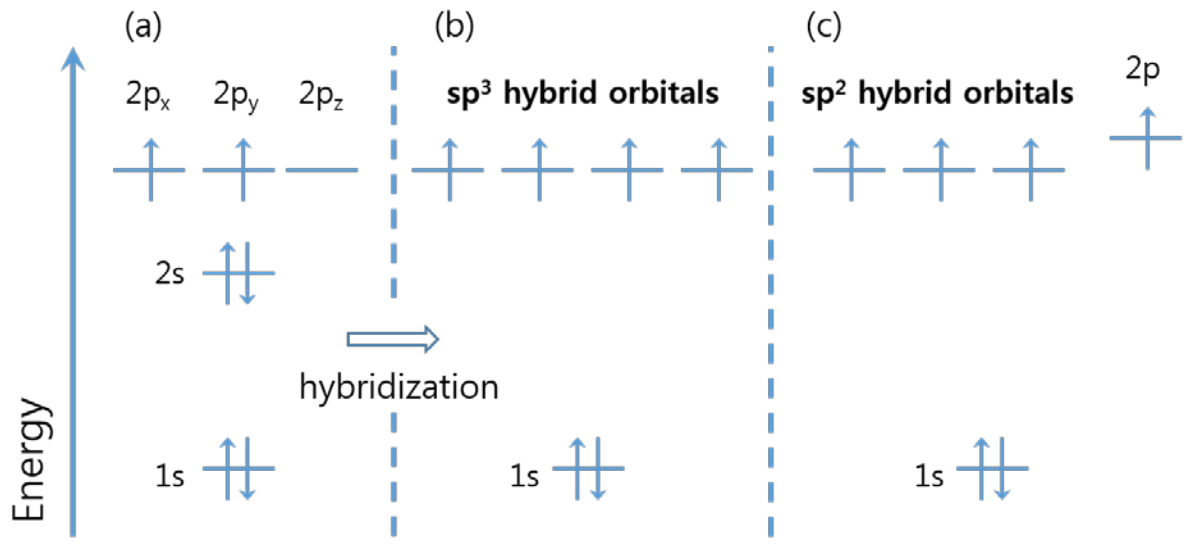

Figure 1. atomic orbital diagram of a carbon atom. The four electrons in the doubly occupied spherical 2s orbital and the half occupied dumbbell-shaped 2p-orbitals participate in the chemical bonding of carbon. (a) Ground state, (b) sp3-hybridized as in diamond, and (c) sp2-hybridized as in graphene.

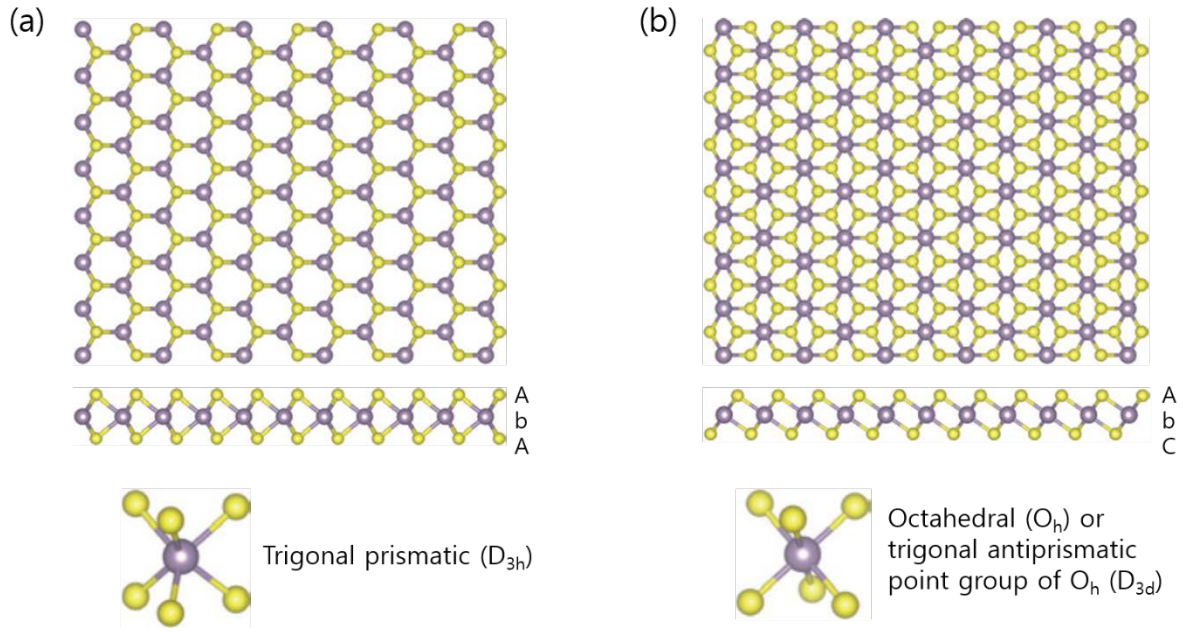

Figure 2. c-Axis and [$11\bar{2}0$] section view of single-layer TMDs with trigonal prismatic (a) and octahedral (b) coordination. Atom color code: purple, metal; yellow, chalcogen. The labels AbA and AbC represent the stacking sequence where the upper- and lower-case letters represent chalcogen and metal elements, respectively.

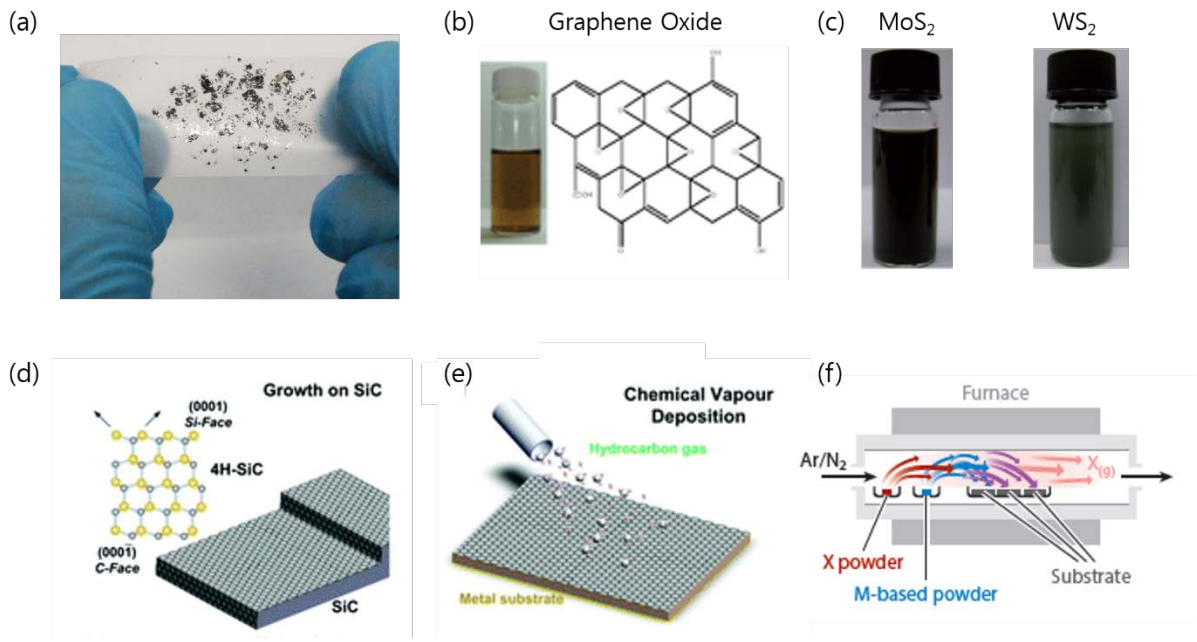

Figure 3. Obtaining the various of methods of layered 2D materials (a) mechanical exfoliation, (b) chemically exfoliated graphene oxide (c) chemically exfoliated MoS_2 and WS_2, (d) epitaxial growth, (e) chemical vapor deposition method of graphene, and (f) of TMDs

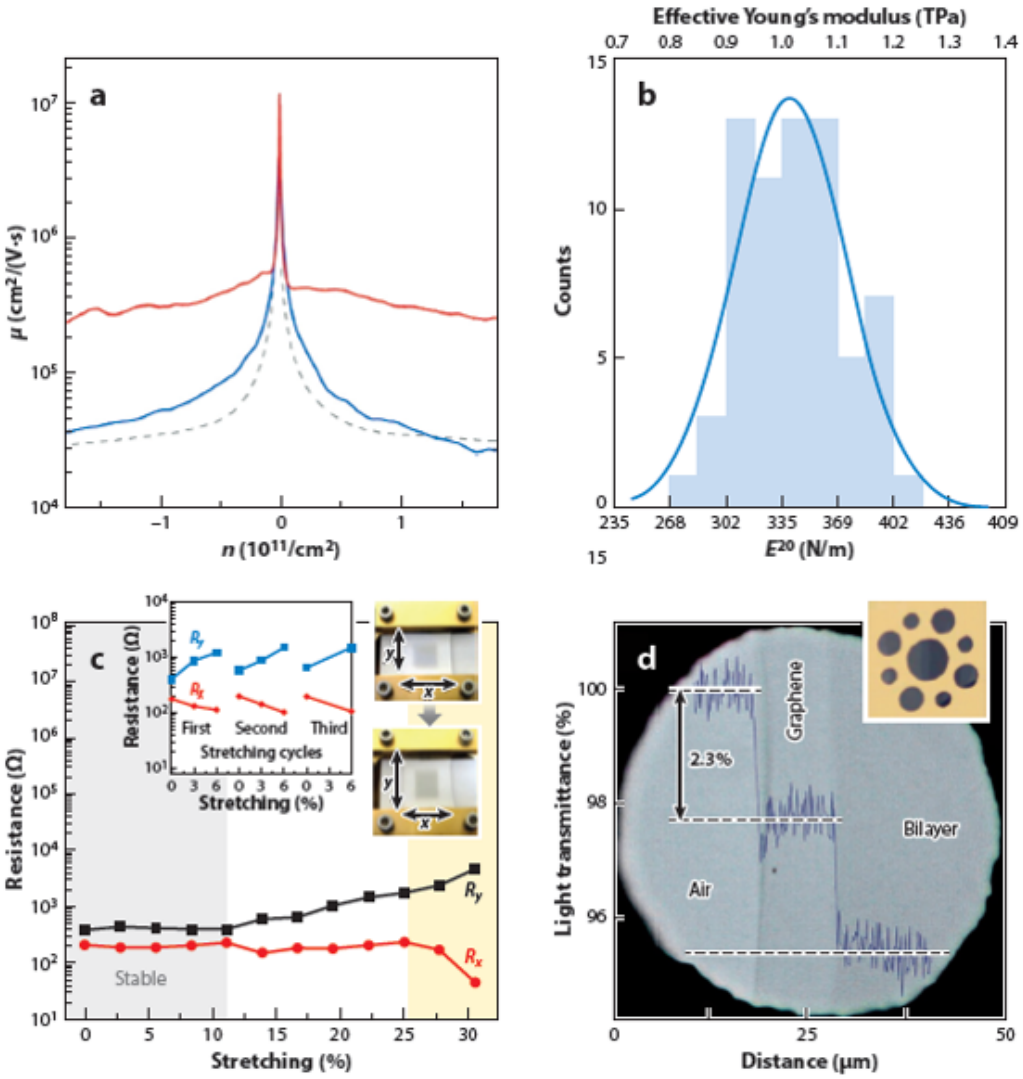

Figure 4. The outstanding properties of graphene for flexible electronics. (a) Mobility as a function of carrier density of a suspended graphene device shows its high electron mobility. (b) Elastic stiffness distribution of graphene film on a silicon oxide cavity. (c) The resistance change of a graphene film transferred onto a polydimethylsiloxane substrate depends on isotropic stretching. (Insets) The resistance change and movement images depend on stretching cycles and stretching direction. (d) Transmittance of partially covered single-layer and bilayer graphene. The inset shows the metal support structure covered with graphene layers.

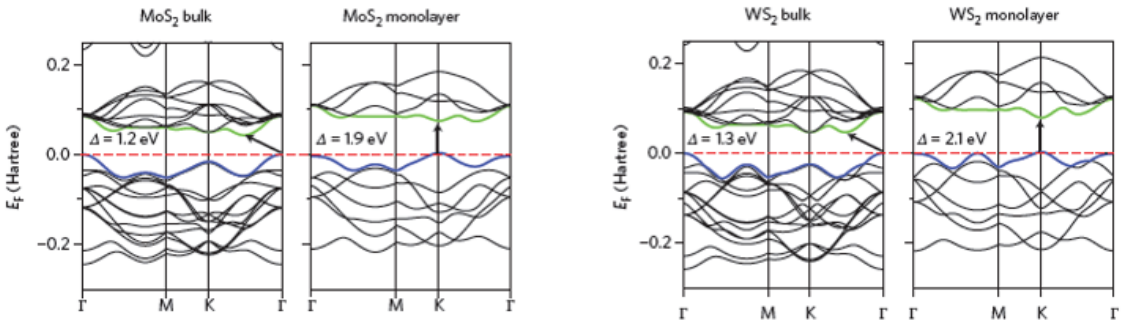

Figure 5. a,b, Band structures calculated from first-principles density functional theory (DFT) for bulk and monolayer MoS_2 (a) and WS_2 (b). The horizontal dashed lines indicate the Fermi level. The arrows indicate the fundamental bandgap (direct or indirect). The top of the valence band (blue) and bottom of the conduction band (green) are highlighted.

Chapter 2

Graphene Growth at Low-Temperature[2]

[2] K. Choi et al. Selective Growth of Graphene by Chemical Vapor Deposition on Patterned Cu-Ni Alloy Catalyst.

Introduction

Since the discovery of graphene by mechanical exfoliation from graphite in 2004,[1] graphene has been intensively explored. Graphene synthesized by the use of the chemical vapor deposition (CVD) method not only facilitates a large-scale growth, as large as 30 inch, but also reflects similar distinguished properties of exfoliated graphene such as half-integer quantum Hall effect, Shubnikov-de Haas oscillations, and remarkable optical transparency.[2-6] These features make CVD graphene a promising material for nano-electronics. However, reducing the growth temperature and time as well as simplifying the fabrication steps of CVD graphene devices still remain as major challenges for practical applications for two important reasons.

First, high thermal energy is required to produce high quality graphene, leading to the synthesis temperature as high as 1000 ºC.[7, 8] This is because high dehydrogenation and dissociation energy of methane (CH_4) have hindered lowering the growth temperature, even though methane has been predominantly used as a precursor. Moreover, higher activation barrier energy of each decomposition step of methane on Cu catalyst than that on Ni catalyst requires a longer growth time (~30 min).[9-11] To endure such harsh condition, a CVD chamber should be made of quartz, which produces inevitable impurities such as silica nanoparticles. These impurities could exert adverse effects on the electrical properties of graphene. In this regard, replacing methane with other hydrocarbon sources such as ethylene (C_2H_4) and acetylene (C_2H_2) as well as utilizing binary metal alloy with high catalytic effective metal and high carbon solubility such as Ni, and Co are key factors in lowering the growth temperature and growth time.[12-14]

Secondly, applying micro- or nano-structured patterns are necessary to tune the physical and electrical properties of graphene and introduce it for a great diversity of applications. Indeed, adequately patterned graphene has been employed as terahertz devices, transparent conducting electrodes, and semiconductor electronics.[15-17] However, post-lithography such as e-beam- or photo-lithography patterning of graphene after growth causes substantial contamination by polymer residues.[18, 19] In addition, reactive ion etching (RIE) can induce structural and chemical alterations, leading to the degradation of graphene's exceptional properties.[20] Recently, there have been many efforts to overcome these challenges with top-down approaches. Safron *et al.*[21] have successfully demonstrated micro- and nano-patterned graphene by the use of barrier-guided CVD. Hofmann *et al.*[22] have also showed a solution-based approach of scalable and high resolution patterning of CVD graphene. Unfortunately, previously reported methods exploited methane and Cu catalyst, which thus require high thermal energy and long growth time.

Here, we report a simple method to prepare uniformly and selectively grown monolayer graphene by substituting the carbon precursor and catalyst. Significant synergetic effect between Cu-Ni alloy and acetylene contributes to lower the growth temperature, as low as 800 ºC, and dramatically reduce the growth time (~1 min). Furthermore, these new recipes have been designed to selectively grow graphene with a desirable shape due to the difference in the activation barrier energy between Cu and Ni. The organic field-effect transistors (OFETs) based on the selectively grown graphene electrodes exhibit enhanced performance compared to photolithography-patterned graphene electrode. We expect that our method would enable the cost-effective high-performance synthesis and applications of graphene by providing lower synthesis temperature that does not require quartz chambers and by simplifying the

complicated post-growth pattering processes of graphene electrodes.

Experimental

Sample preparation. Monolayer graphene was grown on a Cu-Ni in a quartz tube using CVD methods. The Cu-Ni was heated at 800 °C for 40 min under a 5 sccm H_2 flow, and then 0.5 sccm C_2H_2 was inserted to permit graphene growth over 1 min. Finally, the furnace was rapidly cooled to room temperature under a H_2 flow. To protect the graphene, the PMMA solution was applied onto the graphene/Cu-Ni using a spin-coater. The Cu-Ni was etched away using 0.05 M ammonium persulfate over 7 hours. The floating graphene layer and the PMMA support film were transferred onto the target substrate.

*Device fabrication***.** Pentacene OFETs were fabricated by depositing a 50 nm thick pentacene (Aldrich Co.) active layer (at a rate of 0.2 Å/s) onto the substrates supporting graphene S/D electrodes using an organic molecular beam deposition system.

Characterization. The surfaces of the graphene were imaged using an optical microscope (DSX-500, OLYMPUS) and a field-emission scanning electron microscope (AURIGA, Carl Zeiss). Electron microscopic analysis was carried out using in-situ UHV-TEM (JEOL, JEM 2010V) operated at 200 keV. The Raman spectra were measured by a Raman spectrometer (RM 1000-Invia, Renishaw, 514nm). The C1s core level bands of graphene were acquired using an Axis-HIS (Kratos Inc.). The sheet resistance was measured with 4-point probe nanovoltmeter (Keithley 6221), and the current-voltage curve was measured by Agilent B2912A. The electrical characteristics of the pentacene FETs were measured using Keithley 4200 SCS in a N2-rich glove box.

Results and discussion

Copper is the most commonly used catalyst for synthesizing high-quality graphene with the use of methane. This is because the low solubility of carbon in Cu catalyst facilitates a self-limited growth, which predominantly synthesizes homogeneous graphene. However, high thermal energy is needed to decompose methane on Cu, leading to temperature as high as 1000 ºC. To lower the growth temperature, there have been many efforts to replace methane with other hydrocarbon sources such as ethylene and acetylene.[10, 23] Although acetylene is well known for lower decomposition temperature than methane, its low growth temperature (below 1100 K) allows acetylene to produce other polymer states instead of its entire decomposition.[24] It is thus necessary to provide harsh chamber condition at high temperature or high pressure by the use of H_2 and Ar.[25] The Raman spectra of graphene grown on Cu catalyst with acetylene at 1000 °C exhibited similar results to that of turbostratic graphite (Figure 1b). In addition, the deconvoluted spectra of XPS showed sp^2 C-C and excessive oxygen-containing groups such as C-O and O-C=O bonds (Figure 1c). These results suggest that acetylene is an improper match with Cu catalyst to produce high quality graphene. Alternatively, we proposed the use of Cu-Ni binary alloy catalyst as Ni catalyst in a binary alloy plays two important roles: 1) catalytic effect on a dissociation of hydrocarbon molecules.[26, 27] and 2) high carbon solubility. Adsorbed hydrocarbon atoms on Ni surface are more rapidly dissociated to carbon atoms than on Cu surface and diffuse into metal bulk, which happens spontaneously due to the carbon solubility (1.2 at.% at 1000 °C). Although diffused carbon species would precipitate on the surface during cooling, this process leads to produce inhomogeneous graphene. This is because the high carbon solubility of Ni does not control the amount of segregated carbon species from the bulk state. On the other hand, the carbon solubility of Cu-Ni alloy is extremely constrictive

(0.07 at.% at 1000 °C)[28] and the Cu components restrain the dissolved carbon atoms during precipitation process. According to the two roles of Ni that are complementary to each other, high-quality and uniformly monolayer graphene can be grown on Cu-Ni alloy, which was evidenced by SEM, Raman, and XPS spectra (Figure 1d,e,f).

Figure 2a illustrates the differences in the progress of growth and the interaction between hydrocarbon and metal catalyst such as Cu and Cu-Ni for the same elapsed time. We consider that only hydrocarbon molecules are adsorbed on metal surface because the adsorption of carbon atoms requires significantly high activation energy. Alternatively, the carbon atoms are generated by thermal and hydrogen-induced dissociation of adsorbed hydrocarbon molecules on the surface of Cu catalyst. The atoms continue to diffuse on the surface and eventually ripens to form the initial graphene flake. Although each of these processes needs high activation barrier energy in the region only of Cu,[9] the sequence of such events are spontaneous and accelerated in the region of Cu-Ni due to its high carbon solubility and the catalytic effect.

We have explored to synthesize high-quality graphene against three parameters: 1) growth temperature, 2) thickness of Ni catalyst, and 3) acetylene flow rate. In our CVD method, a Cu-Ni (50 ~ 500 nm) alloy in the quartz tube was heated to 700 ~ 1000 ºC for 40 min with 5 sccm H_2 at 25 mtorr. After heating, graphene was grown on Cu-Ni alloy for 1 min with a gas mixture of from 0.5 ~ 10 sccm acetylene and 5 sccm hydrogen (H_2). The Cu-Ni alloy was then rapidly cooled at room temperature with only hydrogen at 25 mtorr. The representative Raman spectra of graphene on temperature variation from 700 ºC to 1000 ºC are shown in Figure 3. A low intensity of D band is observed above 800 ºC, while D band of graphene grown at 700 ºC is very large; it is presumed that acetylene is incompletely decomposed as mentioned. In addition, show Raman spectra of graphene and plotted 2D/G and D/G ratio with respect to different Ni

thickness (50 ~ 500 nm), respectively (Figure 4a,b). An enhanced graphitic quality with increasing Ni thickness was confirmed, which is evidenced by a 6-fold decrease in the D/G ration from 0.92 (Ni thickness of ~50 nm) to 0.14 (Ni thickness of ~300 nm). However, in case of much amounts of Ni (500 nm) on binary alloy surface (with higher carbon solubility), partially multilayer graphene with decrease in 2D/G ratio was exhibited. These results indicate that sufficient concentration of Ni atoms on the surface of binary metal alloy is vital for synthesizing the high-quality graphene. Interestingly, when very low concentration of acetylene flow was injected into the CVD chamber, selectively patterned high-quality graphene was obtained along the region of Ni pattern on Cu foil. The ratio of 2D/G peak intensities remained nearly constant when acetylene flow was a variable in the experiment from 0.5 to 10 sccm. However, the ratio of D/G peak intensities is subjected to extreme changes (Figure 4c,d).[29] These results are presumably due to much hydrocarbon gases rather than meeting with a disturbance to the large-grain graphene. Graphene flakes are densely sprung up across the surface of binary metal alloy due to excessive hydrocarbon. The small lateral size of graphene grain is stitched to each other so that the areas of grain boundaries are enormously generated. Thus, increased D peak intensity is thought to be originated from the grain boundary.

Next, we demonstrated the selective growth of monolayer graphene. Figure 2b shows the pre-pattern of Ni (300 nm) on Cu foil prior to the synthesis process. Ni films were deposited as ‘Graphene Research Laboratory’. Following the synthesis by the CVD method, Ni film was diffused into the Cu foil along the pre-pattern, while Ni atoms are hardly diffused to the lateral direction due to low-temperature. Hence, we could obtain selective monolayer graphene (SMG) of identical shapes with the pre-pattern of Ni. Figure 2c shows the optical microscope image of SMG transferred on SiO_2/Si, synthesized on the pre-patterned catalysts. Based on the clear

difference in the contrasts between graphene and non-graphene regions, we could ascertain that graphene was well-grown selectively along the pre-pattern. Figure 2d shows the Raman intensity mapping of the 2D peak in the region of red box in Figure 2c. The result exhibits that graphene has well-defined pattern and the intensity of 2D band is clearly distinguished from the background. Therefore, we could confirm that our CVD process is a powerful method to synthesize SMG.

To further evaluate the characteristics of resulting graphene achieved by low-temperature (800 ºC), Cu-Ni (35 μm-300 nm), and acetylene (0.5 sccm), we carried out Raman, electrical, and TEM analysis transferred on target substrates such as SiO_2/Si and TEM grid. The Raman spectra of our CVD graphene with 2D/G ratio of ~2.8 and D/G ratio of ~0.1 show a similar trend with conventional graphene grown on Cu catalyst at high temperature (Figure 5a). In addition, the full width at half maximum (FWHM) fitted by Lorentzian of 2D peak (~2685 cm^{-1}) has the value of ~33 cm^{-1}. We randomly chose 25 x 25 μm^2 regions on graphene and compiled its 2D/G and D/G peak intensity of Raman mapping to confirm the uniformity of monolayer graphene (Figure 5b,c). The measured area has an average 2D/G ratio of ~2.71 and D/G ratio of ~0.15, which established the high quality monolayer graphene. Indeed, Figure 5d shows that the mobility of graphene is as high as 2769 $cm^2/V{\cdot}s$, measured by the field-effect transistor (FET) at room temperature (mean mobility of ~ 2593.6 $\pm$ 156.5 $cm^2/V{\cdot}s$). The sheet resistance of resulting graphene is as low as ~ 386.3 $\pm$ 33 Ω/sq. after BI-doping, which corresponds to ~60 % reduction from that of pristine graphene (~1082 $\pm$ 63 Ω/sq.) (Figure 6).[30] The high resolution TEM image and selected area electron diffractions (SAED) suggested the highly crystallintity and monolayer graphene grown on Cu-Ni alloy (Figure 5e,inset). The intensity of inner spots$\{\bar{1}100\}$ is more intense than the outer spots$\{\bar{1}2\bar{1}0\}$, which implies the

characteristic mark of monolayer graphene. In case of our resulting graphene, two distinct spots within the inner and outer indicate that two kinds of dominant grains are stitched. However, graphene grown on Cu-Ni alloy at high temperature presented larger sizes of grain because the concentration of Ni atom existed in the alloy surface was decreased with increased growth temperature (Figure 7). Figure 5f shows that monolayer graphene produced by our recipe has well-defined hexagonal structure and individual carbon atoms are visible by atomic resolution scanning transmission electron microscopy-high angle annular dark field (STEM-HAADF). Thus, we could further confirm that graphene can be synthesized at low temperature with extremely short growth time.

To better understand the selective growth of graphene, we tried to identify the difference between the catalytic role of Cu and Cu-Ni alloy. First, in order to explore the initial evolving flake on the surface of Cu, we have confirmed the selective growth conditions by graphene coverage as a function of temperature. Figure 8 shows representative SEM images of graphene flakes depending on various growth temperature. At high temperatures (900, 950, and 1000 ºC), they exhibited high graphene coverage, indicating the growth is not suppressed on the Cu region and it is impossible to conduct a selective growth. In contrast, graphene coverage was rarely observed at relatively low temperature, below 850 ºC, indicating the growth is well suppressed on the Cu region (Figure 9b). In conclusion, we made a choice on the temperature window of 700 ~ 850 ºC and the growth time window of 0 ~ 4 min (Figure 9c). To extract the activation energy, we calculated the growth rate at each time point for different temperatures. At below 800 ºC, there was no graphene flake on the surface of Cu under 1 min (Figure 9a). However, graphene flakes were gradually appeared with the elapsed time, regardless of the temperature. The flake areal enlargement is visible with increasing growth time as well as the

growth temperature (Figure 10). Using these conditions, the activation energy was obtained by the Arrhenius plot of growth rates (Figure 9d). Acquired Arrhenius plot suggests a 3.5 eV barrier for the growth rates as a function of temperature. By exploiting this activation energy, the rate-determining step could be clearly defined. As previously reported, the synthesis of graphene passes through four phases; (1) the adsorption of hydrocarbon on Cu (we eliminated the adsorption of carbon atoms on copper owing to its tremendously large activation energy of 5.5 eV.); (2) catalytic dissociation and dehydrogenation; (3) surface diffusion; (4) incorporation of carbon species. As the adsorption of hydrocarbons on copper requires zero activation energy and the surface diffusion of carbon atoms and clusters exhibit activation energy barrier of about 0.1 and 0.8 eV, respectively, these processes can be ruled out as the rate-determining step.[9] Instead, the energies of the catalytic dissociation and dehydrogenation of acetylene are analogous to our activation energy.[31] Therefore, we suggest that the rate determining step is the decomposition and dehydrogenation of acetylene on Cu for producing the carbon species. Here, we did not calculate the activation energy on Cu-Ni alloy due to the carbon solubility, which induce carbon atoms to spontaneously diffuse into the bulk.[32, 33]

To explore the possibility of electronic applications, we built pentacene-based OFETs using monolayer graphene electrodes. Employing monolayer graphene as the electrodes of OFETs is particularly advantageous due to its tendency for self-organization of the overlying organic semiconductors.[34, 35] Graphene-based OFETs have further advantages such as its tunable work function, low sheet resistance, flexibility, and low contact resistance. The electrical properties of OFETs were measured using various electrodes: selectively grown graphene electrodes, patterned graphene electrodes by photolithography, and Au electrodes. Figure 11a,c show the transfer and output characteristics of these OFETs, respectively. The

field-effect mobility (μ) was obtained from the slope of a plot of the square root of drain current (I_D) versus gate voltage (V_G) in the saturation current regime (drain voltage, V_D = 80 V) using the equation, $I_D = \mu C_i W(2L)^{-1}(V_G - V_{th})^2$, where C_i is the capacitance per unit area of the gate dielectrics (10 nF/cm^2) and V_{th} is the threshold voltage. All electrical characteristics of these OFETs are summarized in Table 1. The OFETs using selectively grown graphene electrodes show higher mobility and on-state current than graphene electrodes by photolithography. These results indicate that unremoved residues on the surface of graphene, remained after photolithography process, impede the hole injection for pentacene films. In other words, polymer residues serve as a hole blocking layer. On the other hands, the SMG electrodes fabricated by the pre-pattern method does not require additional patterning processes. Raman spectra of graphene in the dark region is well synthesized but graphene does not exist in bright region (Figure 12). The SMG devices manifested the highest transistor performance, with an average mobility value of 0.31 $\pm$ 0.07 cm^2/Vs and on-off ratio of 5.67 $\times$ 10^6. We also fabricated OFETs made of Au/Cr electrodes, but these devices showed very poor performance, compared to graphene electrodes. This is because CVD graphene had flat surface roughness and better thermal and chemical stability than other metal electrodes, thereby facilitating optimal molecular ordering and grain growth of pentacene films. It should be noted that the contact resistances of SMG electrode decreased from 0.4 to 0.242 MΩcm as V_G varied from -40 to -100 V, calculated using the transfer line method (Figure 13), which is one order of magnitude lower than that of other electrodes (Figure 11b). Thus, SMG electrode can further enhance charge injection and transport.

Conclusion

In summary, we first demonstrated the high-quality and selective growth of monolayer graphene on Cu-Ni alloy using acetylene at low-temperature as low as 800 ºC. Monolayer graphene can be selectively grown on pre-patterned Cu-Ni region while the growth is suppressed on the Cu only region possibly due to the higher activation barrier energy of graphene formation on Cu catalyst. The OFETs based on selectively grown graphene show better performance than the post-patterned graphene devices. The present method would be helpful to simplify the fabrication process of graphene devices and to lower the growth temperature for more cost-effective production of large area graphene films.

References

1. Novoselov, K. S.; Geim, A. K.; Morozov, S. V.; Jiang, D.; Zhang, Y.; Dubonos, S. V.; Grigorieva, I. V.; Firsov, A. A., Electric Field Effect in Atomically Thin Carbon Films. *Science* **2004,** *306*, 666-669.
2. Bae, S.; Kim, H.; Lee, Y.; Xu, X.; Park, J.-S.; Zheng, Y.; Balakrishnan, J.; Lei, T.; Ri Kim, H.; Song, Y. I.; *et al.* Roll-to-roll production of 30-inch graphene films for transparent electrodes. *Nat. Nanotechnol.* **2010,** *5*, 574-578.
3. Geim, A. K.; Novoselov, K. S., The rise of graphene. *Nat. Mater.* **2007,** *6*, 183-191.
4. Kim, K. S.; Zhao, Y.; Jang, H.; Lee, S. Y.; Kim, J. M.; Kim, K. S.; Ahn, J.-H.; Kim, P.; Choi, J.-Y.; Hong, B. H., Large-scale pattern growth of graphene films for stretchable transparent electrodes. *Nature* **2009,** *457*, 706-710.
5. Baker, A. M. R.; Alexander-Webber, J. A.; Altebaeumer, T.; McMullan, S. D.; Janssen, T. J. B. M.; Tzalenchuk, A.; Lara-Avila, S.; Kubatkin, S.; Yakimova, R.; Lin, C. T.; Li, L. J.; Nicholas, R. J., Energy loss rates of hot Dirac fermions in epitaxial, exfoliated, and CVD graphene. *Phys. Rev. B* **2013,** *87*, 045414.
6. Bonaccorso, F.; Sun, Z.; Hasan, T.; Ferrari, A. C., Graphene photonics and optoelectronics. *Nature Photon.* **2010,** *4*, 611-622.
7. Li, X.; Cai, W.; An, J.; Kim, S.; Nah, J.; Yang, D.; Piner, R.; Velamakanni, A.; Jung, I.; Tutuc, E.; Banerjee, S. K.; Colombo, L.; Ruoff, R. S., Large-Area Synthesis of High-Quality and Uniform Graphene Films on Copper Foils. *Science* **2009,** *324*, 1312-1314.
8. Zhang, W.; Wu, P.; Li, Z.; Yang, J., First-Principles Thermodynamics of Graphene Growth on Cu Surfaces. *J. Phys. Chem. C* **2011,** *115*, 17782-17787.
9. Mehdipour, H.; Ostrikov, K., Kinetics of Low-Pressure, Low-Temperature Graphene Growth: Toward Single-Layer, Single-Crystalline Structure. *ACS Nano* **2012,** *6*,

10276-10286.

10. Celebi, K.; Cole, M. T.; Choi, J. W.; Wyczisk, F.; Legagneux, P.; Rupesinghe, N.; Robertson, J.; Teo, K. B. K.; Park, H. G., Evolutionary Kinetics of Graphene Formation on Copper. *Nano Lett.* **2013,** *13*, 967-974.

11. Kim, H.; Mattevi, C.; Calvo, M. R.; Oberg, J. C.; Artiglia, L.; Agnoli, S.; Hirjibehedin, C. F.; Chhowalla, M.; Saiz, E., Activation Energy Paths for Graphene Nucleation and Growth on Cu. *ACS Nano* **2012,** *6*, 3614-3623.

12. Dai, B.; Fu, L.; Zou, Z.; Wang, M.; Xu, H.; Wang, S.; Liu, Z., Rational design of a binary metal alloy for chemical vapour deposition growth of uniform single-layer graphene. *Nat. Commun.* **2011,** *2*, 522.

13. Park, J.-U.; Nam, S.; Lee, M.-S.; Lieber, C. M., Synthesis of monolithic graphene–graphite integrated electronics. *Nat. Mater.* **2012,** *11*, 120-125.

14. Weatherup, R. S.; Dlubak, B.; Hofmann, S., Kinetic Control of Catalytic CVD for High-Quality Graphene at Low Temperatures. *ACS Nano* **2012,** *6*, 9996-10003.

15. Ju, L.; Geng, B.; Horng, J.; Girit, C.; Martin, M.; Hao, Z.; Bechtel, H. A.; Liang, X.; Zettl, A.; Shen, Y. R.; Wang, F., Graphene plasmonics for tunable terahertz metamaterials. *Nat. Nanotechnol.* **2011,** *6*, 630-634.

16. Ryu, J.; Kim, Y.; Won, D.; Kim, N.; Park, J. S.; Lee, E.-K.; Cho, D.; Cho, S.-P.; Kim, S. J.; Ryu, G. H.; Shin, H.-A. S.; Lee, Z.; Hong, B. H.; Cho, S., Fast Synthesis of High-Performance Graphene Films by Hydrogen-Free Rapid Thermal Chemical Vapor Deposition. *ACS Nano* **2013,** *8*, 950-956.

17. Yang, H.; Heo, J.; Park, S.; Song, H. J.; Seo, D. H.; Byun, K.-E.; Kim, P.; Yoo, I.; Chung, H.-J.; Kim, K., Graphene Barristor, a Triode Device with a Gate-Controlled Schottky Barrier. *Science* **2012,** *336*, 1140-1143.

18. Pirkle, A.; Chan, J.; Venugopal, A.; Hinojos, D.; Magnuson, C. W.; McDonnell, S.; Colombo, L.; Vogel, E. M.; Ruoff, R. S.; Wallace, R. M., The effect of chemical residues on the physical and electrical properties of chemical vapor deposited graphene transferred to SiO2. *Appl. Phys. Lett.* **2011,** *99*, 122108.

19. Kang, J.; Shin, D.; Bae, S.; Hong, B. H., Graphene transfer: key for applications. *Nanoscale* **2012,** *4*, 5527-5537.

20. Bai, J.; Zhong, X.; Jiang, S.; Huang, Y.; Duan, X., Graphene nanomesh. *Nat. Nanotechnol.* **2010,** *5*, 190-194.

21. Safron, N. S.; Kim, M.; Gopalan, P.; Arnold, M. S., Barrier-Guided Growth of Micro- and Nano-Structured Graphene. *Adv. Mater.* **2012,** *24*, 1041-1045.

22. Hofmann, M.; Hsieh, Y.-P.; Hsu, A. L.; Kong, J., Scalable, flexible and high resolution patterning of CVD graphene. *Nanoscale* **2014,** *6*, 289-292.

23. Ramón, M. E.; Gupta, A.; Corbet, C.; Ferrer, D. A.; Movva, H. C. P.; Carpenter, G.; Colombo, L.; Bourianoff, G.; Doczy, M.; Akinwande, D.; Tutuc, E.; Banerjee, S. K., CMOS-Compatible Synthesis of Large-Area, High-Mobility Graphene by Chemical Vapor Deposition of Acetylene on Cobalt Thin Films. *ACS Nano* **2011,** *5*, 7198-7204.

24. Kiefer, J. H.; Von Drasek, W. A.; Von Drasek, W. A., The mechanism of the homogeneous pyrolysis of acetylene. *Int. J. Chem. Kinet.* **1990,** *22*, 747-786.

25. Qi, M.; Ren, Z.; Jiao, Y.; Zhou, Y.; Xu, X.; Li, W.; Li, J.; Zheng, X.; Bai, J., Hydrogen Kinetics on Scalable Graphene Growth by Atmospheric Pressure Chemical Vapor Deposition with Acetylene. *J. Phys. Chem. C* **2013,** *117*, 14348-14353.

26. Morgante, A.; Modesti, S.; Bertolo, M.; Rudolf, P.; Rosei, R., Dissociation of Ch species on Ni(111): A HREELS study. *Surface Science Letters* **1989,** *211–212*, A149.

27. Rudolf, P.; Astaldi, C.; Modesti, S.; Rosei, R., Kinetics of the C2H2 dissociation on

Ni(111): A HREELS study. *Surf. Sci. Lett.* **1989,** *220*, L714-L718.

28. Wan, D.; Lin, T.; Bi, H.; Huang, F.; Xie, X.; Chen, I. W.; Jiang, M., Autonomously Controlled Homogenous Growth of Wafer-Sized High-Quality Graphene via a Smart Janus Substrate. *Adv. Funct. Mater.* **2012,** *22*, 1033-1039.

29. Kim, H.; Song, I.; Park, C.; Son, M.; Hong, M.; Kim, Y.; Kim, J. S.; Shin, H.-J.; Baik, J.; Choi, H. C., Copper-Vapor-Assisted Chemical Vapor Deposition for High-Quality and Metal-Free Single-Layer Graphene on Amorphous SiO2 Substrate. *ACS Nano* **2013,** *7*, 6575-6582.

30. Kim, S. J.; Ryu, J.; Son, S.; Yoo, J. M.; Park, J. B.; Won, D.; Lee, E.-K.; Cho, S.-P.; Bae, S.; Cho, S.; Hong, B. H., Simultaneous Etching and Doping by Cu-Stabilizing Agent for High-Performance Graphene-Based Transparent Electrodes. *Chem. Mater.* **2014,** *26*, 2332-2336.

31. Montgomery Jr, J. A.; Petersson, G. A., On the C-H bond dissociation energy of acetylene. *Chem. Phys. Lett.* **1990,** *168*, 75-78.

32. Shelton, J. C.; Patil, H. R.; Blakely, J. M., Equilibrium segregation of carbon to a nickel (111) surface: A surface phase transition. *Surf. Sci.* **1974,** *43*, 493-520.

33. Isett, L. C.; Blakely, J. M., Segregation isosteres for carbon at the (100) surface of nickel. *Surf. Sci.* **1976,** *58*, 397-414.

34. Lee, W. H.; Park, J.; Sim, S. H.; Jo, S. B.; Kim, K. S.; Hong, B. H.; Cho, K., Transparent Flexible Organic Transistors Based on Monolayer Graphene Electrodes on Plastic. *Adv. Mater.* **2011,** *23*, 1752-1756.

35. Jeong, Y. J.; Jang, J.; Nam, S.; Kim, K.; Kim, L. H.; Park, S.; An, T. K.; Park, C. E., High-Performance Organic Complementary Inverters Using Monolayer Graphene Electrodes. *ACS Appl. Mater. Inter.* **2014,** *6*, 6816-6824.

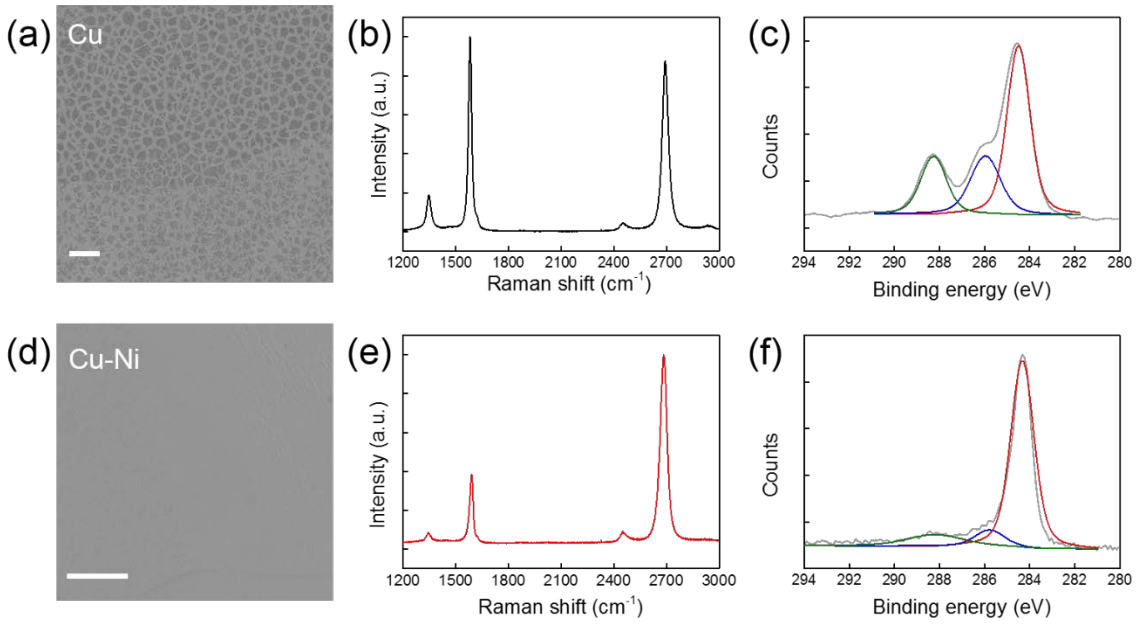

Figure 1. Analysis of graphitic carbon grown on Cu and graphene grown on Cu-Ni alloy at 1000°C. (a) SEM image of graphitic carbon. (b) Raman spectrum and (c) XPS spectrum of graphitic carbon transferred on SiO2/Si. (d) SEM image of graphene. (e) Raman spectrum and (f) XPS spectrum of graphene transferred on SiO2/Si. Scale bars, 500nm.

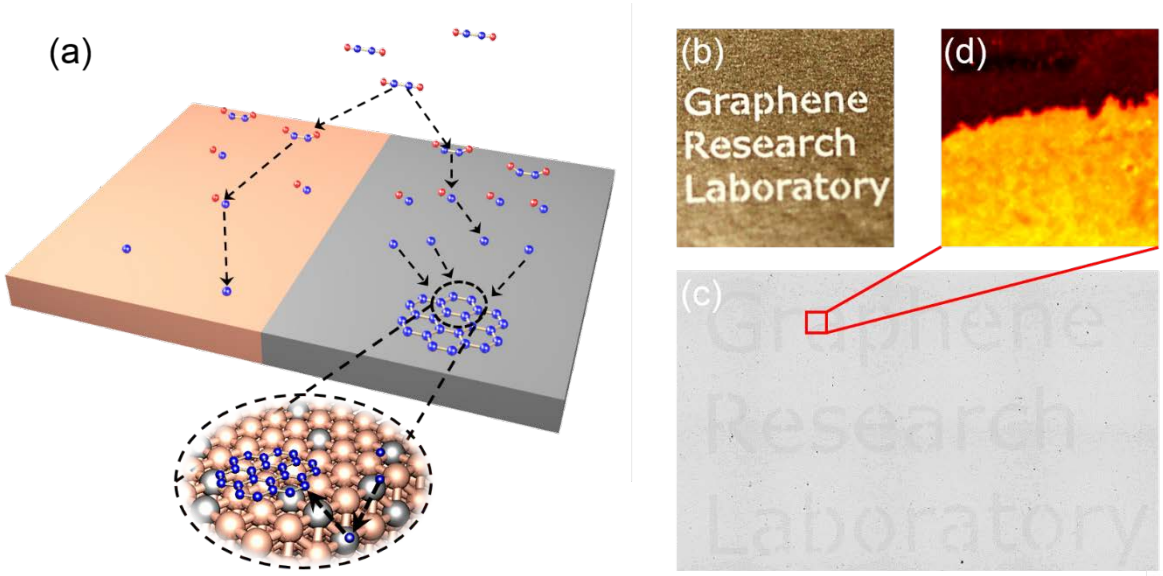

Figure 2. The optimization of high quality and selectively grown monolayer graphene (a) The difference in the interaction between hydrocarbon gas and metal catalysts as well as the growth mechanism corresponding to the nucleation and growth of monolayer graphene on Cu and Cu-Ni alloy at low pressure and temperature. In part of a binary metal alloy, a Ni catalyze the dissociation and dehydrogenation of acetylene. Inset scheme, the process indicates the growth mechanism in accordance with Ni-CVD process, including dissociated carbon atom diffuse into bulk from metal surface and then segregated carbon atoms can form the nucleation of monolayer graphene. Synthesis of selectively monolayer graphene (SMG) (b) Photograph of Ni pre-pattern on Cu foil. (Graphene Research Laboratory) (c) Optical microscope image of the selective growth of monolayer graphene, transferred on SiO_2/Si, synthesized from the catalysts shown in (b). Scale bars, 1mm. (d) Raman intensity mapping of 2D peak in the region of red box in (c).

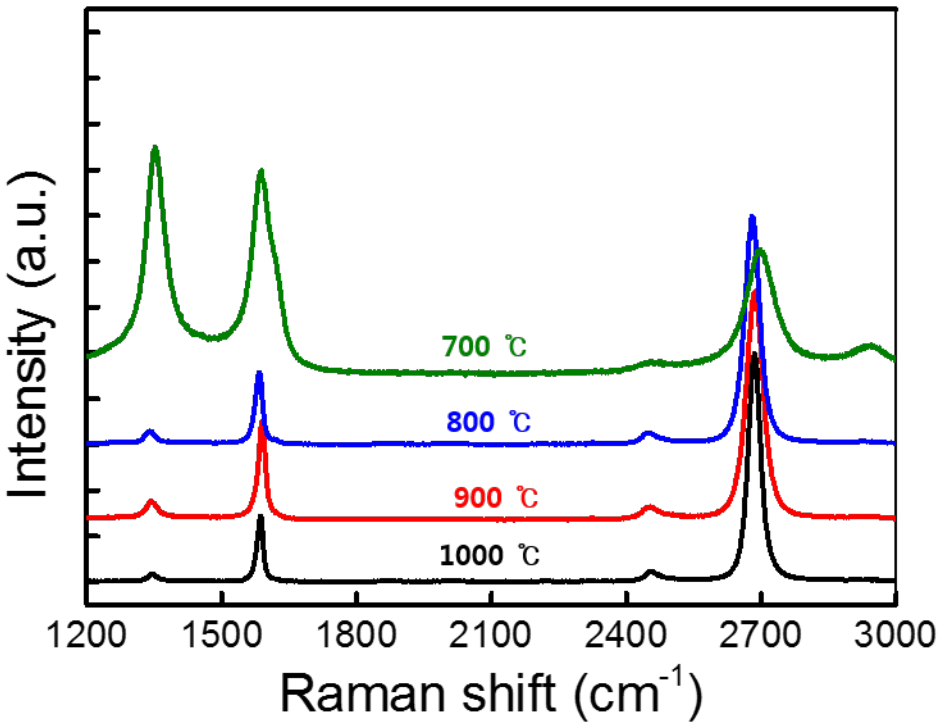

Figure 3. Raman spectrums of graphene grown on Cu-Ni on temperature variation from 700 ºC to 1000 ºC.

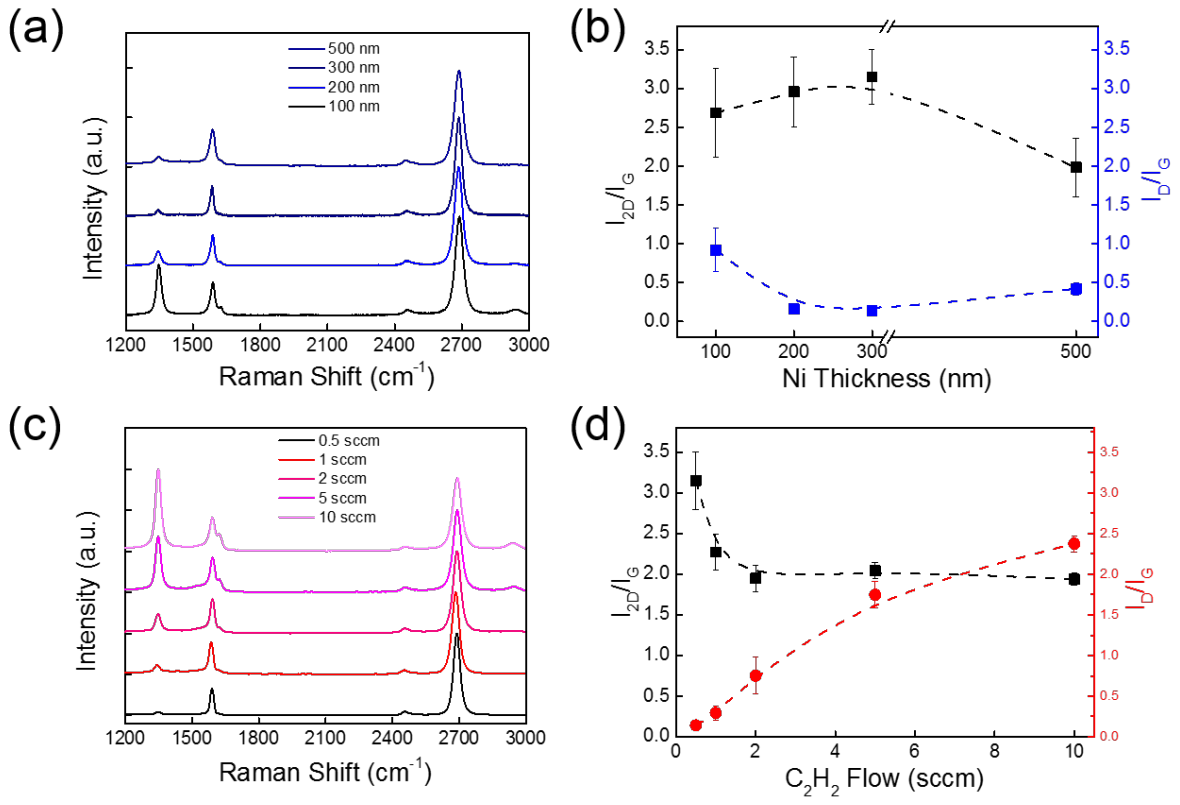

Figure 4. The optimization of high quality and selectively grown monolayer graphene (a) Raman spectra of graphene depending on Ni thickness. (b) The plot of 2D/G peak intensity ratio as a function of Ni thickness. (c) Raman spectra of graphene depending on C2H2 flow. (d) The plot of 2D/G peak intensity ratio as a function of C2H2 flow.

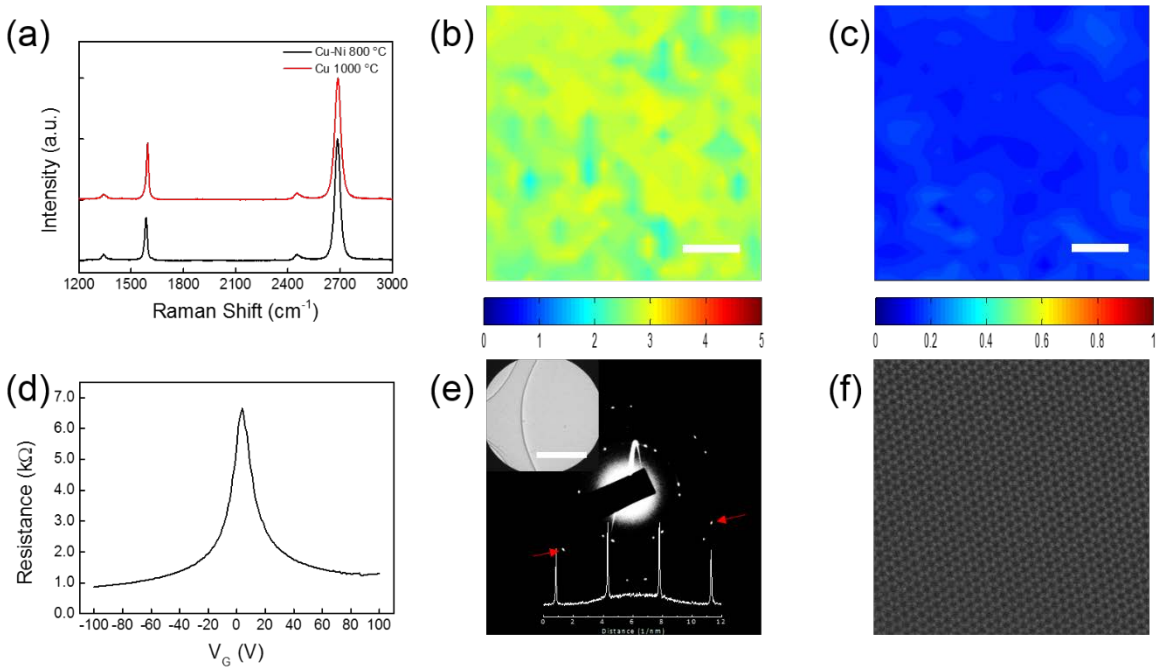

Figure 5. The optical characteristics of monolayer graphene grown on Cu-Ni alloy at 800 °C. (a) The comparison of Raman spectrum of monolayer graphene grown on Cu-Ni and on Cu at 1000 °C, transferred on SiO_2/Si. Raman mapping images of (b) 2D/G peak intensity and (c) D/G peak intensity of monolayer graphene. Scale bars, 5μm. (d) Electrical characteristic of the FET devices of monolayer graphene (e) SAED pattern and profile plots of diffraction spot intensities along red arrow. (inset) TEM image of monolayer graphene. Scale bar, 100 nm. (f) high-angle annular dark field (HAADF) image of monolayer graphene.

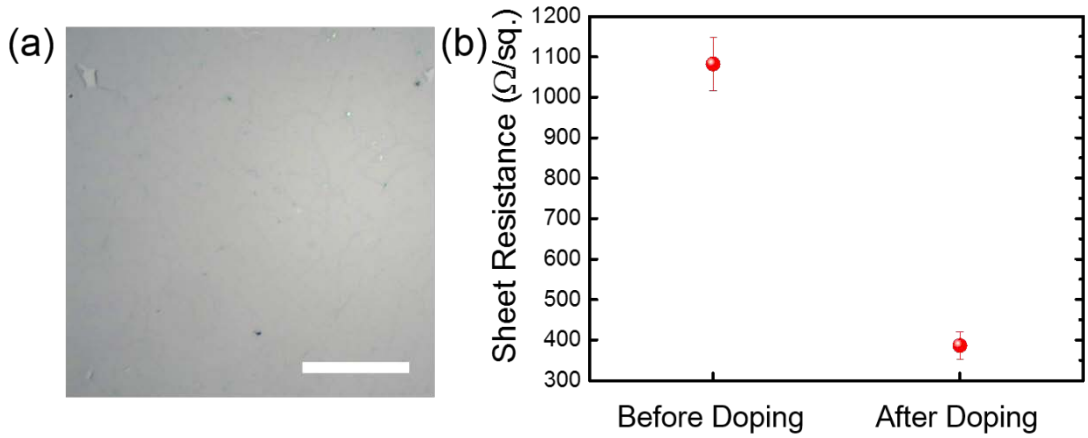

Figure 6. (a) Optical image of graphene. (b) The sheet resistance of graphene depending on doping

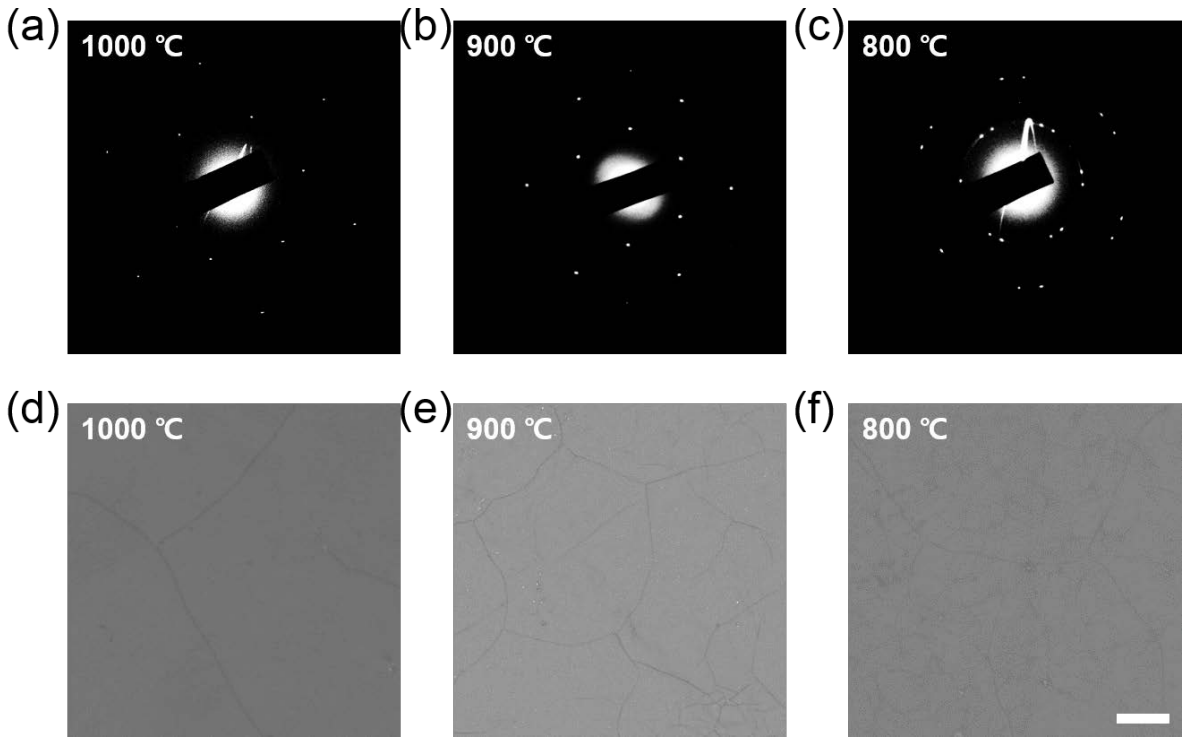

Figure 7. EM analysis of graphene as a function of temperature. (a) SEAD pattern of, and (d) SEM image of graphene grown at 1000 °C. (b) SEAD pattern of, and (e) SEM image of graphene grown at 900 °C. (c) SEAD pattern of, and (f) SEM image of graphene grown at 800 °C. Scale bar, 500 nm.

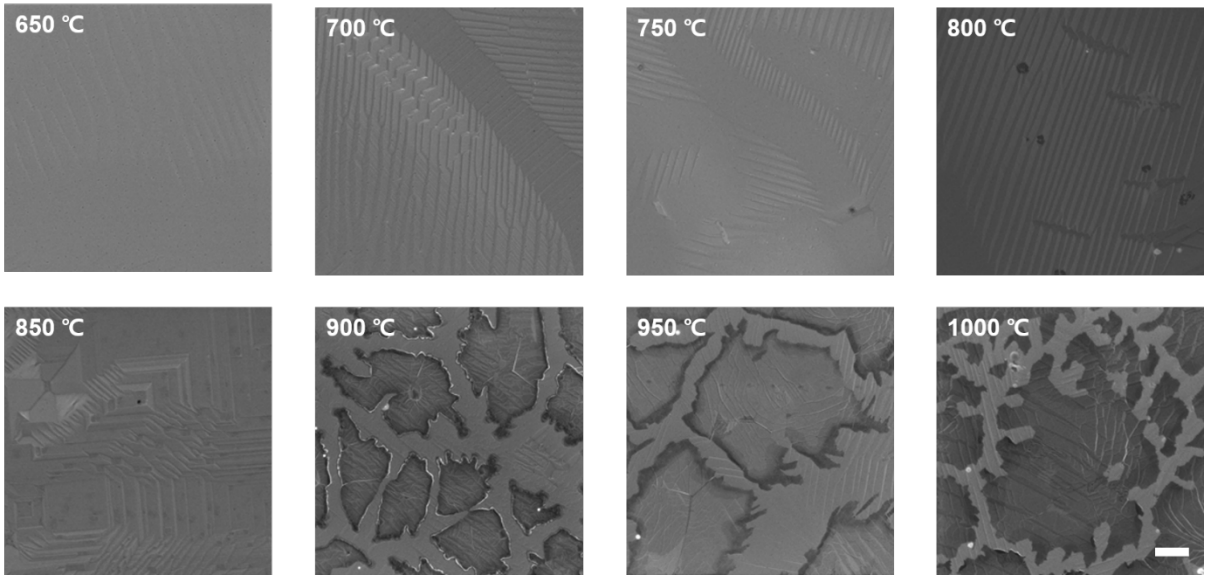

Figure 8. High-magnification SEM images of the flake of graphene on Cu catalyst for the calculation of graphene coverage depending on temperatures. Scale bar, 500 nm.

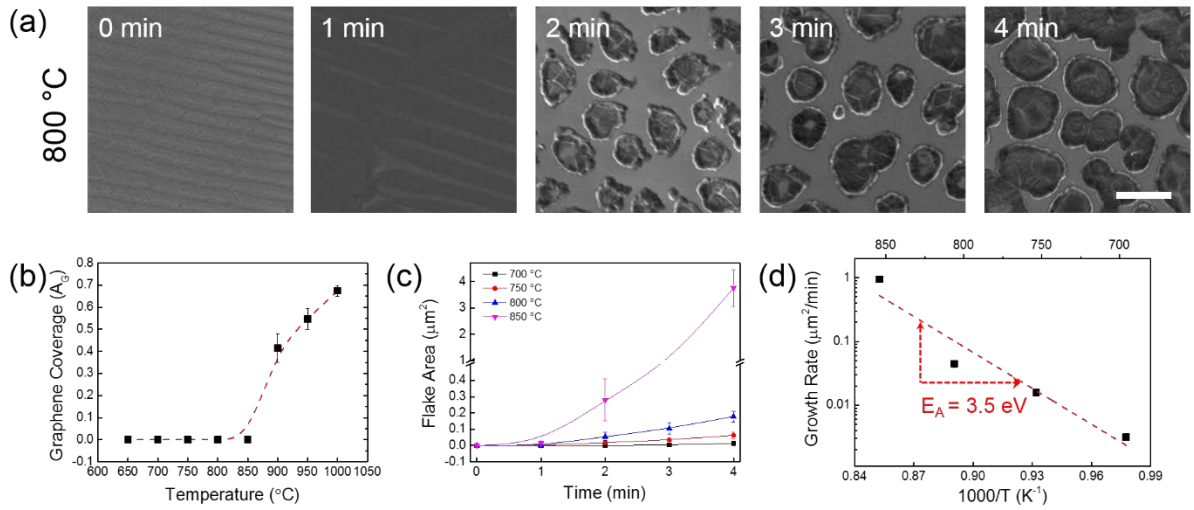

Figure 9. Analysis of kinetics of graphene growth. (a) Representative scanning electron micrographs showing flake evolution with the elapsed time, at 800 °C (scale bar: 500 nm). (b) As-grown graphene coverage on Cu as a function of temperature. (c) Evolution of the mean flake area with growth time for the four temperature. (700, 750, 800, and 850 °C) (d) Arrhenius plot of graphene growth rate as a function of 1000/T. Each point was obtained in (c).

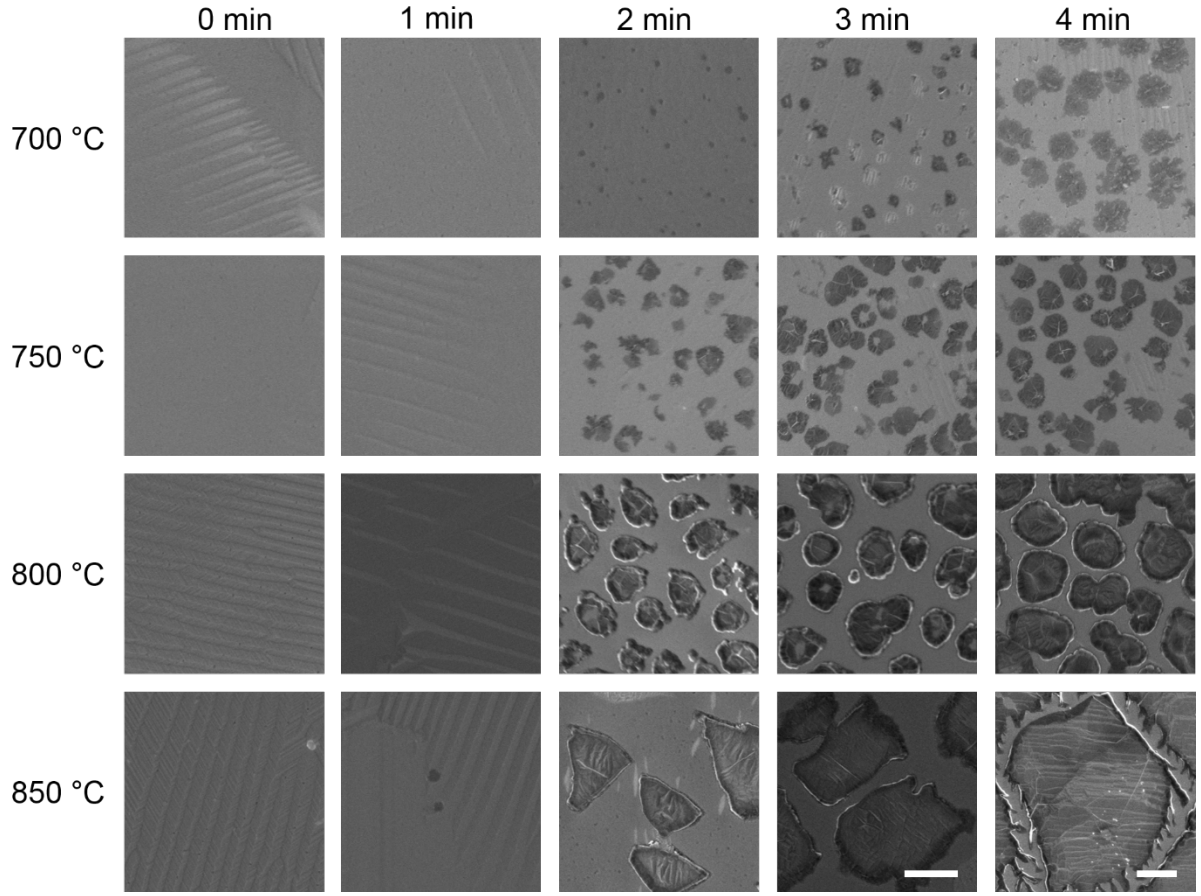

Figure 10. High-magnification SEM images of the flake of graphene on Cu catalyst for the calculation of flake area and growth rate depending on growth temperatures and times. Scale bar, 500nm.

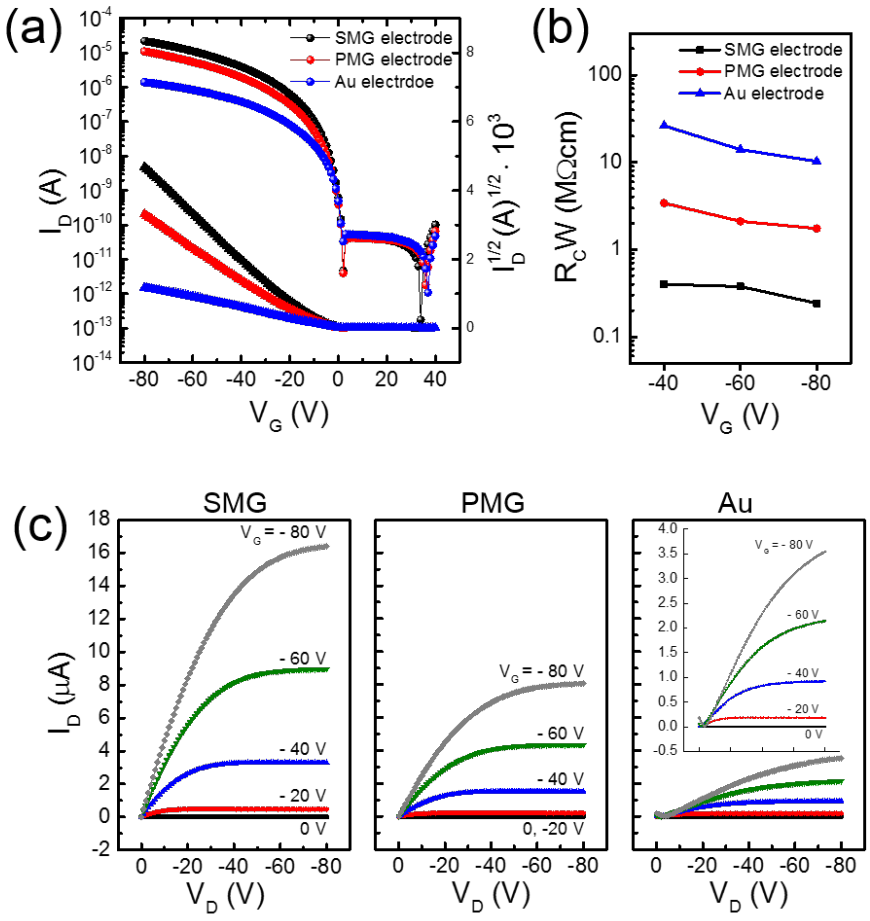

Figure 11. Electrical properties of pentacene FETs with various electrodes, such as SMG, photolithography monolayer graphene (PMG), and Au metal, on SiO_2/Si. (a) Transfer characteristics in the saturation regime (V_D = 80 V), and (c) output characteristics of OFETs prepared with the three types of electrodes. (b) Compared with calculation of the contact resistance values. All electrical measurements were performed in a N_2-rich glove box.

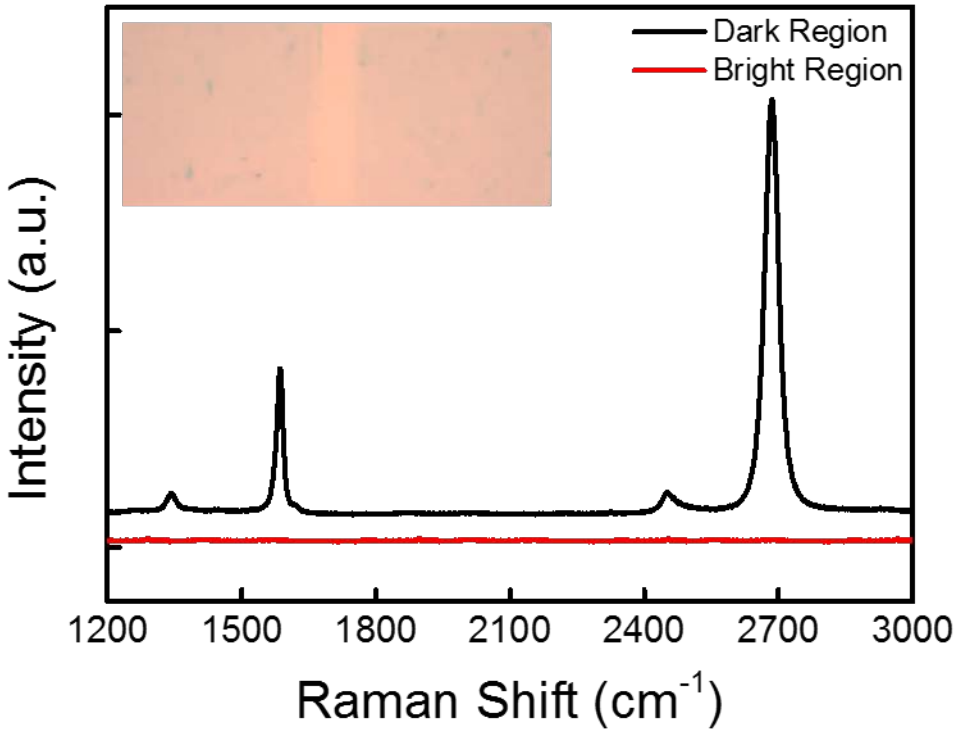

Figure 12. Raman spectra of SMG electrode. (inset) Optical image of SMG electrode.

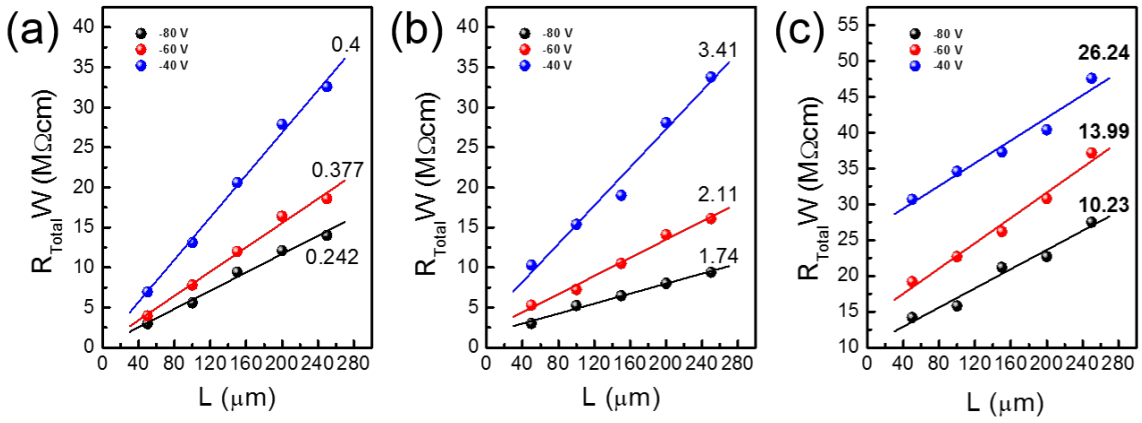

Figure 13. Channel width-normalized R_{total} of the pentacene FETs with (a) SMG electrodes, (b) PMG electrode, and (c) Au electrodes.

Chapter 3

The Synthesis of MoS_2 on Sapphire

Introduction

The most reported member of the transition metal dichalcogenides thin film, such as molybdenum disulfide (MoS_2), has attracted widespread attention for a variety of next-generation electrical and optoelectronic device applications due to its unique properties. A decrease in film thickness to the ultimate limit of the atomic, sub-nanometer length scale, a difficult limit for traditional semiconductors like Si and GaAs, would bring wide benefits for applications in ultrathin and flexible electronics.[1,2] In the bulk of TMDs, this material has a crystalline structure consisting of covalently bonded layers weakly coupled to each other by weak van der Waals (vdW) forces. Because of the weak coupling, monolayer MoS_2 can be easily obtained by exfoliation using Scotch tape[3] or liquid-phase exfoliation.[4] Whereas bulk MoS_2 is a semiconductor with an indirect band gap of 1.2 eV,[5] monolayer MoS_2 is a direct band gap semiconductor with a gap of at least 1.8 eV[6,7] due to the quantum confinement.[8] In addition, their unique electronic band structures provide novel ways of enhancing the functionalities of such devices, including the large excitonic effect,[9] bandgap modulation,[10] piezoelectricity,[11] and valleytronics.[12]

However, the large-scale growth of monolayer TMD films with spatial homogeneity and high electrical performance remains an unsolved challenge. Because of this, several methods, such as decomposition of thiomolybdates[13] and sulfurization of Mo metal[14] or molybdenum oxide,[15,16] have been exploited to synthesize MoS2 on diverse substrates. Among them, chemical vapor deposition (CVD) is the most promising method to synthesize monolayer MoS2 triangular islands tens of micrometers in size. In most of these reports, SiO2 was used as the growth substrate, resulting in the random orientation of MoS2 domains because of the amorphous nature of the substrate and its relatively high surface roughness. This inevitably

results in a large concentration of grain boundaries that can be detrimental to the electrical[17,18] and mechanical properties of the grown films over length scales exceeding several micrometers. In order to avoid this, it is necessary to control the crystallographic orientation of MoS2 islands during growth so that they can coalesce into a uniform layer with a reduced density of grain boundaries.

Recently, van der Waals epitaxy has shown its potential for circumventing the need for a lattice-matched substrate and still keeping an ordered relation with the substrate.[19] Van der Waals interaction between the substrate surface and the grown material governs the formation of the initial nuclei (islands), which constitute the precursors of the layers. Only energetically stable nuclei are able to grow by lateral spreading through the lateral facets. This leads to an overall preferential orientation of the grown layers. The relatively low strength of the van der Waals interaction and the relaxed requirement for lattice matching for substrates and overlayers without dangling bonds make it difficult in practice to control the lattice orientation of the deposited films. This was the case in previously reported deposition of centimeter-scale monolayer MoS2 films that have been deposited on other layered materials such as mica[20] or graphene,[21,22] where MoS2 grains showed a wide distribution of orientations with respect to each other and the substrate lattice.

Experimental

Growth Procedure. Monolayer MoS2 has been grown by metal organic chemical vapor deposition on c-plane sapphire. After consecutive cleaning by acetone/2-propanol/DI-water, the substrates were annealed for 1 h at 800 C in air. Molybdenum hexacarbonyl are selected as chemical precursors for Mo. The safety ratings for these precursors require them to be handled inside of a fume hood. C-plane sapphire was heated at 750 °C for 1 hour under 150 sccm Ar flow and 5 sccm H2 flow, and then both of 10 sccm H_2S and Mo precursor were inserted to permit MoS_2 growth over 10 hours. We use a total pressure of 2.5 Torr. Finally, the furnace was rapidly cooled to room temperature under Ar and H_2 flow.

Optical measurements. The surfaces of the graphene were imaged using an optical microscope (DSX-500, OLYMPUS) and a field-emission scanning electron microscope (AURIGA, Carl Zeiss). The Raman spectra were measured by a Raman spectrometer (RM 1000-Invia, Renishaw, 514nm). The AFM images were collected in the noncontact mode using a Park System XE-100 atomic force microscope. The photoluminescence (PL) measurements were performed with a 488 nm excitation laser under ambient conditions. The PL spectra from the sample were collected by an imaging spectrometer with a CCD camera, and the PL images were taken directly using band pass filters with the center wavelength corresponding to 1.9 eV for MoS_2.

Results and Discussion

We use c-plane sapphire substrates to achieve control over lattice orientation during MOCVD growth of monolayer MoS_2. Even though MoS_2 and sapphire interact only via the relatively weak van der Waals interaction, commensurability of the sapphire lattice with MoS_2 allows the van der Waals interaction to control the lattice orientation of MoS_2. Such the MoS_2 growth by the van der Waals interaction is called van der Waals epitaxy. It is expected that good heterostructures can be grown even between materials having large lattice mismatch with van der Waals epitaxy. In addition, van der Waals epitaxy is expected that a very abrupt interface with small amounts of defect can be fabricated because of the nonexistence of dangling bonds. Thus, van der Waals epitaxy seems to be one of the most powerful techniques for preparing good quality heterostructures with atomic-order thickness.

Figure 1a shows our resulting MoS_2 monolayer and the color photos of MoS_2 (green yellow) grown on a transparent sapphire substrate shows that the TMD grown region (right) is uniform over the whole substrate and clearly distinguishable from the bare sapphire substrate (left). Figure 1b presents SEM image of MoS_2 flake grown on sapphire. Although MoS_2 flakes have a variety of shapes such as triangle- and triangular star-shaped, the size of flake grown at 850 ºC is larger than that of flake grown at 750 ºC (as shown in Fig 2). We were then imaged by AFM. For identifying the thickness of MoS_2 flake, we observed step heights of individual layers of 0.7-0.8 nm. This value is compatible with the 0.62 nm interlayer spacing of a single layer of the S-Mo-S building block of the MoS_2 crystal. In the AFM measurement, monolayer flake on the bare sapphire showed a wider distribution in heights (0.6-0.9 nm). This may reflect the presence of adsorbates below the flake or other interactions between the flake and oxide substrate surface.[23]

Figure 3 shows representative Raman spectra for monolayer MoS_2 flake. Among the four

Raman-active modes of the bulk 2H-MoS_2 crystal (Figure 3c),[24] we observed the E^1_{2g} and A_{1g} modes near 400 cm^{-1}. The other two modes (E_{1g} and E^2_{2g}) could not be detected either because of selection rules for our scattering geometry (E_{1g})[24] or because of the limited rejection of the Rayleigh scattered radiation (E^2_{2g}).[25] Monolayer MoS_2 exhibits a strong in-plane vibrational mode at ~385 cm^{-1}, corresponding to the E^1_{2g} mode of the bulk 2H-MoS_2 crystal. In contrast, this mode was not observed in earlier studies of monolayer MoS_2 suspensions prepared from Li-intercalated MoS_2.[26] Its absence was attributed to the existence of metastable octahedral coordination, which renders the vibration Raman-inactive (E_u). Figure 3a indicates that our resulting monolayer MoS_2 maintain the trigonal prismatic coordination of bulk MoS_2.

Recently reported, the behavior of Raman spectra as a function of film thickness has several intriguing characteristics. Most strikingly, the E^1_{2g} vibration softens (red shifts), while the A_{1g} vibration stiffens (blue shifts) with increasing thickness. The vibrations of bulk materials built up from van der Waals-bonded layers are often analyzed in terms of the two-dimensional layers. Many approaches have been developed within this weak coupling limit to describe the relation between the vibrational modes within thin layers and the those of bulk material.[24,27] Within a classical model for coupled harmonic oscillators, the E^1_{2g} and A_{1g} modes are expected to stiffen as additional layers are added to form the bulk material form individual layers because the interlayer van der Waals interactions increase the effective restoring forces acting on the atoms.

While the shift of A_{1g} mode observed in our measurements with increasing layer number agrees with this prediction, the behavior of the E^1_{2g} mode does not. The failure of the model could reflect the presence of additional interlayer interactions; it could also indicate that the implicit assumption that stacking does not affect intralayer bonding is incorrect. Regarding the

latter, a low-energy electron diffraction study of MoS2 single crystals[28] showed that the interplane distance between Mo and S atomic planes within the topmost layer shrinks by ~5% compared to its bulk value. The lateral lattice expansion observed for dispersed single layers may also be related to surface reconstruction. In addition, the A1g mode of the topmost layer of bulk MoS2 crystals[29] was found to soften by 25 cm^{-1}, possibly because of the surface reconstruction. The observed surface reconstruction and vibrational softening show that even the nominally weak interlayer interaction in MoS2 can affect intralayer bonding and lattice dynamics. The same considerations may apply to single- and few-layer MoS2 samples.

The shift in the frequency of the A1g mode as a function of thickness in the current study is consistent with the transition from surface to bulk layers. The opposite progression for the E1 2g mode may reflect the influence of stacking-induced structural changes. Alternatively, the anomalous behavior of E1 2g may be attributed to long-range Coulombic interlayer interactions.

The successful formation of MoS_2 in atomic layers was initially characterized by Raman spectroscopy. Figure 3a shows that a representative Raman spectra of MoS_2 flake shows two characteristic peaks of E^1_{2g} and A_{1g} at 385.4 and 404.7 cm^{-1}, respectively. The Raman spectra taken at ten different locations in MoS_2 flake on sapphire. The energy difference of ~20 cm^{-1} between E^1_{2g} and A_{1g} peaks suggest that monolayer MoS_2 is more dominant than bilayer MoS_2 (Figure 3b). This result closely corresponds to the AFM image (Figure1c).

Figure 4a shows a photoluminescence spectrum acquired at room temperature on MOCVD-grown monolayer MoS_2. We can clearly resole the intense A excitonic peak at 1.86 eV, while the B exciton is not expected to be visible at low excitation intensities due to state-filling effects. Typical peak widths are ~61 meV and smaller than in exfoliated MoS_2 (~111

meV), indicating that our resulting MoS_2 has superior optical qualities to the exfoliated material. In addition, figure 4b indicates almost MoS_2 flakes are monolayer on sapphire.

Conclusion

In conclusion, we have demonstrated metal organic chemical vapor deposition growth of monolayer MoS_2 on sapphire by the use of liquid phase Mo-precursor. The AFM and SEM images revealed that the MoS_2 flake is well-defined triangular shape and MoS_2 flake has observed step heights of individual layers of 0.7-0.8 nm, which is compatible with the 0.62 nm interlayer spacing of a single layer of the S-Mo-S building block of the MoS_2 crystal. Furthermore, Raman and PL spectrum indicate that monolayer MoS_2 is less doped and smaller structural disorder. We believe that our versatile MOCVD leads to synthesis high quality monolayer MoS_2, allowing its use in future electronic and optoelectronic devices.

References

1. Rogers, J. A.; Someya, T.; Huang, Y., Materials and Mechanics for Stretchable Electronics. *Science* **2010,** *327*, 1603-1607.
2. Ko, H.; Takei, K.; Kapadia, R.; Chuang, S.; Fang, H.; Leu, P. W.; Ganapathi, K.; Plis, E.; Kim, H. S.; Chen, S.-Y.; Madsen, M.; Ford, A. C.; Chueh, Y.-L.; Krishna, S.; Salahuddin, S.; Javey, A., Ultrathin compound semiconductor on insulator layers for high-performance nanoscale transistors. *Nature* **2010,** *468*, 286-289.
3. Novoselov, K. S.; Jiang, D.; Schedin, F.; Booth, T. J.; Khotkevich, V. V.; Morozov, S. V.; Geim, A. K., Two-dimensional atomic crystals. *Proc. Natl. Acad. Sci. U.S.A.* **2005,** *102*, 10451-10453.
4. Coleman, J. N.; Lotya, M.; O'Neill, A.; Bergin, S. D.; King, P. J.; Khan, U.; Young, K.; Gaucher, A.; De, S.; Smith, R. J.; *et al* Two-Dimensional Nanosheets Produced by Liquid Exfoliation of Layered Materials. *Science* **2011,** *331*, 568-571.
5. Kam, K. K.; Parkinson, B. A., Detailed photocurrent spectroscopy of the semiconducting group VIB transition metal dichalcogenides. *J. Phys. Chem.* **1982,** *86*, 463-467.
6. Lebègue, S.; Eriksson, O., Electronic structure of two-dimensional crystals from *ab initio* theory. *Phys. Rev. B* **2009,** *79*, 115409.
7. Splendiani, A.; Sun, L.; Zhang, Y.; Li, T.; Kim, J.; Chim, C.-Y.; Galli, G.; Wang, F., Emerging Photoluminescence in Monolayer MoS2. *Nano Lett.* **2010,** *10*, 1271-1275.
8. Kuc, A.; Zibouche, N.; Heine, T., Influence of quantum confinement on the electronic structure of the transition metal sulfide TS_2. *Phys. Rev. B* **2011,** *83*, 245213.
9. Ye, Z.; Cao, T.; O/'Brien, K.; Zhu, H.; Yin, X.; Wang, Y.; Louie, S. G.; Zhang, X., Probing excitonic dark states in single-layer tungsten disulphide. *Nature* **2014,** *513*,

214-218.

10. Feng, Q.; Zhu, Y.; Hong, J.; Zhang, M.; Duan, W.; Mao, N.; Wu, J.; Xu, H.; Dong, F.; Lin, F.; Jin, C.; Wang, C.; Zhang, J.; Xie, L., Growth of Large-Area 2D $MoS_{2(1-x)}Se_{2x}$ Semiconductor Alloys. *Adv. Mater.* **2014,** *26*, 2648-2653.
11. Wu, W.; Wang, L.; Li, Y.; Zhang, F.; Lin, L.; Niu, S.; Chenet, D.; Zhang, X.; Hao, Y.; Heinz, T. F.; Hone, J.; Wang, Z. L., Piezoelectricity of single-atomic-layer MoS2 for energy conversion and piezotronics. *Nature* **2014,** *514*, 470-474.
12. Mak, K. F.; McGill, K. L.; Park, J.; McEuen, P. L., The valley Hall effect in MoS2 transistors. *Science* **2014,** *344*, 1489-1492.
13. Liu, K.-K.; Zhang, W.; Lee, Y.-H.; Lin, Y.-C.; Chang, M.-T.; Su, C.-Y.; Chang, C.-S.; Li, H.; Shi, Y.; Zhang, H.; Lai, C.-S.; Li, L.-J., Growth of Large-Area and Highly Crystalline MoS2 Thin Layers on Insulating Substrates. *Nano Lett.* **2012,** *12*, 1538-1544.
14. Zhan, Y.; Liu, Z.; Najmaei, S.; Ajayan, P. M.; Lou, J., Large-Area Vapor-Phase Growth and Characterization of MoS2 Atomic Layers on a SiO2 Substrate. *Small* **2012,** *8*, 966-971.
15. Najmaei, S.; Liu, Z.; Zhou, W.; Zou, X.; Shi, G.; Lei, S.; Yakobson, B. I.; Idrobo, J.-C.; Ajayan, P. M.; Lou, J., Vapour phase growth and grain boundary structure of molybdenum disulphide atomic layers. *Nat. Mater.* **2013,** *12*, 754-759.
16. van der Zande, A. M.; Huang, P. Y.; Chenet, D. A.; Berkelbach, T. C.; You, Y.; Lee, G.-H.; Heinz, T. F.; Reichman, D. R.; Muller, D. A.; Hone, J. C., Grains and grain boundaries in highly crystalline monolayer molybdenum disulphide. *Nat. Mater.* **2013,** *12*, 554-561.
17. Najmaei, S.; Amani, M.; Chin, M. L.; Liu, Z.; Birdwell, A. G.; O'Regan, T. P.; Ajayan,

P. M.; Dubey, M.; Lou, J., Electrical Transport Properties of Polycrystalline Monolayer Molybdenum Disulfide. *ACS Nano* **2014,** *8*, 7930-7937.

18. Yazyev, O. V.; Chen, Y. P., Polycrystalline graphene and other two-dimensional materials. *Nat. Nanotechnol.* **2014,** *9*, 755-767.

19. Koma, A., Van der Waals epitaxy for highly lattice-mismatched systems. *J. Cryst. Growth* **1999,** *201–202*, 236-241.

20. Ji, Q.; Zhang, Y.; Gao, T.; Zhang, Y.; Ma, D.; Liu, M.; Chen, Y.; Qiao, X.; Tan, P.-H.; Kan, M.; Feng, J.; Sun, Q.; Liu, Z., Epitaxial Monolayer MoS_2 on Mica with Novel Photoluminescence. *Nano Lett.* **2013,** *13*, 3870-3877.

21. Shi, Y.; Zhou, W.; Lu, A.-Y.; Fang, W.; Lee, Y.-H.; Hsu, A. L.; Kim, S. M.; Kim, K. K.; Yang, H. Y.; Li, L.-J.; Idrobo, J.-C.; Kong, J., van der Waals Epitaxy of MoS_2 Layers Using Graphene As Growth Templates. *Nano Lett.* **2012,** *12*, 2784-2791.

22. Lin, Y.-C.; Lu, N.; Perea-Lopez, N.; Li, J.; Lin, Z.; Peng, X.; Lee, C. H.; Sun, C.; Calderin, L.; Browning, P. N.; Bresnehan, M. S.; Kim, M. J.; Mayer, T. S.; Terrones, M.; Robinson, J. A., Direct Synthesis of van der Waals Solids. *ACS Nano* **2014,** *8*, 3715-3723.

23. Nemes-Incze, P.; Osváth, Z.; Kamarás, K.; Biró, L. P., Anomalies in thickness measurements of graphene and few layer graphite crystals by tapping mode atomic force microscopy. *Carbon* **2008,** *46*, 1435-1442.

24. Verble, J. L.; Wieting, T. J., Lattice Mode Degeneracy in MoS_2 and Other Layer Compounds. *Phys. Rev. Lett.* **1970,** *25*, 362-365.

25. Verble, J. L.; Wietling, T. J.; Reed, P. R., Rigid-layer lattice vibrations and van der waals bonding in hexagonal MoS2. *Solid State Commun.* **1972,** *11*, 941-944.

26. Yang, D.; Sandoval, S. J.; Divigalpitiya, W. M. R.; Irwin, J. C.; Frindt, R. F., Structure

of single-molecular-layer MoS_2. *Phys. Rev. B* **1991,** *43*, 12053-12056.

27. Bromley, R. A., The lattice vibrations of the MoS_2 structure. *Philos. Mag.* **1971,** *23*, 1417-1427.

28. Mrstik, B. J.; Kaplan, R.; Reinecke, T. L.; Van Hove, M.; Tong, S. Y., Surface-structure determination of the layered compounds MoS_2 and $NbSe_2$ by low-energy electron diffraction. *Phys. Rev. B* **1977,** *15*, 897-900.

29. Bertrand, P. A., Surface-phonon dispersion of MoS_2. *Phys. Rev. B* **1991,** *44*, 5745-5749.

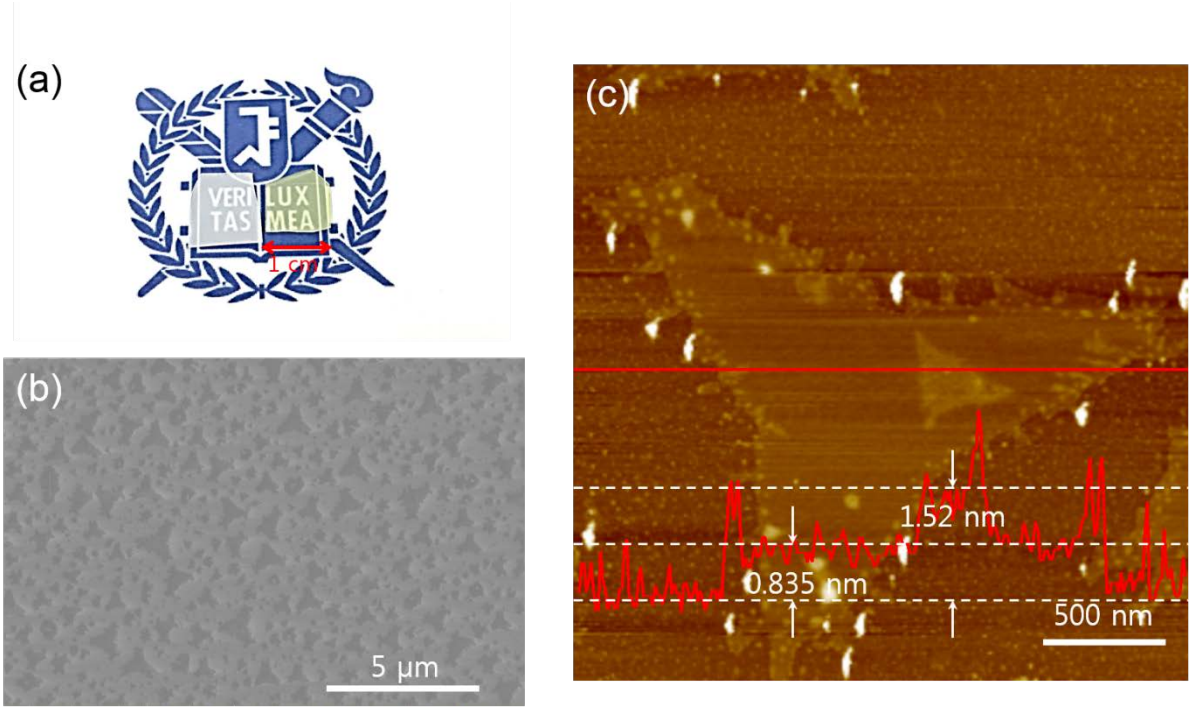

Figure 1. (a) Photographs of monolayer MoS_2 grown on sapphire (right). The left substrate shows the bare sapphire for comparison. (b) SEM image of monolayer MoS_2 flake on sapphire. (c) AFM image of monolayer MoS_2 flake. Inset: Line scan showing the thickness profile along the red line in the AFM image.

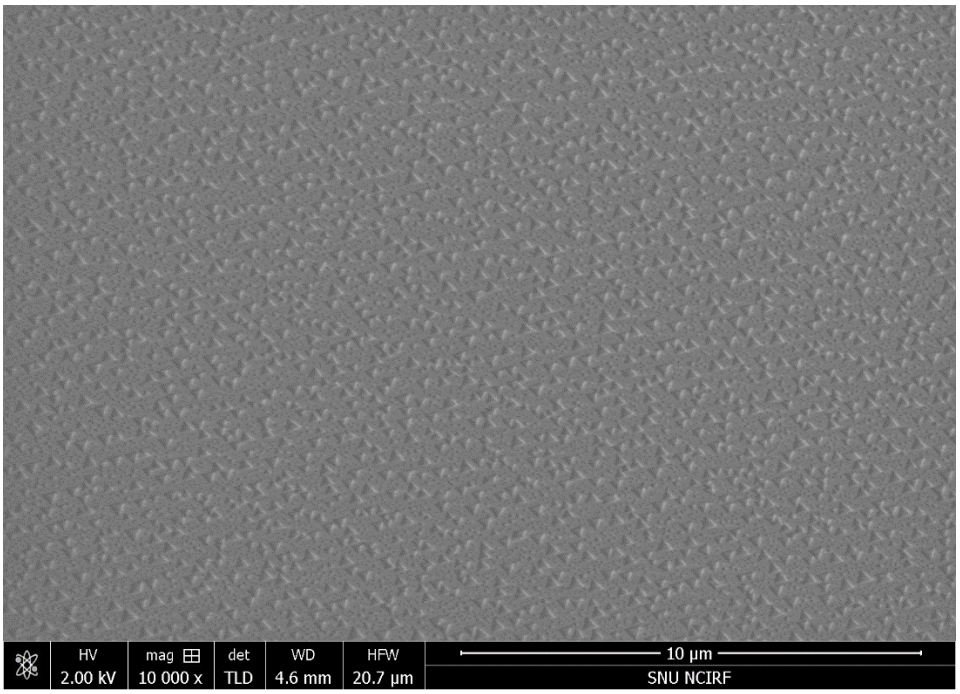

Figure 2. SEM images of monolayer MoS_2 flake grown at 750 ºC.

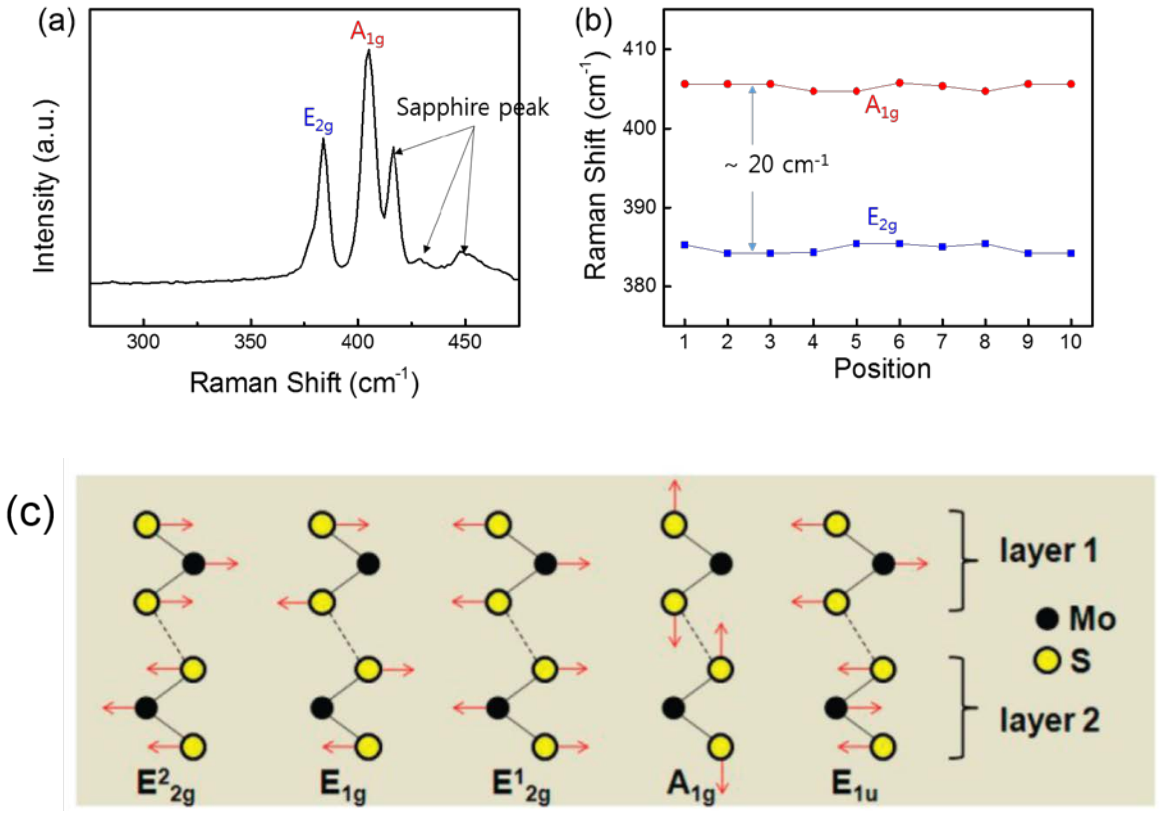

Figure 3. (a) Representative Raman spectrum of MoS_2 flake. (b) Positions of Raman peaks measured at ten random positions. (c) Atomic displacements of the sour Raman-active modes and one IR-active mode (E_{1u}) in the unit cell of the bulk MoS_2 crystal as viewed along the [1000] direction.[30]

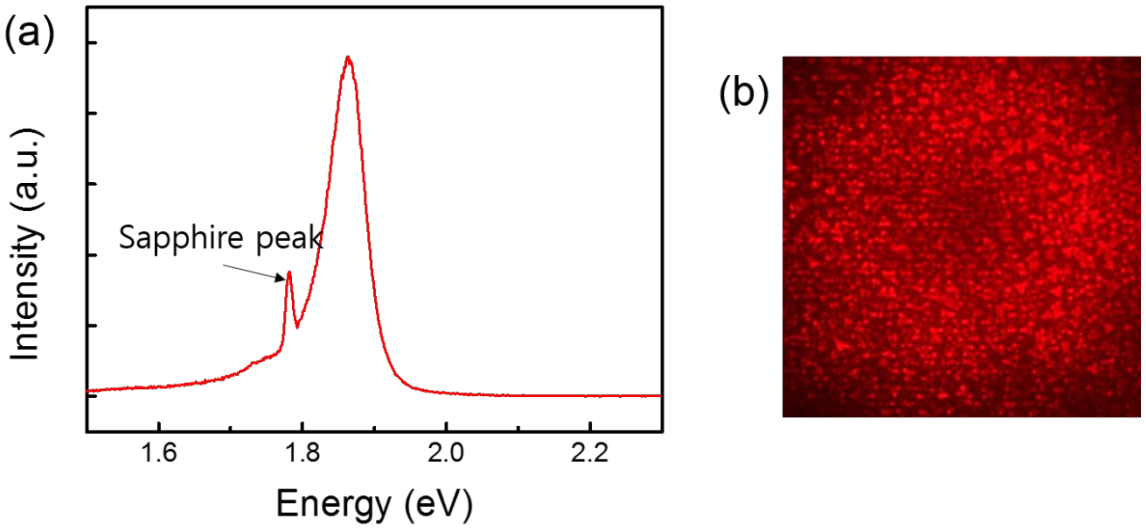

Figure 4. (a) PL spectrum of monolayer MoS_2 flake grown on sapphire. (b) PL image of monolayer MoS_2 flake grown on sapphire.

Chapter 4

Graphene Gas Barrier Films[3]

[3] K. Choi, S. Nam et al. Reduced Water Vapor Transmission Rate of Graphene Gas Barrier Films for Flexible Organic Field-Effect Transistors, *ACS Nano,* (2015)

Introduction

Graphene, an atomically thin two-dimensional carbon allotrope with hexagonal lattice structures, has been intensively studied in recent years owing to its outstanding electrical,[1-3] mechanical,[4,5] and chemical properties.[6,7] In particular, graphene has received much attention as a promising barrier material not only because of its densely packed structure that does not allow the transmission of gases or liquids[8-17] but because of outstanding optical transparency and mechanical flexibility. This is particularly important for flexible OFETs,[18-21] as the performance of organic materials considerably degrades in the presence of water or oxygen molecules from ambient air.[22-24] Inorganic materials such as silicone oxides (SiOx) and aluminum oxides (Al_2O_3) have been predominantly employed as the gas barrier films.[25-27] However, the complicated fabrication processes as well as the poor mechanical flexibility of these materials have hindered the practical application to flexible electronic devices.[28,29] In this regard, the excellent gas-impermeability, flexibility, and transmittance of graphene films[30] are expected to be useful for more reliable and durable operation of organic devices. Recently, Lange *et al.* have discovered the impermeable characteristics of mechanically exfoliated graphene,[31] and Liu *et al*. have successfully demonstrated the application of large-area graphene films to gas-impermeable top electrodes covering organic photovoltaic devices.[11] However, the impermeability of large-area graphene has not been directly evidenced by measuring the WVTR, although it is a standard parameter showing the performance of gas-impermeability.

Here, we directly evaluated the gas barrier performance of large-area graphene films (10x10 cm^2) synthesized by CVD by measuring the WVTR. The WVTR value of 6-layer graphene on PET films was as low as 10^{-4} $g/m^2 \cdot day$ for the first a few hours. However, it was gradually increased and stabilized at 0.48 $g/m^2 day$, which is 7 times lower than bare PET films.

The graphene-passivated OFETs exhibit excellent environmental stability as well as a prolonged lifetime compared to the non-passivated devices even after 500 bending cycles with strain of 2.3 %.

Experimental

Sample preparation. Monolayer graphene was grown on a Cu foil in a quartz tube using CVD methods. The Cu foil was heated at 1000 °C for 1 hour under a 5 sccm H_2 flow, and then 35 sccm CH_4 was inserted to permit graphene growth over 30 min. Finally, the furnace was rapidly cooled to room temperature under a H_2 flow. To protect the graphene, the PMMA solution was applied onto the graphene/Cu foil using a spin-coater. The Cu foil was etched away using 0.05 M ammonium persulfate over 7 hours. The floating graphene layer and the PMMA support film were transferred onto the target substrate.

Devices fabrication. A 50-nm-thick Al layer was deposited onto a PAR substrate to form a gate electrode. Subsequently, a 100-nm-thick Al_2O_3 layer was coated as a gate insulator using a plasma enhanced atomic layer deposition (PEALD) process. During the PEALD process, trimethylaluminum (TMA) and oxygen (O_2) gases were used as the sources of Al and O, respectively. The PEALD process is described in detail elsewhere.[40] A 30 nm layer of a cyclic olefin copolymer (Polyscience Co.) was spin-coated to provide a bilayer gate dielectric layer. The samples were then heated on a 120 °C hot plate for 30 min to remove residual solvent. Subsequently, a 50-nm-thick pentacene film was deposited onto the dielectric layer by means of organic molecular beam deposition under high vacuum (i.e., 10^{-7} Torr) at a rate of 0.2 Å/s through a shadow mask. The top-contact geometry was prepared by thermally evaporating gold source/drain electrodes through a shadow mask onto the pentacene layer (5 Å/s under 10^{-6} Torr). The channel length (L) and width (W) of the shadow mask used for the gold deposition step were fixed at 100 μm and 1500 μm, respectively.

Characterization. The transmittances of graphene were measured using a SINCO S-3100. The surfaces of the graphene were imaged using a field-emission scanning electron microscope

(AURIGA, Carl Zeiss). The AFM images were collected in the noncontact mode using a Park System XE-100 atomic force microscope. The C1s core level bands of graphene were acquired using an Axis-HIS (Kratos Inc.). Water vapor transmission rate (WVTR) testing was performed in accordance with the ASTM F1249, using a PERMATRAN_W 3/33 MA (MOCON) at room temperature and 100% RH. (Film type of barrier materials is placed in test cell, which is made up inside chamber and outside chamber and separated by test sample. The inside chamber is filled with nitrogen (carrier gas) and the outside chamber is filled with water vapor (test gas). Molecules of water diffuse through the test film to the inside chamber and are conveyed to the sensor by the carrier gas. The computer monitors the increase in water vapor concentration in the carrier gas and it reports that value on the screen as the water vapor transmission rate.) The electrical characteristics of the pentacene FETs were measured using Keithley 2400 and 236 source/measure units. The capacitances were characterized using a 4284A LCR meter (Agilent Tech).

Results and Discussion

We synthesized large-area graphene using a typical CVD method using 35-μm-thick Cu foils with flowing 35 sccm methane and 5 sccm hydrogen gases at 1000 °C,[3] followed by coating with poly(methyl-methacrylate) (PMMA) and transfer to PET films. After the removal of PMMA with acetone, considerable amount of PMMA residues remains on graphene surface, which disturbs the close contact between multi-transferred graphene layers. Therefore, the PMMA-assisted transfer steps need to be minimized for less polymer residues and for better performance of graphene gas barrier films. Figure 1 shows the difference between a single PMMA coating/removal step (upper) and multiple PMMA coating/removal steps (lower). In the case of conventional transfer processes that includes multiple PMMA coating/removal steps, PMMA/graphene is transferred onto target substrate such as PET, and then PMMA is removed in acetone. Thus, repetition of PMMA coating/removal steps multiple times is needed for obtaining multiple stacked graphene. However, in case of single PMMA coating/removal step, PMMA/graphene is directly transferred onto graphene/Cu foil (G/Cu). After etching Cu foil and transferring on G/Cu several times, multiple stacked graphene can be obtained without polymer residue, with only single PMMA removal step. Thus, we used a graphene transfer method that requires only one time use of the PMMA layer as shown in Figure 1.[32]

In the multiple PMMA coating/removal steps, the greater amount of polymer residues remained on graphene compared to the case of using a single PMMA coating/removal step, as evidenced by atomic force microscopy (AFM) and scanning electron microscopy (SEM) images (Figure 2a-d). As a result, the WVTR of the single-PMMA-coated graphene films decreased from 2.22 $g/m^2 \cdot day$ to 0.94 $g/m^2 \cdot day$, indicating that minimizing the gap between graphene layers efficiently blocks the penetrating passage of water and oxygen molecules. It should be noted that the graphene barrier films initially showed WVTR as low as 10^{-4}

g/m^2·day, but the WVTR value gradually increased with time possibly due to the horizontal diffusion of water molecules between the graphene layers (Figure 3). All the WVTR values in the manuscript were measured after the WVTR change has been stabilized and saturated.

The WVTR of monolayer graphene on a PET film (3.11 g/m^2·day) does not much differ from that of a bare PET film (3.28 g/m^2·day) because of defects or tears formed during growth and transfer steps (Figure 4a, b). However, the WVTR considerably decreased by adding another layer of graphene on top (Figure 2f), as the additional layer can patch the defects on the previous graphene layer (Figure 4c). The WVTR of the 6-layer graphene film prepared on a PET substrate was measured to be of 0.48 g/m^2·day, which is 7-fold lower than that of a bare PET film. It should be noted that the 6-layer graphene exhibits an excellent optical transmittance as high as 85% at a wavelength of 550 nm (Figure 5), which is of great importance for the barrier application to various optoelectronic applications.

As mentioned earlier, graphene can act as anti-oxidation layer because of its densely packed structure that does not allow the transmission of gases or liquids. We carried out other research on a long-term corrosion protection. As-grown graphene on Cu surface exposed to ambient conditions showed no significant change for more than 2 months, while the bare Cu surface is readily oxidized (Figure 6).[33] XPS spectra of Cu foil with graphene indicates two sharp peaks related Cu ($Cu2p_{3/2}$: 932.6 eV and $Cu2p_{1/2}$: 952.4 eV) whereas that of bare Cu foil shows the broad peaks corresponding to copper oxide (Cu_2O: 932.4 and 952.4 eV, CuO: 933.6 and 953.4 eV, $Cu(OH)_2$: 934.3 and 954.5 eV). Therefore, these results suggest that graphene films can defend metals against environment oxidants.

To meet the demands of the growing interest in flexible electronics, organic semiconductors have been intensively studied as emerging materials due to high field-effect mobility and outstanding on-off ratio. Among them, pentacene is a widely used p-type organic

semiconductor,[34,35] however, its electrical properties, morphology, and chemical states are significantly degraded in the presence of water or oxygen species from ambient air.[36,37] Thus, we investigated the barrier effects of our multi-stacked graphene by the use of practical pentacene-FET devices on flexible substrates.[20] Stability tests under harsh oxygen-rich conditions were conducted by applying UV/Ozone treatment (λ = 254 nm) to the pentacene films. The AFM image shows the typical three-dimensional pyramidal structure of a bare pentacene film on a SiO_2 substrate (Figure 7a). As the UV/Ozone treatment proceeds, the continuous pentacene film changed to spherical particles and then gradually disappeared (Figure 8).

The AFM images, line profiles, and XPS spectra of a pentacene film on a SiO_2/Si substrate in Figure 5 clearly show the difference between UV/Ozone-treated pentacene films with and without protecting graphene films. The morphology of the pentacene without protecting graphene became very rough after oxidation. The XPS spectra also indicate that the pentacene unprotected by graphene easily oxidizes while the graphene barrier layer prevents the pentacene from oxidation that leads to the degradation of its semiconducting property. We suppose that a new peak arising at 289 eV (O=C-O), including two conspicuous peaks of bare pentacene films: one strong peak centered at 284.5 eV (C=C) and a sub-band centered at 285.7 eV (C-C), in Figure 7b are resulted from PMMA residues on top of the protecting graphene layer and the appearance of the oxygen-containing groups on the graphene surface, thus the underlying pentacene is still safe from the harsh oxidation condition (AFM image in Figure 5b). As shown in Figure 7c, the new peaks corresponding to C-C, O=C-O, and 287.6 eV (C=O) groups reveal that the pentacene film without a graphene barrier has been heavily oxidized,[22] which is also in good agreement with a previous report that showed the deformed surface

morphology of oxidized pentacene films after UV irradiation in presence of oxygen species (Figure 8).

The barrier robustness of the graphene films was further verified by applying these to OFETs. The field-effect mobilities of the OFETs were obtained from the slope of a plot of the square root of the drain current (I_D) *versus* the gate voltage (V_G) in the saturation current region using the following equation:

$$I_D = (\frac{WC_i}{2L})\mu(V_G - V_{th})^2,$$

where I_D is the drain current, C_i is the capacitance per unit area of the dielectric, and W and L are the channel width and length, respectively. In case of direct contact between graphene and pentacene, the pentacene of the channel region can be seriously damaged due to the over-flow of charges through graphene (Figure 10c). To avoid this problem induced by the conductivity of graphene barrier layers, the PMMA side of the PMMA/graphene film needs to be in contact with the pentacene layer, which can be accomplished by a reversed transfer method as depicted in Figure 9.[38] PMMA as a dielectric layer can block vertical overflow through the graphene layer.[39] We fabricated a device with a structure containing polyarylate (PAR)/Al/Al_2O_3/Au/pentacene /PMMA/graphene (a mobility of ~ 0.5 $cm^2 \cdot V^{-1} \cdot s^{-1}$ in Figure 10a). Figure 11 shows the characteristics of OFET as time passed and bending stability, respectively. The devices were kept in a 60°C and 60% relative humidity conditioned chamber. The $I_D^{1/2}$ *versus* V_G and relative mobility of graphene-passivated OFETs changed much less than the unpassivated OFETs with the elapse of time (Figure 11a, b).

We also evaluated the stability of the graphene passivation layer by monitoring the OFET performance with respect to cyclic bending at ~ 2.3 % strain, resulting in only ~30% degradation in mobility (from 0.51 ± 0.04 $cm^2 \cdot V^{-1} \cdot s^{-1}$ to 0.35 ± 0.09 $cm^2 \cdot V^{-1} \cdot s^{-}1$) but considerable enhancement in on/off ratios (Figure 11c, d). This result well matches with the stable WVTR values of bended graphene/PET films (Figure 12). The WVTR of the PET after 500-cycle bending test increased by a factor of 10 compared to PET prior to bending, whereas the barrier properties of graphene/PET films were gradually stabilized with bending cycles. We suppose that the poor off-current problem in graphene-passivated OFETs can be removed if wrinkles and voids that are unfavorable for the dielectric property of PMMA/graphene layers disappear with cyclic bending. We further infer that graphene is a very effective barrier film regardless of the number of bending.

Conclusion

In summary, we have successfully measured the WVTR of large-area graphene films grown by CVD, which is as low as 0.48 g/m^2·day corresponding to a 7-fold improvement compared to a bare PET film. The AFM images and XPS spectra revealed that the graphene films efficiently protect a pentacene film from oxidizing species. We also showed that the flexible OFETs passivated with the graphene films exhibit prolonged lifetimes (~42 days) and mechanical stability over 500 bending cycles (~2.3 % strain). We believe that our results provide an important reference that supports the excellent gas barrier properties of large-area graphene films, but further optimization is needed to fully utilize the intrinsic gas-impermeable capability of graphene films.

References

1. Geim, A. K.; Novoselov, K. S., The Rise of Graphene. *Nat. Mater.* **2007**, *6*, 183-191.

2. Bolotin, K. I.; Sikes, K. J.; Jiang, Z.; Klima, M.; Fudenberg, G.; Hone, J.; Kim, P.; Stormer, H. L., Ultrahigh Electron Mobility in Suspended Graphene. *Solid State Commun.* **2008**, *146*, 351-355.

3. Bae, S.; Kim, H.; Lee, Y.; Xu, X.; Park, J.-S.; Zheng, Y.; Balakrishnan, J.; Lei, T.; Ri Kim, H.; Song, Y. I.; *et al.* Roll-to-roll Production of 30-inch Graphene Films for Transparent Electrodes. *Nat. Nanotechnol.* **2010**, *5*, 574-578.

4. Lee, C.; Wei, X.; Kysar, J. W.; Hone, J., Measurement of the Elastic Properties and Intrinsic Strength of Monolayer Graphene. *Science* **2008**, *321*, 385-388.

5. Koenig, S. P.; Boddeti, N. G.; Dunn, M. L.; Bunch, J. S., Ultrastrong Adhesion of Graphene Membranes. *Nat. Nanotechnol.* **2011**, *6*, 543-546.

6. McAllister, M. J.; Li, J.-L.; Adamson, D. H.; Schniepp, H. C.; Abdala, A. A.; Liu, J.; Herrera-Alonso, M.; Milius, D. L.; Car, R.; Prud'homme, R. K.; *et al.* Single Sheet Functionalized Graphene by Oxidation and Thermal Expansion of Graphite. *Chem. Mater.* **2007**, *19*, 4396-4404.

7. Wang, X.; Li, X.; Zhang, L.; Yoon, Y.; Weber, P. K.; Wang, H.; Guo, J.; Dai, H., N-Doping of Graphene Through Electrothermal Reactions with Ammonia. *Science* **2009**, *324*, 768-771.

8. Bunch, J. S.; Verbridge, S. S.; Alden, J. S.; van der Zande, A. M.; Parpia, J. M.; Craighead, H. G.; McEuen, P. L., Impermeable Atomic Membranes from Graphene Sheets. *Nano*

Lett. **2008**, *8*, 2458-2462.

9. Nair, R. R.; Wu, H. A.; Jayaram, P. N.; Grigorieva, I. V.; Geim, A. K., Unimpeded Permeation of Water Through Helium-Leak–Tight Graphene-Based Membranes. *Science* **2012**, *335*, 442-444.

10. Shin, D.; Park, J. B.; Kim, Y.-J.; Kim, S. J.; Kang, J. H.; Lee, B.; Cho, S.-P.; Hong, B. H.; Novoselov, K. S., Growth Dynamics and Gas Transport Mechanism of Nanobubbles in Graphene Liquid Cells. *Nat. Commun.* **2015**, 6.

11. Liu, Z.; Li, J.; Yan, F., Package-Free Flexible Organic Solar Cells with Graphene top Electrodes. *Adv. Mater.* **2013**, *25*, 4296-4301.

12. Zhao, Y.; Xie, Y.; Hui, Y. Y.; Tang, L.; Jie, W.; Jiang, Y.; Xu, L.; Lau, S. P.; Chai, Y., Highly Impermeable and Transparent Graphene as an Ultra-Thin Protection Barrier for Ag Thin Films. *J. Mater. Chem. C* **2013**, *1*, 4956-4961.

13. Su, Y.; Kravets, V. G.; Wong, S. L.; Waters, J.; Geim, A. K.; Nair, R. R., Impermeable Barrier Films and Protective Coatings based on Reduced Graphene Oxide. *Nat. Commun.* **2014**, 5.

14. Yamaguchi, H.; Granstrom, J.; Nie, W.; Sojoudi, H.; Fujita, T.; Voiry, D.; Chen, M.; Gupta, G.; Mohite, A. D.; Graham, S.; *et al.* Reduced Graphene Oxide Thin Films as Ultrabarriers for Organic Electronics. *Adv. Energy Mater.* **2014**, *4*, 1300986.

15. Celebi, K.; Buchheim, J.; Wyss, R. M.; Droudian, A.; Gasser, P.; Shorubalko, I.; Kye, J.-I.; Lee, C.; Park, H. G., Ultimate Permeation Across Atomically Thin Porous Graphene. *Science* **2014**, *344*, 289-292.

16. Boutilier, M. S. H.; Sun, C.; O'Hern, S. C.; Au, H.; Hadjiconstantinou, N. G.; Karnik, R., Implications of Permeation through Intrinsic Defects in Graphene on the Design of Defect-Tolerant Membranes for Gas Separation. *ACS Nano* **2014**, *8*, 841-849.

17. Yang, S.; Zhan, L.; Xu, X.; Wang, Y.; Ling, L.; Feng, X., Graphene-Based Porous Silica Sheets Impregnated with Polyethyleneimine for Superior CO2 Capture. *Adv. Mater.* **2013**, *25*, 2130-2134.

18. Lee, W. H.; Park, J.; Sim, S. H.; Lim, S.; Kim, K. S.; Hong, B. H.; Cho, K., Surface-Directed Molecular Assembly of Pentacene on Monolayer Graphene for High-Performance Organic Transistors. *J. Am. Chem. Soc.* **2011**, *133*, 4447-4454.

19. Ou, X.; Jiang, L.; Chen, P.; Zhu, M.; Hu, W.; Liu, M.; Zhu, J.; Ju, H., Highly Stable Graphene-Based Multilayer Films Immobilized *via* Covalent Bonds and Their Applications in Organic Field-Effect Transistors. *Adv. Funct. Mater.* **2013**, *23*, 2422-2435.

20. Nam, S.; Jang, J.; Kim, K.; Yun, W. M.; Chung, D. S.; Hwang, J.; Kwon, O. K.; Chang, T.; Park, C. E., Solvent-Free Solution Processed Passivation Layer for Improved Long-Term Stability of Organic Field-Effect Transistors. *J. Mater. Chem.* **2011**, *21*, 775-780.

21. Sekitani, T.; Zschieschang, U.; Klauk, H.; Someya, T., Flexible Organic Transistors and Circuits with Extreme Bending Stability. *Nat. Mater.* **2010**, *9*, 1015-1022.

22. Yang, H.; Yang, L.; Ling, M.-M.; Lastella, S.; Gandhi, D. D.; Ramanath, G.; Bao, Z.; Ryu, C. Y., Aging Susceptibility of Terrace-Like Pentacene Films. *J. Phys. Chem. C* **2008**, *112*, 16161-16165.

23. Schaer, M.; Nüesch, F.; Berner, D.; Leo, W.; Zuppiroli, L., Water Vapor and Oxygen Degradation Mechanisms in Organic Light Emitting Diodes. *Adv. Funct. Mater.* **2001**, *11*,

116-121.

24. Li, D.; Borkent, E.-J.; Nortrup, R.; Moon, H.; Katz, H.; Bao, Z., Humidity Effect on Electrical Performance of Organic Thin-Film Transistors. *Appl. Phys. Lett.* **2005**, *86*, 042105.

25. Jeon, H.; Shin, K.; Yang, C.; Park, C. E.; Park, S.-H. K., Thin-Film Passivation by Atomic Layer Deposition for Organic Field-Effect Transistors. *Appl. Phys. Lett.* **2008**, *93*, 163304.

26. Kim, N.; Potscavage, W. J.; Domercq, B.; Kippelen, B.; Graham, S., A hybrid Encapsulation Method for Organic Electronics. *Appl. Phys. Lett.* **2009**, *94*, 163308.

27. Meyer, J.; Görrn, P.; Bertram, F.; Hamwi, S.; Winkler, T.; Johannes, H.-H.; Weimann, T.; Hinze, P.; Riedl, T.; Kowalsky, W., Al2O3/ZrO2 Nanolaminates as Ultrahigh Gas-Diffusion Barriers—A Strategy for Reliable Encapsulation of Organic Electronics. *Adv. Mater.* **2009**, *21*, 1845-1849.

28. Jang, J.; Nam, S.; Chung, D. S.; Kim, S. H.; Yun, W. M.; Park, C. E., High Tg Cyclic Olefin Copolymer Gate Dielectrics for N,N′-Ditridecyl Perylene Diimide Based Field-Effect Transistors: Improving Performance and Stability with Thermal Treatment. *Adv. Funct. Mater.* **2010**, *20*, 2611-2618.

29. Singh, T. B.; Marjanović, N.; Matt, G. J.; Günes, S.; Sariciftci, N. S.; Montaigne Ramil, A.; Andreev, A.; Sitter, H.; Schwödiauer, R.; Bauer, S., High-Mobility n-Channel Organic Field-Effect Transistors based on Epitaxially Grown C60 Films. *Org. Electron.* **2005**, *6*, 105-110.

30. Kim, K. S.; Zhao, Y.; Jang, H.; Lee, S. Y.; Kim, J. M.; Kim, K. S.; Ahn, J.-H.; Kim, P.;

Choi, J.-Y.; Hong, B. H., Large-Scale Pattern Growth of Graphene Films for Stretchable Transparent Electrodes. *Nature* **2009**, *457*, 706-710.

31. Lange, P.; Dorn, M.; Severin, N.; Vanden Bout, D. A.; Rabe, J. P., Single- and Double-Layer Graphenes as Ultrabarriers for Fluorescent Polymer Films. *J. Phys. Chem. C* **2011**, *115*, 23057-23061.

32. Wang, Y.; Tong, S. W.; Xu, X. F.; Özyilmaz, B.; Loh, K. P., Interface Engineering of Layer-by-Layer Stacked Graphene Anodes for High-Performance Organic Solar Cells. *Adv. Mater.* **2011**, *23*, 1514-1518.

33. Chen, S.; Brown, L.; Levendorf, M.; Cai, W.; Ju, S.-Y.; Edgeworth, J.; Li, X.; Magnuson, C. W.; Velamakanni, A.; Piner, R. D.; *et al.* Oxidation Resistance of Graphene-Coated Cu and Cu/Ni Alloy. *ACS Nano* **2011**, *5*, 1321-1327.

34. Kato, Y.; Iba, S.; Teramoto, R.; Sekitani, T.; Someya, T.; Kawaguchi, H.; Sakurai, T., High Mobility of Pentacene Field-Effect Transistors with Polyimide Gate Dielectric Layers. *Appl. Phys. Lett.* **2004**, *84*, 3789-3791.

35. Meijer, E. J.; de Leeuw, D. M.; Setayesh, S.; van Veenendaal, E.; Huisman, B. H.; Blom, P. W. M.; Hummelen, J. C.; Scherf, U.; Klapwijk, T. M., Solution-Processed Ambipolar Organic Field-Effect Transistors and Inverters. *Nat. Mater.* **2003**, *2*, 678-682.

36. Vollmer, A.; Weiss, H.; Rentenberger, S.; Salzmann, I.; Rabe, J. P.; Koch, N., The Interaction of Oxygen and Ozone with Pentacene. *Surface Science* **2006**, *600*, 4004-4007.

37. Jurchescu, O. D.; Baas, J.; Palstra, T. T. M., Electronic Transport Properties of Pentacene Single Crystals upon Exposure to Air. *Appl. Phys. Lett.* **2005**, *87*, 052102.

38. Son, D. I.; Kim, T. W.; Shim, J. H.; Jung, J. H.; Lee, D. U.; Lee, J. M.; Park, W. I.; Choi, W. K., Flexible Organic Bistable Devices Based on Graphene Embedded in an Insulating Poly(methyl methacrylate) Polymer Layer. *Nano Lett.* **2010**, *10*, 2441-2447.

39. Park, J. H.; Hwang, D. K.; Lee, J.; Im, S.; Kim, E., Studies on Poly(methyl methacrylate) Dielectric Layer for Field Effect Transistor: Influence of Polymer Tacticity. *Thin Solid Films* **2007**, *515*, 4041-4044.

40. Yun, W. M.; Jang, J.; Nam, S.; Jeong, Y. J.; Kim, L. H.; Park, S.; Seo, S. J.; Park, C. E., Vacuum Thermally Evaporated Polymeric Zinc Acrylate as an Organic Interlayer of Organic/Inorganic Multilayer Passivation for Flexible Organic Thin-Film Transistors. *J. Mater. Chem.* **2012,** *22*, 25395-25401.

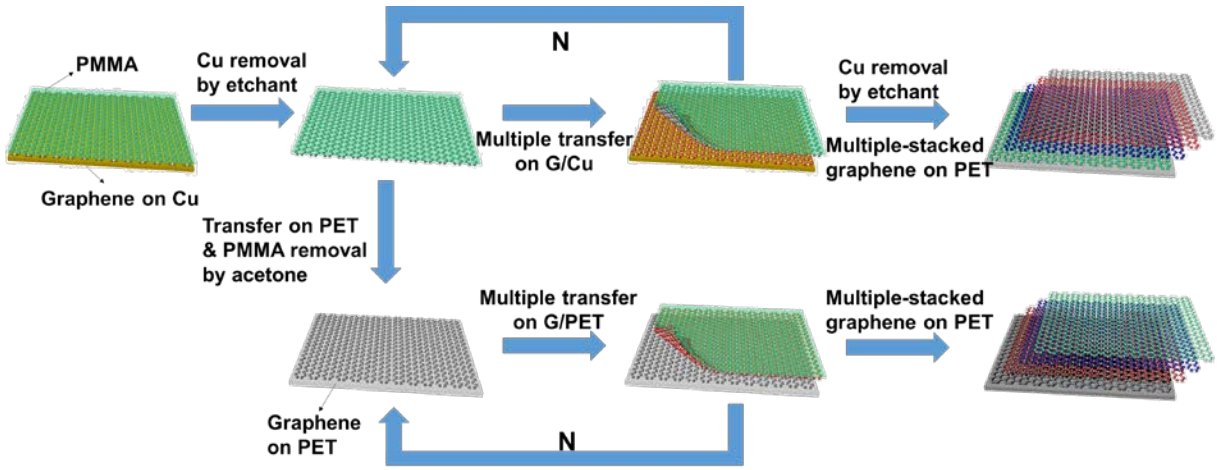

Figure 1. A schematic representation showing the multiple graphene transfer processes that use only a single PMMA removal step (upper) and multiple PMMA removal steps (lower).

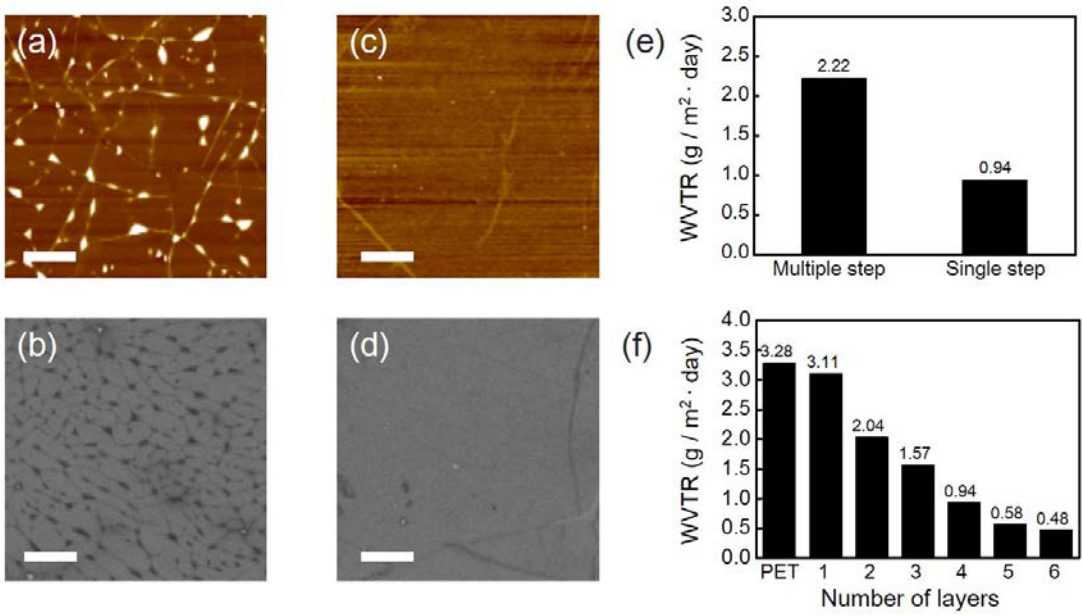

Figure 2. (**a-d**) AFM and SEM images of multilayer graphene transferred by the single PMMA removal step (a, b) and the multiple PMMA removal step (c, d), respectively. Scale bars, 1 μm. (**e**) WVTR values of 4-layer graphene transferred by the multiple/single use of PMMA coating. (**f**) WVTR values of graphene transferred on a PET film with respect to increasing number of graphene layers at 23 °C and 100% relative humidity.

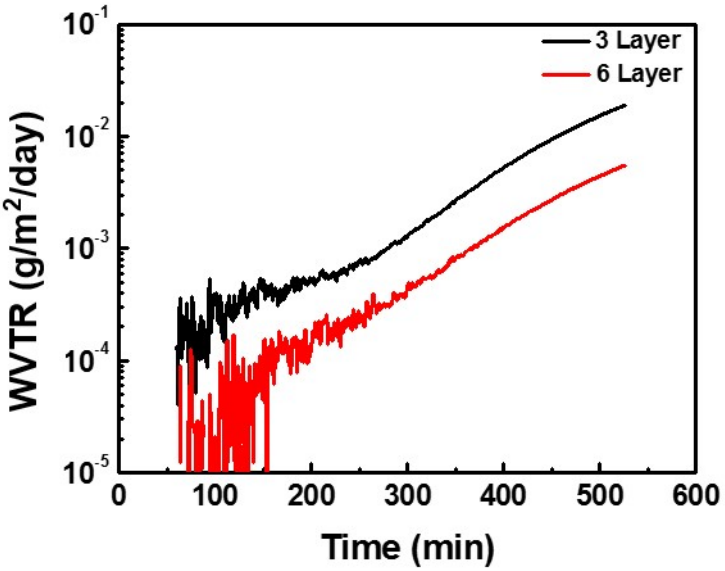

Figure 3. WVTR versus time (min) with respect to the different number of graphene layers transferred on to PET substrates.

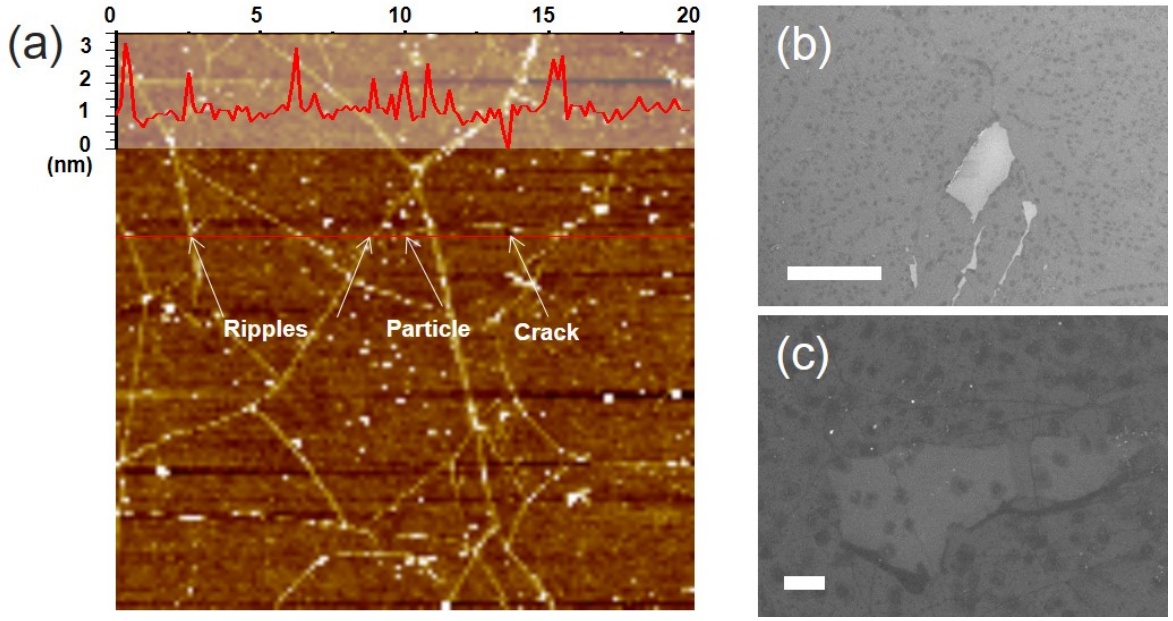

Figure 4. (a) AFM image of single layered graphene films showing some crack, ripples and nano-scale particles. SEM image of (b) the torn area in monolayer graphene and (c) the additional graphene covered the torn area of the previous graphene. Scale bars are 5μm, and 2 μm, respectively.

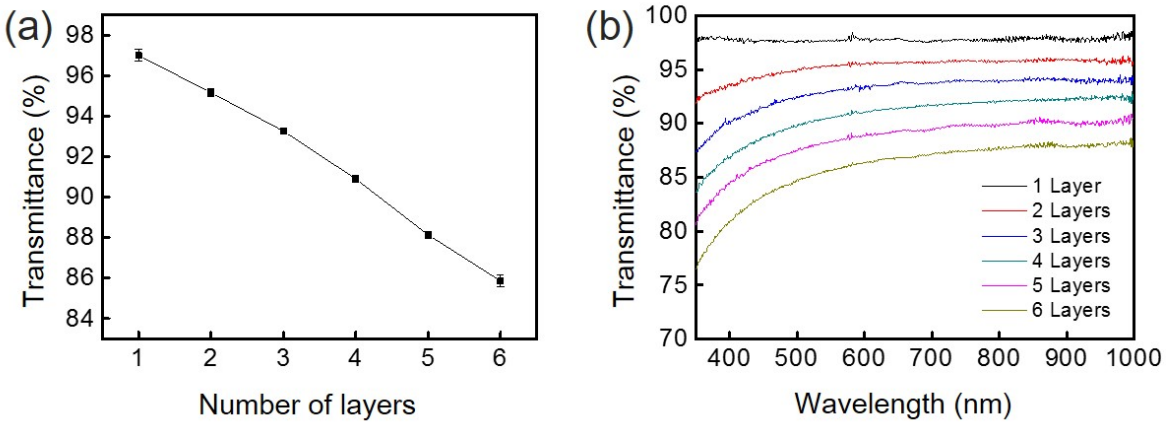

Figure 5. (**a, b)** Optical transmittance and UV–Vis spectra of graphene films on PET films with increasing number of graphene layers, respectively.

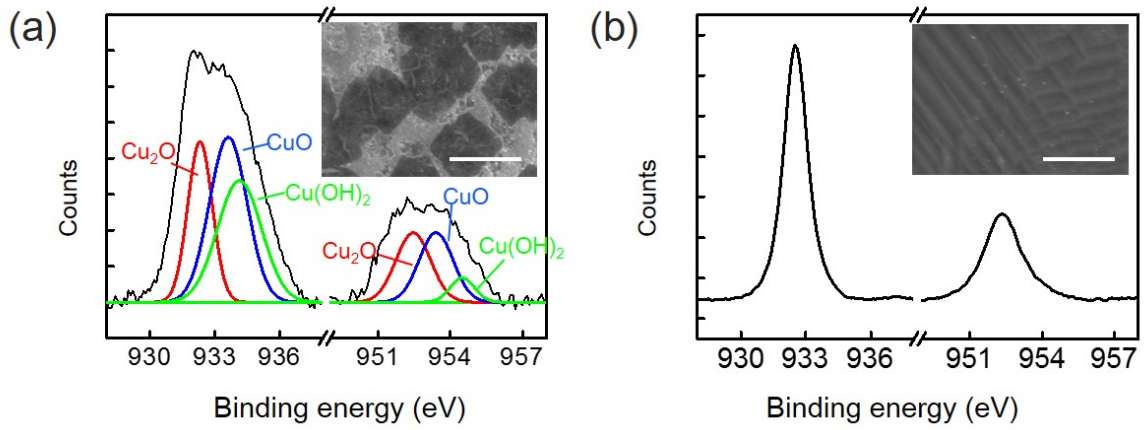

Figure 6. XPS spectra of (a) bare Cu foil and (b) Cu foil with graphene film after air oxidation ($Cu2p_{3/2}$; 932.6 eV, $Cu2p_{1/2}$: 952.4 eV, Cu_2O ; 932.4 and 952.4 eV, CuO ; 933.6 and 953.4 eV, $Cu(OH)_2$; 934.3 and 954.5 eV) after two months under ambient pressure and room temperature. Scale bars, 2 μm.

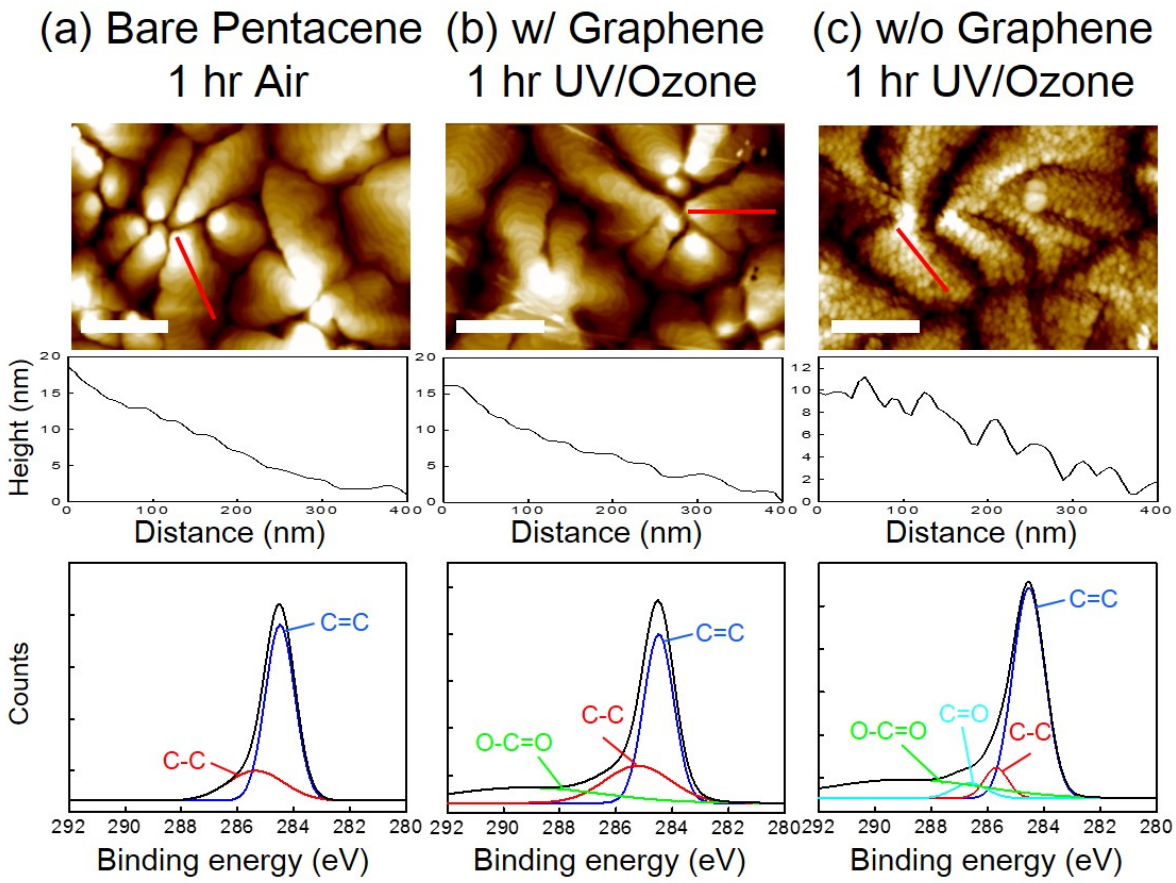

Figure 7. (**a-c**) AFM topographs and XPS spectra of bare pentacene, oxidized pentacene with graphene, and oxidized pentacene without graphene, respectively. Scale bars, 400 nm. The oxidation was carried out by using UV/Ozone treatment for 1 hour. The AFM profiles of pentacene on SiO_2/Si along the red line clearly shows the degradation of pentacene film by oxidation. The XPS analyses of the C1s core level bands show that the oxygen related peaks appear as oxidation proceeds.

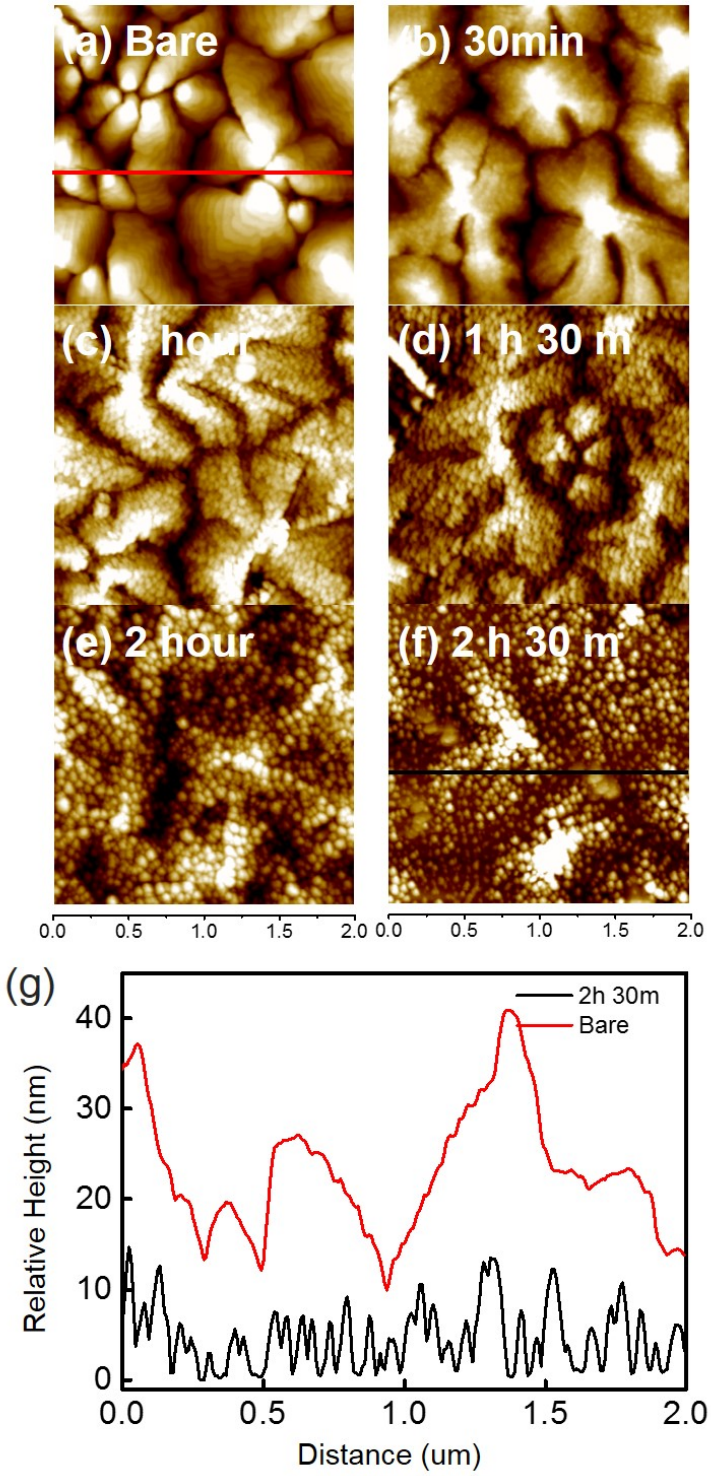

Figure 8. (a) ~ (f) AFM topographs of pentacene as a function of UV/Ozone treatment time. (g) Cross sectional AFM relative height of (a) bare pentacene and (f) oxidized pentacene for 2 h 30 m.

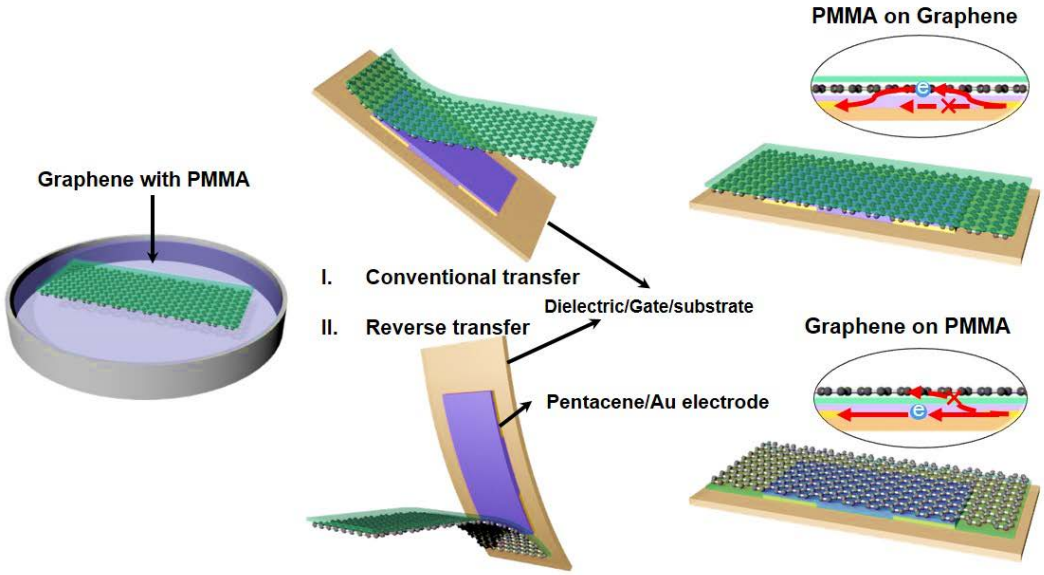

Figure 9. Schematic of the difference between the conventional and reverse method for transferring graphene films.

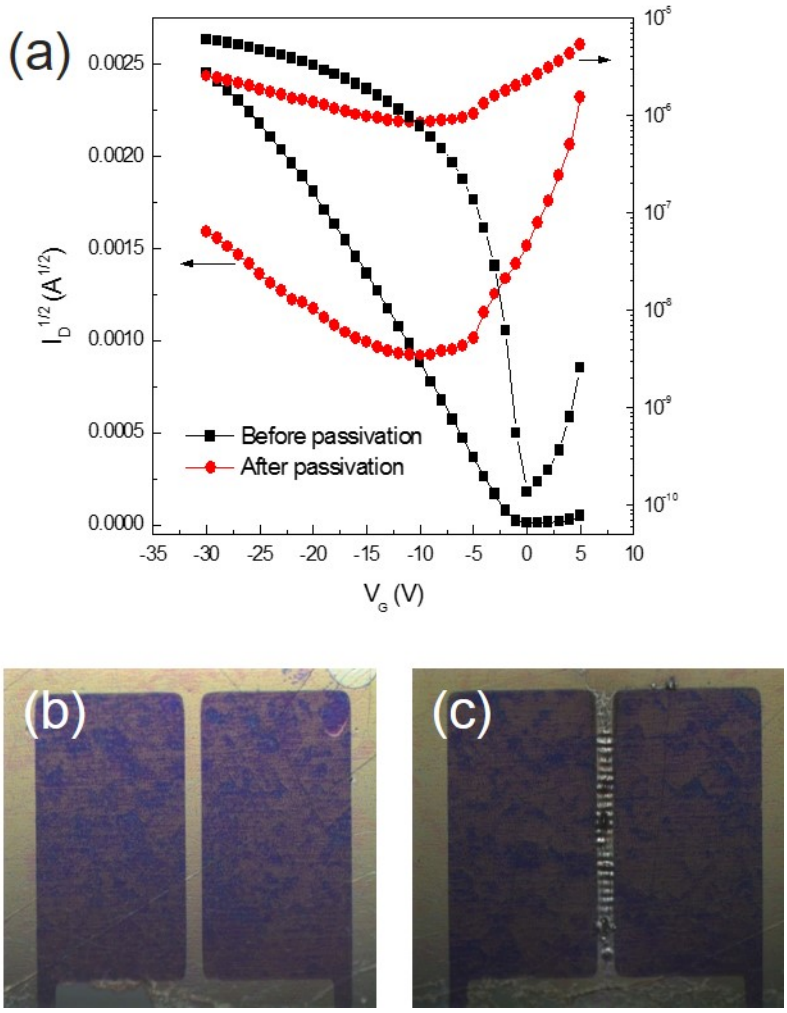

Figure 10. (a) I_D versus V_G transfer characteristics and $I_D^{1/2}$ versus V_G characteristics of before (black curve) and after (red curve) passivated OFET with graphene. (b) Before applying voltage to a passivated OFET and (c) after applying voltage to a passivated OFET

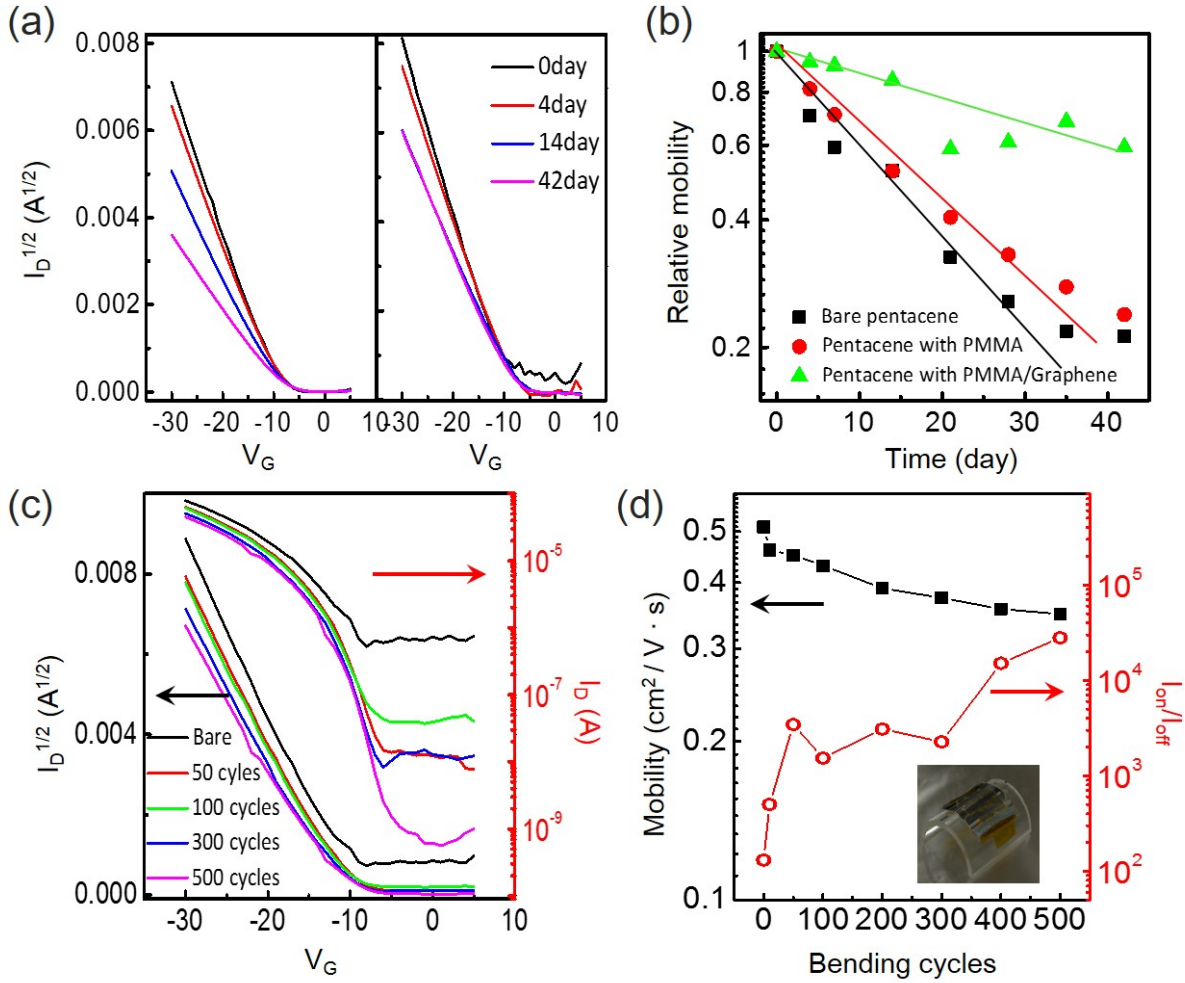

Figure 11. (a) Time-dependent $I_D^{1/2}$ *vs*. V_G characteristics of the bare OFETs (left) and an OFET passivated with PMMA/graphene (right). (**b**) Time-dependent relative field-effect mobilities of bare pentacene, pentacene with PMMA, and pentacene with PMMA/graphene films. Bending cycle tests: (**c**) I_D *vs*. V_G transfer characteristics and the $I_D^{1/2}$ *versus* V_G characteristics of a passivated OFET prepared with PMMA/ 6-layer graphene. (**d**) Field-effect mobility and on-off ratio of a passivated OFET prepared with PMMA/ 6-layer graphene. All the electrical measurements were performed using the reversed transfer method at 25°C under 60% relative humidity.

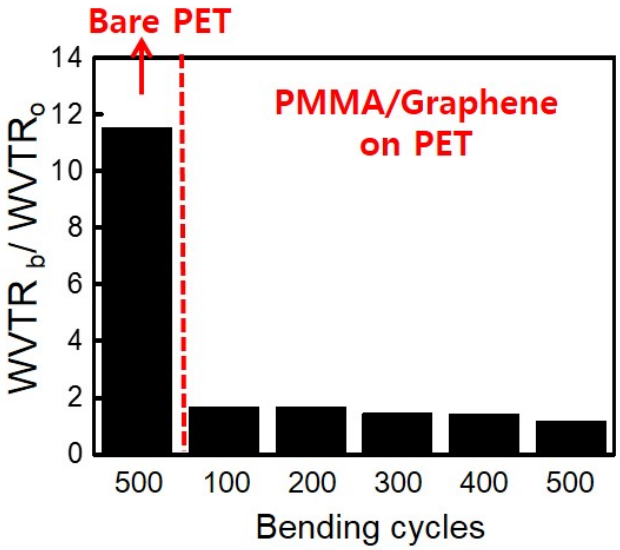

Figure 12. Relative WVTR values with increasing bending cycles, where WVTRo and $WVTR_b$ denote the WVTR values before and after bending, respectively.

Appendix

A. List of Publication

B. List of Presentation

A. List of Publications

1. **Choi, K**.; Nam, S.; Lee, Y.; Lee, M.; Jang, J.; Kim, S. J.; Jeong, Y. J.; Kim, H.; Bae, S.; Yoo, J.-B.; Cho, S. M.; Choi, J.-B.; Chung, H. K.; Ahn, J.-H.; Park, C. E.; Hong, B. H., Reduced Water Vapor Transmission Rate of Graphene Gas Barrier Films for Flexible Organic Field-Effect Transistors. *ACS Nano* (2015).

2. Kim, S. J.; Choi, T.; Lee, B.; Lee, S.; **Choi, K**.; Park, J. B.; Yoo, J. M.; Choi, Y. S.; Ryu, J.; Kim, P., Ultraclean Patterned Transfer of Single-Layer Graphene by Recyclable Pressure Sensitive Adhesive Films. *Nano Lett.* **15**, 3236-3240, (2015).

3. Kim, S. J.; **Choi, K**.; Lee, B.; Kim, Y.; Hong, B. H., Materials for Flexible, Stretchable Electronics: Graphene and 2D Materials. *Ann. Rev. Mater. Res*. **45** (2015) (Co-first authorship)

4. Kim, Y.; Park, J.; Kang, J.; Yoo, J. M.; **Choi, K**.; Kim, E. S.; Choi, J.-B.; Hwang, C.; Novoselov, K.; Hong, B. H., A highly conducting graphene film with dual-side molecular n-doping. *Nanoscale*, **6**, 9545-9549, (2014).

5. Ahn, G.; Kim, H. R.; Ko, T. Y.; **Choi, K**.; Watanabe, K.; Taniguchi, T.; Hong, B. H.; Ryu, S., Optical probing of the electronic interaction between graphene and hexagonal boron nitride. *ACS nano*, **7**, 1533-1541 (2013)

B. List of Presentations

1. Choi, K.; Jeong, Y. J.;. Park, J. B.; Lee, B.; Ryu, J.; Cho, S-P.; Park, C. E.; Hong, B. H.; Selective Growth of Graphene by Chemical Vapor Deposition on Patterned Cu-Ni Alloy Catalyst, The 1st International Conference on Two-Dimensioanl Layered Materials, China, Oct. 2014

2. Choi, K.; Jeong, Y. J.;. Park, J. B.; Lee, B.; Ryu, J.; Cho, S-P.; Park, C. E.; Hong, B. H.; Selective Growth of Graphene by Chemical Vapor Deposition on Patterned Cu-Ni Alloy Catalyst, Graphene Week 2014, Sweden, Jun. 2014

Abstract (Korean)

1장에서는 최근 각광받고 있는 2차원 물질 중 대표적인 그래핀과 TMDs 기본적인 특성 및 이를 얻기 위한 합성법에 대해서 간략히 소개하였다.

2장에서는 그래핀을 원하는 부분에서만 선택적으로 저온에서 합성하는 연구를 하였다. 본 연구에서는 기존의 연구와는 다르게 구리와 니켈의 합금 촉매를 이용하여 그래핀을 합성하였다. 니켈은 높은 탄소 용해도를 가지고 있고 탄화수소를 구리에 비해 잘 분해시키기 때문에 낮은 온도에서 고품질의 균일한 단층 그래핀을 얻을 수 있었다. 구리에서 탄화수소를 분해시키기 위해서는 높은 활성화 에너지를 필요로 한다. 따라서 짧은 시간 동안 그래핀을 합성하면 패턴된 합금 촉매에서는 그래핀이 형성되지만 구리 촉매에서는 그래핀이 형성되지 않는 사실을 밝혔다.

3장에서는 그래핀의 단점을 보완해줄 수 있는 원자 단위의 두께를 가지고 있으면서 반도체적인 특성을 나타내는 단층 이황화물리브데늄을 사파이어 기판 위에서 합성하였다. 합성된 이황화몰리브데늄의 E_{2g}와 A_{1g}의 간격이 약 20 cm^{-1}정도 나오는데 이는 이론적으로 알려진 단층 이황화몰리브데늄이 가지는 값과 유사한 결과값이 나오는 것을 확인할 수 있다. 빛 발광 스펙트럼과 라만 스펙트럼을 통해서 고품질의 이황화몰리브데늄이 합성된 것을 확인할 수 있다.

4장에서는 고품질의 다층 그래핀을 이용하여 대면적 가스 배리어 필름을 만들었다. 그래핀 가스 배리어는 약 10^{-1} g/m^2 day의 특성을 가지고 있는 것을 확인하였다. 또한 그래핀이 가지는 뛰어난 기계적 특성에 의해서 2.3% 정도의 굽힘에도 배리어 특성을 유지하는 것을 확인하였다.

주요어 : 그래핀, 선택적 합성, 배리어 필름, 유기전계효과트랜지스터, 이황화몰리브데늄, 반데르발스 에피택셜

학번: 2013-30094